



# Ion beam characterisation of III-V heterostructures for micro and optoelectronic applications

Viktoriia Gorbenko

## ► To cite this version:

Viktoriia Gorbenko. Ion beam characterisation of III-V heterostructures for micro and optoelectronic applications. Micro and nanotechnologies/Microelectronics. Université Grenoble Alpes, 2015. English. NNT : 2015GREAT140 . tel-01281330

**HAL Id: tel-01281330**

**<https://theses.hal.science/tel-01281330>**

Submitted on 2 Mar 2016

**HAL** is a multi-disciplinary open access archive for the deposit and dissemination of scientific research documents, whether they are published or not. The documents may come from teaching and research institutions in France or abroad, or from public or private research centers.

L'archive ouverte pluridisciplinaire **HAL**, est destinée au dépôt et à la diffusion de documents scientifiques de niveau recherche, publiés ou non, émanant des établissements d'enseignement et de recherche français ou étrangers, des laboratoires publics ou privés.

## THÈSE

Pour obtenir le grade de

### **DOCTEUR DE LA COMMUNAUTÉ UNIVERSITÉ GRENOBLE ALPES**

Spécialité : **NANOELECTRONIQUE ET NANOTECHNOLOGIES**

Arrêté ministériel : 7 août 2006

Présentée par

**Viktoriia Gorbenko**

Thèse dirigée par **Thierry Baron**

Co-encadré par **Jean-Paul Barnes (CEA-LETI)** et **Franck Bassani (LTM-CNRS)**

Préparée au sein du Service de Caractérisation des Matériaux & Composants du LETI et du Laboratoire des Technologies de la microélectronique du CNRS au CEA-Grenoble.

dans l'Écoles Doctorale EEATS

## **Caractérisation par faisceaux d'ions d'hétérostructures III-V pour les applications micro et optoélectroniques**

Thèse soutenue publiquement le **18 Décembre 2015**,  
devant le jury composé de :

**Dr. Michel Gendry**

Directeur de Recherche, INSA de Lyon, Président

**Dr. Brice Gautier**

Professeur des Universités, INSA de Lyon, Rapporteur

**Dr. Thierry Conard**

Ingénieur-chercheur, IMEC, Belgique, Rapporteur

**Dr. Thierry Baron**

Directeur de Recherche, LTM, CNRS, Directeur de thèse

**Dr. Franck Bassani**

Chargé de Recherche, LTM, CNRS, Co-encadrant de thèse

**Dr. Jean-Paul Barnes**

Ingénieur-chercheur, LETI, CEA, Co-encadrant de thèse









# ABSTRACT

The integration of III-V semiconductor compounds on silicon should lead to the development of new highly efficient micro- and optoelectronic devices. High mobility InGaAs material is a promising candidate for n-channel metal-oxide-semiconductor-field-effect transistor beyond the 10 nm technology node. Moreover, III-V semiconductors are also suitable materials for fabrication of optical (lasers, diodes) and ultra-high frequency analog devices and their integration on a Si platform will add new functionalities for optical networks and communication. However, the miniaturization of devices and their integration into 3D architectures require the development of advanced characterization methods to provide information on their physico-chemical composition with nanometer scale resolution.

In this thesis, the physico-chemical studies of III-V heterostructures directly grown on 300 mm Si wafers by metalorganic vapor phase epitaxy are addressed. Secondary ion mass spectrometry (SIMS) techniques are used and developed in order to study interface abruptness, chemical composition and doping of III-V thin layers in 2D and 3D architectures with high depth resolution. The accurate quantitative analysis of InGaAs quantum wells (QWs) in 2D and 3D architectures was performed using magnetic SIMS and Auger techniques. To obtain the chemical profiling of narrow and repetitive III-V structures, an averaging profiling method was developed for both techniques. Additionally, 3D reconstruction and depth profiling of individual trenches (less than a hundred nanometers in width) containing thin InGaAs QWs selectively grown in silicon dioxide cavities using the aspect ratio trapping method were successfully obtained using Time-of-flight SIMS and atom probe tomography. Finally, the results were correlated with photoluminescence measurements.

**KEYWORDS:** III-V heterostructures, SIMS, FinFET, microelectronics, optoelectronics, and quantum wells



# RÉSUMÉ

L'intégration de composés semi-conducteurs III-V sur silicium devrait conduire au développement de nouveaux dispositifs micro- et optoélectroniques performants. Le composé InGaAs de haute mobilité électronique est un candidat prometteur pour le transistor métal-oxyde-semiconducteur à effet de champ à canal n au-delà du nœud technologique 10 nm. En outre les semi-conducteurs III-V sont aussi des matériaux appropriés pour la fabrication de composants optiques (lasers, diodes) et de dispositifs analogiques ultra-haute fréquence et leur intégration sur une plateforme Si ajoutera de nouvelles fonctionnalités pour le réseau de communications optiques. Cependant la miniaturisation des dispositifs et leur intégration dans les architectures 3D nécessitent le développement de méthodes de caractérisation avancées pour fournir des informations sur leur composition physico-chimique avec une résolution à l'échelle nanométrique.

Dans cette thèse, les études physico-chimiques des hétérostructures III-V directement élaborées sur plaquettes de Si 300 mm par épitaxie en phase vapeur sont adressées. Les techniques de spectrométrie de masse d'ions secondaires sont utilisées et développées dans le but d'étudier la raideur des interfaces, la composition chimique et le dopage de couches III-V minces dans des architectures 2D et 3D avec une bonne résolution en profondeur. L'analyse quantitative précise sur un puits quantique InGaAs (PQ) pour des architectures 2D et 3D a été réalisée en utilisant les techniques SIMS magnétique et Auger. Pour obtenir le profil chimique des structures III-V étroites et répétitives, une méthode de moyenne des profils a été développée pour ces deux techniques. Egalement, la reconstruction 3D et le profil en profondeur de tranchées individuelles (moins de cent nanomètres de largeur) contenant un PQ d'InGaAs mince obtenu par croissance sélective dans des cavités de dioxyde de silicium en utilisant la méthode de piégeage des défauts par rapport d'aspect ont été obtenus avec succès en utilisant le SIMS à temps de vol ainsi que la sonde atomique tomographique. Enfin, les résultats ont été corrélés avec des mesures de photoluminescence.

**MOTS-CLÉS:** III-V hétérostructures, SIMS, FinFET, microélectronique, optoélectronique, puits quantique



*L'expérience est une lanterne accrochée  
dans le dos qui n'éclaire que le chemin parcouru ...*

*Confucius*



## ACKNOWLEDGMENTS

I believe that with an expert guidance everything is possible. I would like to thank the supervisors of my thesis, Dr. Jean-Paul Barnes and Dr. Franck Bassani, for patience, support and guidance in writing of the thesis. I very appreciate their contributions, discussions and advices in the research work (conferences, publications, seminars, symposiums etc.). I am grateful for (English and French) language revision of my thesis. I would like to thank the director of my thesis, Dr. Thierry Baron, for expert guidance of my thesis and great positive mood all the time. I was lucky to work with one of the kindest and friendliest supervisors.

I thank the Material Integration team at LTM-CNRS Laboratory for great teamwork in MINOS project, scientific discussions concerning growth of materials, and nice friendly working atmosphere. Especially I would like to mention the Romain Cipro (soon Dr), Dr. Mickael Martin, and Arnaud Alcoud for providing the samples and great discussions together. Thanks to Dr. Yann Bogumilowicz for his advices for my thesis.

I would like to thank also the Nanocharacterization group at LETI-CEA for great support and very friendly atmosphere. I thank Dr. Marc Veillerot and Dr. Alexandre Merkulov (from Cameca) for their advices and training in working with SIMS SC Ultra instrument. I was working with the great international team. Especially I would like to mention my colleagues with whom I shared my office: Riccardo, Robert and Tanguy. Three years of working together have passed so fast. Thanks them for all fantastic time, coffee breaks (who can do research without café ☺ ?!!), lunch time, many different discussions (scientific and non-scientific) and for all great Ph.D. moments.

I am grateful to Dr. Adeline Grenier, Dr. Sylvain David and Dr. Guillaume Audoit for FIB-STEM and APT experiments, Dr. Francois Pierre for RBS experiments. I am thankful to Dr. Wael Hourani for many discussions concerning Auger experiments, as well for his support and help. I am grateful to Dr. Dennis Mariolle and Dr. Lukasz Borowik for advices concerning AFM measurements and pleasant working time together. Thanks to my dear colleagues and friends Dr. Camille Marie, Dr. Agnieszka Priebe, Dr. Ferrah Djawhar, and Mariana Verezhak (soon Dr.) for their help in preparation of the Ph.D. defense and, in general, for all support and shared sports activities (ski, swimming, ice-skating etc.).

Thanks to LTM and LETI administration, Dr. Jean-Claude Royer, Dr. Francois Bertin and Dr. Gambacorti Narciso for their help and advices in my research work.

It was a great pleasure to work with you. Merci à tous!

My deepest thanks and gratitude I wish to express to my wonderful family. I am happy to have you, my dear sister Nataliya (Dr.), brother Ivan (maybe a future Dr.), father Vitalij (Dr.) and mother Iryna (Mother).



# CONTENTS

ABBREVIATION INDEX .....	15
CHAPTER I INTRODUCTION AND OVERVIEW .....	19
I.1. III-V materials as channel materials.....	22
I.2. State of the art of III-V integration on Si substrate .....	24
I.2. Challenges of nano-characterization of channel materials in 2D and 3D architectures	28
I.2.1 Doping profiling in 3D architecture materials .....	28
I.2.2 SIMS profiling of InGaAs materials overview .....	30
CHAPTER II Growth of III-V heterostructures and characterization methods .....	35
II.1 Growth of III-V heterostructures on Si wafers by MOCVD.....	35
II.1.1 The basic principles of the MOCVD technique .....	35
II.1.2 MOCVD reactor .....	37
II.1.3 Challenges of III-V growth on Si wafers .....	37
II.1.4 Sample description .....	39
II.1.4.1 InGaAs/AlAs quantum wells on planar Si substrates .....	39
II.1.4.2 InGaAs reference samples for quantitative SIMS analysis.....	41
II.1.4.3 Selective growth of III-V heterostructures on non-planar Si-substrates by MOCVD .....	43
II.1.4.4 Doping in planar and non-planar samples .....	44
II.2 Ion beam characterization techniques .....	45
II.2.1 Secondary ion mass spectrometry .....	45
II.2.1.1 Time of flight mass spectrometry .....	46
II.2.1.2 Experimental conditions .....	47
II.2.1.3 Magnetic sector SIMS.....	47
II.2.1.4 Instrumentation of CAMECA SC-Ultra magnetic SIMS.....	49
II.2.1.5 Experimental conditions .....	51
II.2.1.6 Depth calibration.....	53
II.2.2 Atom probe tomography .....	53
II.2.2.1 Sample preparation for APT using the focused ion beam technique.....	55
II.2.2.2 Experimental conditions .....	57
II.2.3 Auger technique .....	57
II.2.3.1 Experimental conditions .....	59

II.2.4	Rutherford backscattering spectrometry .....	60
II.2.4.1	Experimental conditions .....	62
CHAPTER III	Quantitative chemical analysis of III-V elements using SIMS .....	65
III.1.	Theoretical aspects of quantitative SIMS analysis .....	65
III.2.	Description of reference standards for accurate measurements of composition in $\text{In}_x\text{Ga}_{1-x}\text{As}$ and $\text{Al}_x\text{Ga}_{1-x}\text{As}$ matrices.....	68
III.2.1	Ion-implanted standards .....	68
III.2.2	Standards for accurate measurements of x in $\text{In}_x\text{Ga}_{1-x}\text{As}$ matrix .....	70
III.3.	Development of a SIMS protocol for InGaAs channel material .....	74
III.3.1	Quantitative analysis of InGaAs QW using $\text{O}_2^+$ ion beam bombardment .....	74
III.3.2	Quantitative analysis of InGaAs quantum well using SIMS.....	82
III.3.3	Quantitative analysis of InGaAs quantum well using complementary techniques	84
III.3.4	Quantification using molecular $\text{MCs}^+$ ions under low energy sputtering .....	86
III.4	.Development of a SIMS protocol for n-doped GaAs in 2D and 3D architectures .....	88
CHAPTER IV	Development of experimental protocols for chemical composition profiling of 3D architecture structures.....	99
IV.1	.Recall of basic parameters of the investigated sample.....	99
IV.2.	An average approach using low energy magnetic SIMS .....	99
IV.2.1	SIMS conditions optimization in terms of sample topography and depth resolution under oxygen ion beam bombardment.....	100
IV.2.1.1	Effect of primary energy .....	100
IV.2.1.2	Effect of orientation of the ion beam with respect to the trenches .....	102
IV.2.1.3	Effect of incidence angle .....	107
IV.2.1.4	Effect of sample rotation.....	109
IV.3	3D reconstruction of a single III-V trench using ToF-SIMS and atom probe tomography.....	116
IV.4	Quantitative analysis of InGaAs quantum well by Auger and SIMS techniques	121
CONCLUSIONS	.....	128
PERSPECTIVES:	.....	131

## ABBREVIATION INDEX

AES	Auger electron spectroscopy
AFM	Atomic force microscopy
AMAT	Applied Materials Tool
APB	Anti-phase boundary
APD	Anti-phase domain
APT	Atom probe tomography
AR	Aspect ratio
ART	Aspect ratio trapping
BOX	Buried-oxide
CELO	Confined epitaxial lateral overgrowth
CMOS	Complementary metal-oxide-semiconductor technology
CVD	Chemical vapor deposition
DWB	Direct wafer bonding
EM	Electron multiplier
ESA	Electrostatic sector analyzer
EXLIE	Extremely low primary beam impact energy
FC	Faraday cup
FIB	Focused ion beam
FinFET	Fin-shaped field-effect transistor
FWHM	Full-width at half-maximum
HF	Hydrogen fluoride
IC	Integrated circuit
ITRS	International Technology Roadmap for Semiconductors

LED	Light-emitting diode
LTE	Local thermal equilibrium
MBE	Molecular beam epitaxy
MOCVD	Metalorganic chemical vapor deposition
MOSFET	Metal-oxide-semiconductor field-effect transistor
NW	Nanowires
PIGE	Particle induced Gamma-Ray emission
PIXE	Particle induced X-ray technique
PL	Photoluminescence
QW	Quantum well
RBS	Rutherford backscattering spectrometry
RF	Radio frequency
RMS	Root mean square
RSF	Relative sensitivity factor
SF-SIMS	Self-focusing SIMS
SIMS	Secondary ion mass spectrometry
SR	Sputter rate
STEM	Scanning transmission electron microscope
STI	Shallow trench isolation
TEGa	Triethylgallium
TEM	Transmission electron microscopy
TMAI	Trimethylaluminium
TMGa	Trimethylgallium
ToF-SIMS	Time-of-flight SIMS
TRIFT	Triple focusing time of flight

XRD

X-ray diffraction

3D

Three-dimensional



# CHAPTER I

## I. INTRODUCTION AND OVERVIEW

Over the past fifty years, the miniaturization of circuits by transistor scaling remains the main technology trend in the semiconductor industry [W. Arden et al., 2004]. The International Technology Roadmap for Semiconductors (ITRS) [www.itrs.net] according to Moore's law defines the continuous downscaling of integrated circuits (IC) by a factor 0.7 every two years. Moore's law states that the number of IC components increases exponentially over time. It requires the improvement of the performances, i.e. increasing the speed and the power of transistors, whilst reducing the cost per transistor. Thus, it has a big influence on the semiconductor market as it provides a benchmark for semiconductor manufacturing.

The semiconductor benchmarking is accompanied by the continuous studies of material properties. The research goal is to find alternative semiconductor compounds with the best physical features with low-cost semiconductor manufacturing. Silicon has high mechanical strength and extremely high-quality in comparison with other materials (e.g. GaAs, InP). For this reason, a silicon-based manufacturing replaced the first established germanium-based device industry. Thus, large-scale devices, such as GaN or InGaN-based light-emitted diodes (LED), III-V laser diodes and transistors can be integrated (co-integrated) on large-area silicon wafers (300 mm, 450 mm in near future).

The evolution of complementary metal-oxide-semiconductor (CMOS) technology over the last fifteen years is illustrated in Figure I-1. However, the device scaling revealed new challenges in transistor manufacturing. The reduction of the operation voltage has to be considered in order to solve the issue of power dissipation in logic chips. [J. A. del Alamo, 2011]. Also, the switching speed has to be accordingly adjusted. The transistor performance, in general, has to be improved, thus, issues of channel mobility, electrostatic control, parasitic resistance and gate capacitance are still important for device performance [K. J. Kuhn, 2012]. Further scaling of transistors was made possible recently by the introduction 3-dimensional (3D) device architectures. Such architectures may take the form of the fin-shaped field-effect transistor (FinFET), TriGate, and Gate-all-around transistors [K. J. Kuhn, 2012]. Moreover, FinFET and TriGate transistors were recently manufactured by Intel for the 22-nm and 14-nm node CMOS technology, respectively (see Figure 1-1).

The integration of III-V semiconductors on Si wafers in 3D architectures will give new functionalities in opto- and microelectronic applications. Furthermore, III-V materials have interesting physical properties, such as a high carrier transport, direct and wideband gap. However, the integration of III-V on Si faces growth-related challenges, i.e. a thermal and lattice mismatches of semiconductors, which affect the device operation. The growth and characterization of III-V semiconductors grown on planar and non-planar Si substrates using ion beam techniques are addressed in this thesis and presented in the following four chapters.

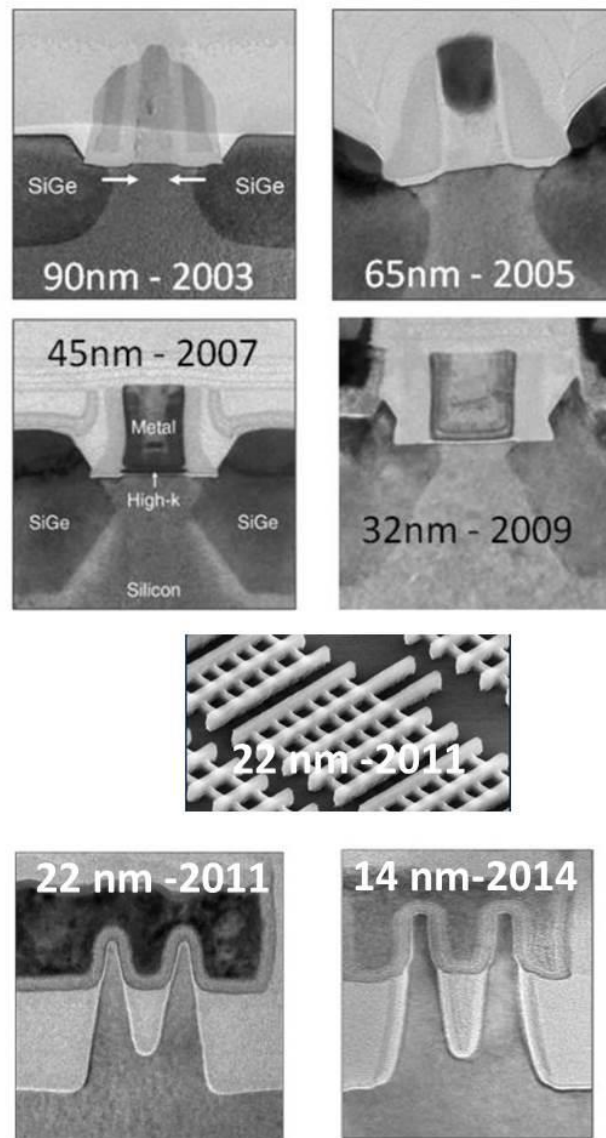


Figure I-1 CMOS scaling evolution from 90 nm to 14 nm technology node. Prototypes are demonstrated by Intel company [K. J. Kuhn, 2012, M. Bohr, 2014].

**Chapter I** introduces the III-V integration technology on Si wafers. The first section describes the physical properties of III-V materials that make them suitable for opto- and micro-electronics applications. In particular, the main application of III-V materials on Si is described and their use as channel materials in nMOSFETs technology. It reports on the III-V FinFET and FDSOI technology issues. The most promising and recently reported approaches to integrating III-V on Si wafers, such as direct wafer bonding, lateral overepitaxy, and aspect ratio trapping are described. The second section focuses on the characterization issues of materials in 3D architectures. It summarizes the very recently reported works regarding 3D doping profiling and chemical profiling of thin InGaAs layers.

**Chapter II** describes the growth and characterization techniques and also the samples investigated in this thesis. The first section of this chapter is focused on the epitaxial growth process of III-V heterostructures on 300 mm Si wafers using MOCVD. The challenges and

methods to obtain high-quality III-V layers on Si wafers are addressed. The description of InGaAs quantum wells (QW) and Si-doped GaAs samples grown by MOCVD studied using magnetic secondary ion mass spectrometry (SIMS) and Time-of-flight (ToF) SIMS is given. The first section includes also the description of reference sample used for quantitative analysis. The second section is focused on the ion beam techniques used in this work. It starts with a description of the basic principles of magnetic SIMS and ToF-SIMS followed by the details of the Cameca SC-Ultra instrument used in this work. Then the basic principles of atom probe tomography (APT), Auger and Rutherford backscattering spectrometry (RBS) are explained. Moreover, at the end of each sub-section, the experimental details for each technique are given.

**Chapter III** is focused on the compositional analysis of  $\text{In}_x\text{Ga}_{1-x}\text{As}$  QWs and 3D-doping profiling using SIMS for future generations of transistors. It starts with theoretical background on the quantitative analysis using SIMS. The development of SIMS protocols under oxygen and cesium ion beam sputtering under low impact energy is described. Quantitative analysis using reference  $\text{In}_x\text{Ga}_{1-x}\text{As}$  series designed in this thesis is explained. Moreover, the ion yield as a function of indium fraction  $x$  and primary energy of ion beam is experimentally determined. Quantitative analysis using  $\text{MCs}^+$  ions was also demonstrated. Finally, the development of SIMS and ToF-SIMS protocols for Si-dopant profiling in 2D and 3D architectures is described.

**Chapter IV** reports on the investigation of repetitive III-V trench arrays selectively grown by MOCVD on patterned Si wafers. The first section of this chapter introduces the average approach for chemical depth profiling of repetitive array of III-V trenches. This section describes also the optimization and development of the SIMS conditions used to profile the III-V trench arrays. SIMS parameters, such as (1) the impact of primary energy, (2) incident angle and (3) orientation of the ion beam with respect to the trenches are investigated in detail in order to improve the depth resolution. Investigation of topography formation under oxygen irradiation on III-V materials using atomic force microscopy observations and correlation with SIMS profiles is also included. The second section describes 3D chemical profiling of thin InGaAs QWs grown on patterned Si wafers using ToF-SIMS and APT techniques. This section represents the complementary studies performed on individual III-V trench arrays using the pointed and average analysis method by Auger technique. Finally, the quantitative chemical analysis for repetitive InGaAs QWs arrays studied using Auger, SIMS, photoluminescence techniques are described.

The conclusions and perspectives summarize the main results obtained in this thesis and outline the perspectives for this work in terms of characterization of III-V semiconductors for advanced CMOS technology.

## I.1 III-V materials as channel materials

III-V semiconductors are promising materials for realization of high performance of metal-oxide-semiconductor field effect transistor (MOSFET) and will be manufactured starting from 2018 according to ITRS 2013 roadmap [www.itrs.net]. Integration of high mobility III-V materials is essential for increasing the transistor performance with a reduction in voltage [J. A. del Alamo, 2011]. The carrier mobility of III-V semiconductor compounds is illustrated in Figure I-2. As can be seen, III-As based components exhibit an electron mobility ( $>8000 \text{ cm}^2/\text{V}\cdot\text{s}$ ) ten times higher than silicon, while III-Sb based components have a hole mobility in the same order than germanium. Thus, the replacing of silicon channels by InGaAs or InAs materials will allow transistor performance to be improved.

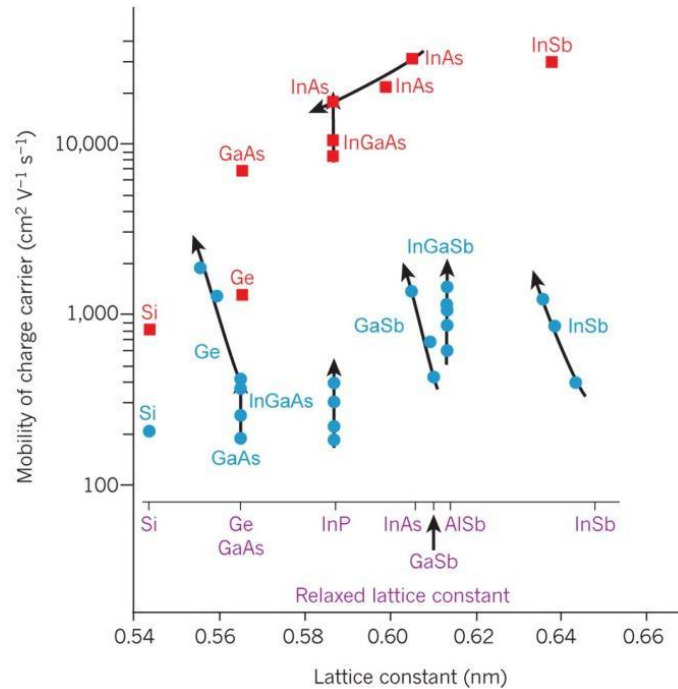


Figure I-2 Electron and hole mobility versus a lattice constant of III-V group compounds, where the highest room-temperature mobility of holes and electrons are marked in blue and red color, respectively. Figure is taken from reference [J. A. del Alamo, 2011].

Due to direct and wide band gap ( $\sim 1\text{-}2.2 \text{ eV}$ ), III-V materials are also often used for fabrication of optoelectronic devices, such as lasers, diodes etc. For example, III-nitride-based LEDs are commonly used in general lighting, traffic signals, video displays, sensors, etc. Moreover, the heterogeneous integration of III-V on Si will make the manufacture of various semiconductor chips possible [J. A. del Alamo, 2011]. Applications of III-V materials in high electron mobility transistor (HEMT) and Si photonics are promising for data transfer by combining systems with a cell phone, TV and Internet together [T. Li et al., 2011]. Additionally, III-V materials (e. g. GaN) can be used in solar cells and high-power/high-frequency transistors (broadcast, wireless infrastructure, defense). The main application of the

III–V materials on Si is, however, the high-speed devices in nMOSFETs technology [G. Doornbos et al., 2010] and is discussed below.

As an example, the structure of III-V nMOSFET (NMOS) and Ge pMOSFET (PMOS) in CMOS technology are illustrated in Figure I-3. As was mentioned previously, III-V and Ge materials have to be integrated on Si substrates, however, such issues need to be solved for CMOS technology: (i) growth of high-quality III-V and Ge materials on Si substrates, (ii) interface quality between gate insulator and channel material, (iii) formation of low resistivity source/drain contacts [S. Takagi et al., 2007, S. Takagi et al., 2013].

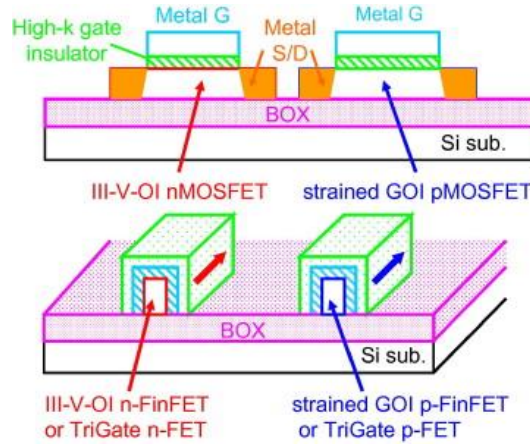


Figure I-3 CMOS device structure of III-V nMOSFET and Ge pMOSFET. Figure is taken from reference [S. Takagi et al., 2013].

The integration of the gate on III-V is challenging. Possible planar quantum well (QW) MOSFET designs are illustrated in Figure I-4 a, b. The advantages having the channel localized under the source and drain (see Figure I-4 a) are process flexibility and possibility to obtain high mobility transport in the device. In this device, the dielectric/III-V interface is created later in the process. It allows the uniaxial strain in the channel to be introduced. Promising results of electrical characteristics of planar QW MOSFET devices were reported by R. Terao [R. Terao et al., 2011]. However, scaling of the planar QW MOSFET requires a very thin channel (less than 10 nm) and extremely thin gate barrier which is difficult to achieve. Additionally, the quantum confinement in silicon or III-V may be critical for devices with a thickness less than 5 nm. It may lead to increasing the threshold voltage ( $V_T$ ) and changes in the scattering behavior (transport of electrons). [K. J. Kuhn, 2012]. Therefore, alternative device designs (Figure I-4 c, d), e.g. III-V FinFET or Gate-all-around nanowires, are designed to improve the electrostatics in MOSFETs. In such devices, the III-V channel is surrounded with two or more opposing gates to improve the short-channel control. Moreover, the effective channel length  $\lambda_N$  can be improved by increasing the number of gates, decreasing the gate dielectric thickness and channel thickness, or by decreasing the permittivity of the channel [K. J. Kuhn, 2012].

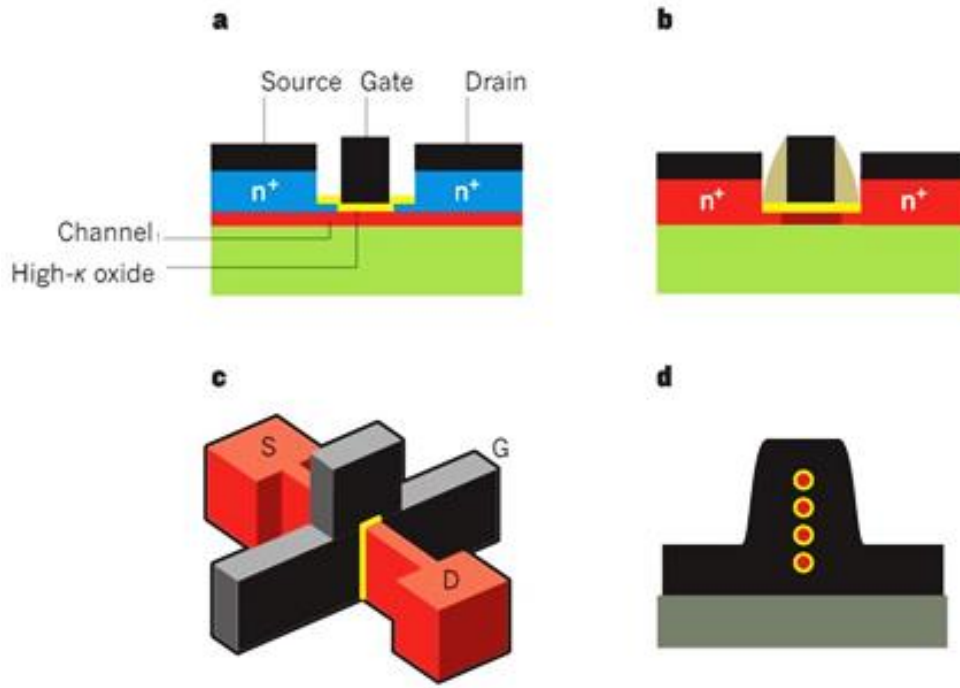


Figure I-4 Architecture of MOSFETs based on the III-V channel materials, where a) etched source-and-drain QW MOSFET, b) regrown source-and-drain QW MOSFET, c) III-V FinFET, d) Gate-all-around nanowire MOSFET. Figure is adapted from reference [J. A. del Alamo, 2011].

Further, such architectures as Pi-Gates (the side gates extend below the channel) and Omega-FETs (the gate wraps the top and surrounds the part of the fourth side) can be mentioned for future integration of III-V channel materials [K. J. Kuhn, 2012]. However, prototypes of such III-V devices were not yet developed.

## I.2 State of the art of III-V integration on Si

The growth of III-V compounds on Si has been studied for over 30 years. The growth of high-quality III-V on Si remains challenging due to the thermal coefficient mismatch and large lattice mismatch between III-V materials and Si. The large lattice mismatch leads to the formation of misfit dislocations with high density which results in the degradation of devices performance. Moreover, thermal expansion coefficient difference might cause additional strain in the layers, even the presence of cracks in thick layers (see Chapter II). Thus, to overcome these issues and to integrate III-V on silicon different methods were developed and are discussed below.

The first approach is based on the direct wafer bonding (DWB) process similar to the silicon-on-insulator (SOI) technology. InGaAs on donor InP wafers are used to fabricate InGaAs channels on SOI. The fabrication process of an InGaAs layer of 3 nm in thickness with a

lattice matched InP on Si by molecular beam epitaxy (MBE) is illustrated in Figure I-5a [S. Takagi et al., 2013]. Figure I-5b shows a transmission electron microscopy (TEM) image of a good quality InGaAs-OI layer with the smooth and abrupt interfaces. For buried-oxide (BOX) layers, the  $\text{Al}_2\text{O}_3$  thin films of 7.7 nm were used to integrate III-V-OI on Si wafers. High electron mobility in the range of 2000-3000  $\text{cm}^2/\text{Vs}$  for the 450 nm in thickness  $\text{In}_{53}\text{GaAs-OI}$  has been reported using this approach [X. Dai et al., 2014].

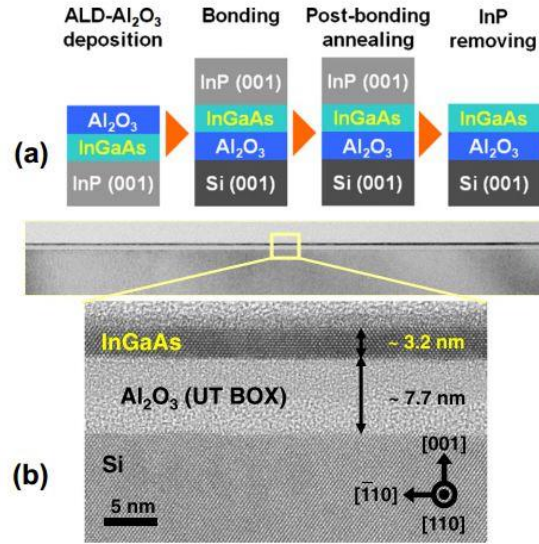


Figure I-5 a) Fabrication process of InGaAs-OI substrates, b) cross-sectional TEM image of InGaAs-OI on Si wafers. Figure is taken from reference [S. Takagi et al., 2013].

The fabrication of ultrathin InAs on SOI was also reported. Firstly, GaSb donor substrates with an AlGaSb sacrificial etch layer and InAs active layer with PMMA are used. Then, active layers are patterned into nanoribbons and the sacrificial layer is partially etched. Finally, the thin InAs films are transferred on  $\text{SiO}_2/\text{Si}$  substrates. (see Figure I-6). The main challenges of SOI integration are issues of scaling up to large wafers (300 mm or 450 mm in future) and the high cost of device fabrication [J. A. del Alamo, 2011].

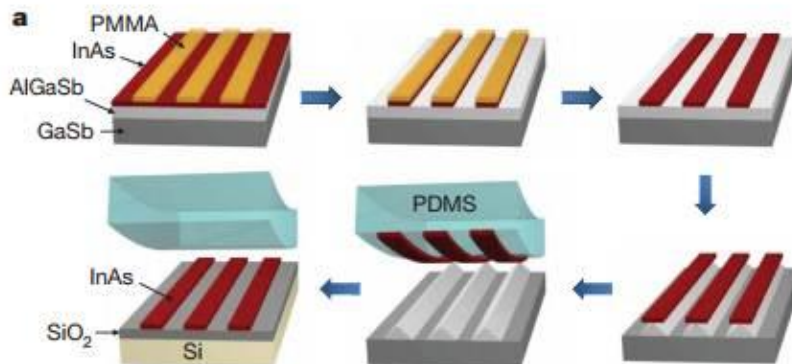


Figure I-6 a) Fabrication process of InAs with silicon-on-insulator (SOI) technology. The epitaxially grown, single-crystal InAs films are patterned with PMMA and wet etched into nanoribbon arrays. A subsequent selective wet etch of the underlying AlGaSb layer and the transfer of nanoribbon arrays by using an elastomeric PDMS slab result in the formation of InAs nanoribbon arrays on  $\text{Si}/\text{SiO}_2$  substrates. Figure is taken from reference [H. Ko et al., 2010].

A second approach is based on the selective heteroepitaxial growth of high-quality III-V channel materials using the aspect ratio trapping (ART) or necking effect approach (see Chapter II.1.3). The reduction of dislocation density at  $\text{Si}_{1-x}\text{Ge}/\text{Si}$  interfaces by selective growth in small areas of patterned Si substrates by chemical vapor deposition (CVD) was demonstrated in 1990. [D. B. Noble et al., 1990] After twenty years, the growth of lattice-mismatched materials like GaAs (Figure I-7 a, b) [Y. Q. Wu et al., 2008, Z. Zuoming et al., 2009], Ge [J.-S. Park et al., 2009] and InP [C. Merckling et al., 2013] on patterned silicon wafers was successfully demonstrated. For selective epitaxial growth of III-V materials on Si, an MOCVD technique is mainly used [C. Merckling et al., 2013, R. Castillo Ojeda et al., 2007, G. Wang et al., 2010]. The InP growth in shallow trench isolation (STI) on patterned Si (001) with a width in the range of 40 to 500 nm using selective epitaxial growth was demonstrated using the ART method [C. Meckling, 2013]. The dislocations that are generated at the III-V/Si substrate are trapped in the  $\text{SiO}_2$  walls and therefore, reducing the number of dislocations and providing high-quality material near the top surface. The high-quality of III-V materials on Si wafers in STI structures can be achieved with an aspect ratio (AR) more than 2 [J. G. Fiorenza et al., 2010]. However, the extreme scaling of the trench width down to 15 nm is challenging and requires the optimization of growth conditions (pressure, temperature) to obtain good growth uniformity and crystal quality [C. Merckling et al., 2013]. Rapid melt growth method is another method to overcome a large mismatch of materials. It is based on the deposition, patterning of amorphous GaAs and, therefore, its transformation to a single crystal by melting and solidifying on Si substrates.[C. Shu-Lu et al., 2010]

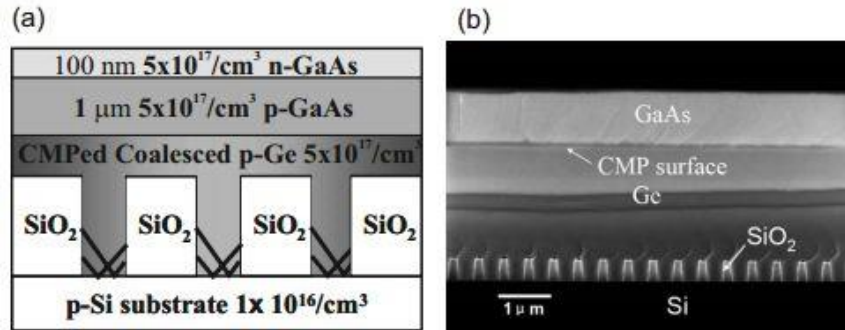


Figure I-7 a) Diagram of epitaxy GaAs on a  $\text{SiO}_2$  patterned silicon substrate using ART method, b) cross-section STEM image of GaAs. Figure is taken from reference [Y. Q. Wu et al., 2008].

Lateral epitaxial overgrowth approach was demonstrated by several groups [Takagi, 2007, [W. Yang et al., 1999, Y. Honda et al., 2002]. This method is based on III-V growth in the limited areas inside of  $\text{SiO}_2$  windows and is illustrated in Figure I-8. Similar to ART method the dislocations are geometrically confined in  $\text{SiO}_2$  walls and as the result, the high-quality III-V materials can be achieved. The relative high electron mobility ( $\mu \sim 480 \text{ cm}^2/\text{V}$ ) using a similar approach (ART and overepitaxy or overgrowth) were demonstrated by Y. Q. Wu [Y. Q. Wu et al., 2008]. The challenges of this method are a reduction of defects (point and antiphase domains), thickness control under ultra-thin regime and control of surface flatness and edge shapes of III-V-OI films [S. Takagi et al., 2007].

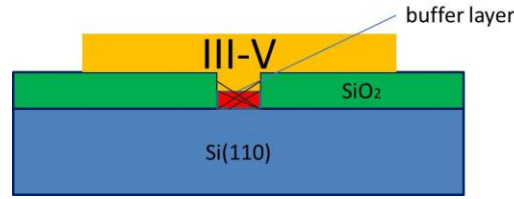


Figure I-8 Diagram of lateral epitaxial overgrowth.

Very recently the gate first-aligned FinFET device using a confined epitaxial lateral overgrowth (CELO) was demonstrated [L. Czornomaz et al., 2015]. A high-quality  $\text{In}_{0.7}\text{GaAs}$  on Si materials and as a result, the good device performance was achieved using this method. Figure I-9 a, b, c shows that the fabrication process of InGaAs material by necking the defects in the seed region.

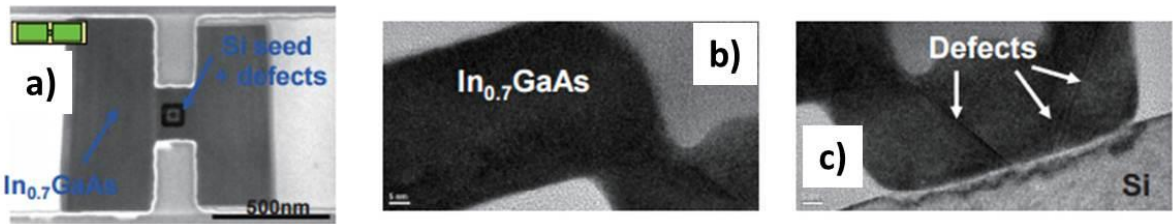


Figure I-9 a) Plan view of the corresponding InGaAs CELO structure, b, c) cross-sectional HR-TEM image confirming that defects are confined in the seed region. Figure is taken from reference [L. Czornomaz et al., 2015].

The first prototype of III-V FinFET devices monolithically integrated on 300 mm Si wafers was demonstrated by IMEC group in 2014 [<http://www2.imec.be>]. Figure I-10 shows the TEM image of high-quality InGaAs layer capped on an InP trench with a width less than 40 nm using ART method. However, the reduction of trench width (less than 40 nm) requires the progress in patterning technology and growth parameters optimization.

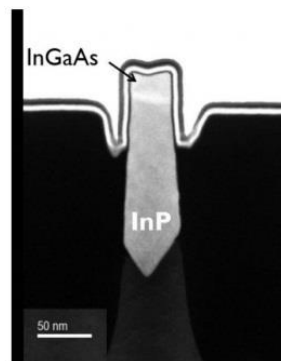


Figure I-10 TEM image of first III-V FinFET devices monolithically integrated on 300 mm Si wafers [<http://www2.imec.be>].

The semiconductor roadmap for 28 nm devices and beyond is focused mainly on FinFET and FD-SOI technology. SOI Industry Consortium [<http://www.soiconsortium.org/>] includes such companies as IBM, IMEC, SOITEC, Freescale, GlobalFoundries. The good cost-to-performance ratio is an important parameter for the semiconductor industry. FD-SOI wafers

are expensive but the integration of devices is found to be very efficient for low power devices. However, the highest performance was achieved with FinFET devices. Recently, the combination of FinFET with SOI was demonstrated as a possible integration approach for III-V channels for 16 nm and 7 nm nodes. The TEM image of this device is shown in Figure I-11. Thus, the different integration approaches of III-V materials on Si platform were developed.

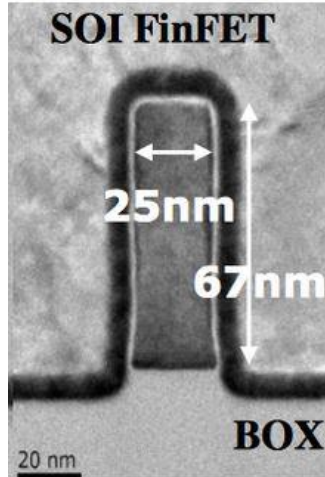


Figure I-11 TEM image of FinFET on SOI device. Figure is taken from [[http://www.eetimes.com/document.asp?doc\\_id=1327035&](http://www.eetimes.com/document.asp?doc_id=1327035&)].

### I.3 Challenges of nano-characterization of channel materials in 2D and 3D architectures

#### I.3.1 Doping profiling in 3D architecture materials

The control of doping is an important issue to achieve high-performance transistors. To obtain the doped source/drain region, ion implantation, vapor phase doping or plasma immersion doping processes are used. The doping process requires the dopant profile optimization (conformal doping) of the source/drain area [J. Mody et al., 2010]. However, the control of dopants incorporation, activation, and self-diffusion in 3D devices is difficult. That's why an improved metrology characterization should be developed for optimization of this doping process. Here, the recently reported metrology for doping measurements in 3D structures/materials is discussed.

Dynamic SIMS is often used to study the doping profiling (e.g. dopant concentration and diffusion) in planar materials due to its excellent sensitivity. SIMS allows the total concentration of dopants to be estimated while techniques such as photoluminescence, Raman spectroscopy, and photoconductivity and scanning photocurrent microscopy and scanning capacitance will give only qualitative information on measured impurities. Additionally, the dopant activation can be studied in a combination in a combination with Hall measurements which give carrier concentration.

High lateral resolution (less than 40 nm) and high sensitivity of detection (less than  $1 \cdot 10^{17}$  at/cm<sup>3</sup>) are required to study the doping in 3D structures. However, most analytical techniques have to be improved in order to provide an accurate quantitative information of dopants in small areas (see Figure I-12). Recently, despite the low SIMS lateral resolution (less than 100 nm) but thanks to its high sensitivity of detection the promising results of doping measurements in 3D structures were reported.

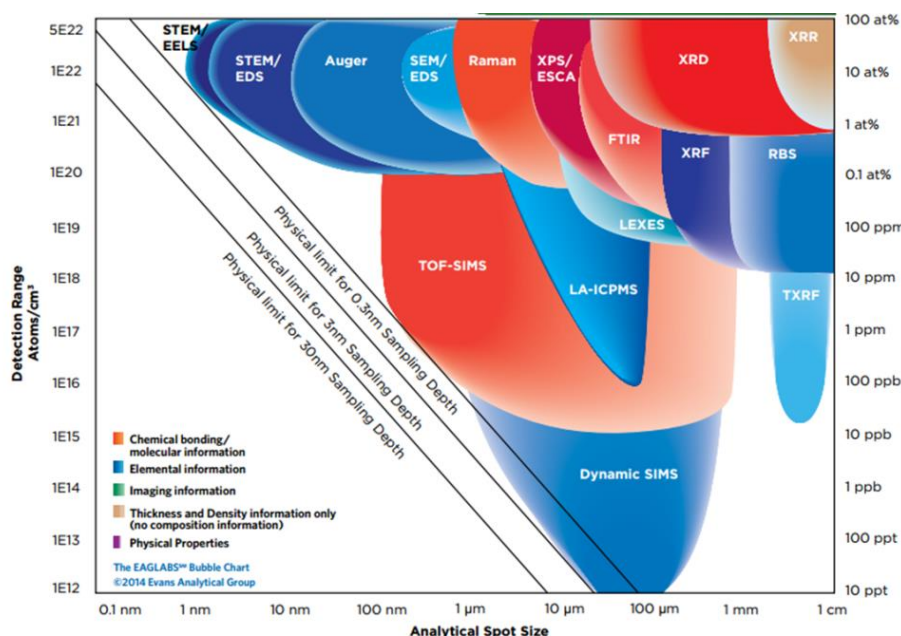


Figure I-12 Analytical resolution versus detection limit for a variety of standard characterization techniques in material research. Figure is taken from [www.eag.com]

Promising results of doping profiling in vertical III-V nanowires (NWs) by profiling ensembles were demonstrated [A. C. E. Chia et al., 2013]. For SIMS experiments, the Cyclotene polymer was used to fill the space between NWs to achieve a smooth and planar top surface. Using the similar approach the doping profiling in fins for FinFET technology was recently reported [W. Vandervorst et al., 2014]. Note that, identical doping distribution (profile) on the top and at the side of fins is required for FinFET technology to optimize the electrical performance of the device. For SIMS experiments, the spaces between the fins were filled by polysilicon and then, the top of the surface was planarized by polishing. SIMS method for fin structures is based on the assumption that recorded SIMS signal from arrays always corresponds to an amount of dopants present at the instantaneous surface [W. Vandervorst et al., 2014]. Figure I-13 illustrates the SIMS profile of B-implantation in fin arrays of 80 nm in width with a doping concentration of  $6\text{--}7 \cdot 10^{21}$  at/cm<sup>3</sup>. To detect dopant in fins structures, the cluster ions can be also used. The Cs<sub>2</sub>As<sup>+</sup> cluster ions using averaging the fins ensembles were used to detect the As doping concentration in FinFETs. [K. A. B. T. Meura et al., 2014].

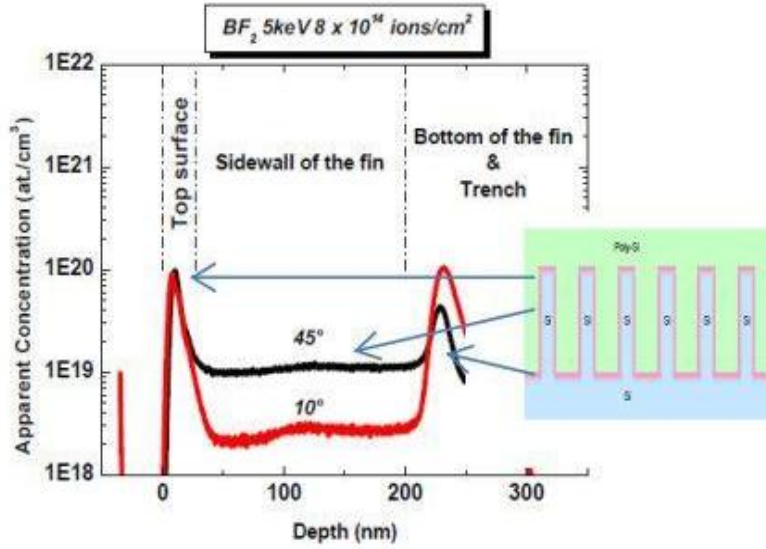


Figure I-13 SIMS profile of B-concentration in Fin arrays, wherein red and black color lines are fin profiles at tilt angles  $10^\circ$  and  $45^\circ$ , respectively. Figure is taken from reference [W. Vandervorst et al., 2014].

The results of dopant clustering and dopant diffusion in FinFET devices were reported using APT technique with high spatial resolution [A. K. Kambham et al., 2013]. The non-conformality of the doping process and the different dopant gradients under the gate at the top and the sidewalls were observed. Overall, APT is a useful technique which gives the information from the very small volume. However, APT analysis of dopants in fins is, in general, difficult due to challenges of sample preparation, poor tip yield, artifacts during the reconstructions and differences in the in the evaporation field of semiconductor/insulator etc. [W. Vandervorst et al., 2014]. Moreover, the main disadvantage of APT compared to SIMS is lower sensitivity of detection. Additionally, there is a need to obtain the dopant information from a large number of fins to optimize the dopant process. Thus, it seems that SIMS is the most adapted technique for doping profiling in 3D devices.

### I.3.2 SIMS profiling of InGaAs materials overview

As was mentioned previously, InGaAs materials are promising high-mobility materials for nMOSFET devices. InGaAs materials grown on Si using the ART approach can be formed ready to use as channels in FinFET or Trigate device architectures. However, the physico-chemical investigation of III-V FinFET devices is very challenging as the channel thickness has to be extremely thin (less than 10 nm). Moreover, the interface abruptness, diffusion, and compositional studies are needed in order to optimize the device performances.

The MOCVD technique is used for selective epitaxy and growth of multilayered structures (superlattices and quantum wells) with abrupt interfaces of superlattices and QWs [C. Gerardi, 1997]. Growth process conditions, such as the gas pressure, temperature, and contamination, were reported to have a large impact on the growth uniformity and crystal

quality of III-V trenches [C. Merckling et al., 2013]. Time to data analysis, the high sensitivity of detection and complexity of measurements are important parameters for material characterization in order to optimize the epitaxy process. Over and above, with scaling tendency and development of non-planar materials, these requirements become more than critical. Additionally, the characterization techniques should have sufficient lateral and depth resolution and concentration precision (less than 3-5%) with new transistor development. For example, over ten years ago the depth resolution for techniques was sufficient to be in the range of 1 to 10 nm for semiconductor analysis while today the depth resolution needs sub-nanometer.

SIMS is a powerful technique and with optimization of analysis conditions give a complete chemical analysis with the relatively high precision of quantification (less than 2-3%). Very recently, SIMS was successfully used to study confined volumes narrow structures with dimensions below 20 nm for FinFET technology applications. [A. Merkulov, 2015, M. Hopstaken, 2015, A. Budrevich, 2015, A. Franquet et al., 2015, A. Franquet et al., 2014]. As mentioned previously, the chemical analysis of such materials is limited by the lateral resolution of standard methods like XPS, SIMS, and RBS etc. The new approach called self-focusing (SF) SIMS was demonstrated in order to study the composition in thin layers in ultra-narrow trenches and to overcome the lateral limitations of SIMS instrument. In general, in standard SIMS approach the major signals are used for quantification of planar layers, whilst in SF-SIMS to determinate the composition the cluster ions are used. Thus, SF-SIMS approach gives the local composition from small areas with high sensitivity. The Ge quantification in trenches (20-500 nm in width) using  $\text{SiGe}^-$  and  $\text{Ge}_2^-$  ion clusters with high accuracy was recently reported [A. Franquet, et al., 2016]. The SF-SIMS approach was also also demonstrated for InGaAs/InAlAs/InP fin structures [A. Franquet et al., 2015]. 1.5-D SIMS metrology was also demonstrated by A. Budrevich [A. Budrevich, 2015]. For the compositional analysis using this method the geometry and dimensions and the narrow structures were considered. Additionally, the spaces between fins were covered by poly or amorphous silicon and SIMS experiments were performed using normal incidence of ion beam.

In conclusion, SIMS instrument has been demonstrated as a suitable and powerful technique for depth profiling of repetitive ensembles which can be used for determining dopant impurity and elemental concentration not only for 2D but as well for 3D structures. These reported results may be implemented in semiconductor manufacturing industry.

## REFERENCES:

- [W. Arden, et al. 2004] More-than-Moore, <http://www.itrs.net/ITRS%201999-2014%20Mtgs,%20Presentations%20&%20Links/2010ITRS/IRC-ITRS-MtM-v2%203.pdf>.
- [M. Bohr, 2014] 14 nm Process Technology: Opening New Horizons, <http://www.intel.com/content/dam/www/public/us/en/documents/pdf/foundry/mark-bohr-2014-idf-presentation.pdf>.
- [A. Budrevich, 2015] 1.5D SIMS methodology for semiconductors technology development, SIMS Conference XX, Seattle, USA.
- [R. Castillo Ojeda, et al. 2007] Growth of  $\text{Al}_x\text{Ga}_{1-x}\text{As}/\text{GaAs}$  structures for single quantum wells by solid arsenic MOCVD system, *Revista Mexicana de Fisica*, **53** (6), pp. 441-446.
- [A. C. E. Chia, et al. 2013] Unlocking doping and compositional profiles of nanowire ensembles using SIMS, *Nanotechnology*, **24** (4), pp. 045701.
- [L. Czornomaz, et al. 2015] Confined Epitaxial Lateral Overgrowth (CELO): A novel concept for scalable integration of CMOS-compatible InGaAs-on-insulator MOSFETs on large-area Si substrates, VLSI Technology Symposium, pp. T172-T1T3.
- [X. Dai, et al. 2014] Novel Heterogeneous Integration Technology of III–V Layers and InGaAs FinFETs to Silicon, *Advanced Functional Materials*, **24** (28), pp. 4420-4426.
- [J. A. Del Alamo, 2011] Nanometre-scale electronics with III-V compound semiconductors, *Nature*, **479** (7373), pp. 317-323.
- [G. Doornbos, et al. 2010] Benchmarking of III-V n-MOSFET maturity and feasibility for future CMOS, *IEEE Electron Device Letters*, **31** (10), pp. 1110-1112.
- [J. G. Fiorenza, et al. 2010] Aspect Ratio Trapping: A Unique Technology for Integrating Ge and III-Vs with Silicon CMOS, *ECS Transactions*, **33** (6), pp. 963-976.
- [A. Franquet, et al. 2014] Quantification of Group IV alloys in confined structures: the self-focusing SIMS approach, SIMS Conference Europe, Muster, Germany.
- [A. Franquet, et al. 2015] Composition analysis of III-V materials grown in nanostructures for semiconductor applications: the self-focusing SIMS approach, SIMS Conference XX, Seattle, USA.
- [A. Franquet, et al. 2016] Self focusing SIMS: probing thin films composition in very confined volumes, *Applied Surface Science*, **365**, pp. 143-152.
- [G. Wang, et al. 2010] Selective Area Growth of InP in Shallow-Trench-Isolated Structures on Off-Axis Si(001) Substrates, *J. Electrochem. Society*, **157** (11), pp. H1023-H1028.
- [C. Gerardi, 1997] SIMS analyses of III-V semiconductor quantum well and superlattice heterostructures, *Surface and Interface Analysis*, **25** (6), pp. 397-403.
- [Y. Honda, et al. 2002] Growth of GaN free from cracks on an (111)Si substrate by selective metalorganic vapor-phase epitaxy, *Applied Physics Letters*, **80** (2), pp. 222-224.
- [M. Hopstaken 2015] Atomic Layer SIMS depth profiling of epitaxial SiGe films: quantification aspects at low impact energy, SIMS Conference XX, Seattle, USA.
- [M. J. P. Hopstaken, et al. 2010] Sputtering behavior and evolution of depth resolution upon low energy ion irradiation of GaAs, *Journal of Vacuum Science & Technology B: Microelectronics and Nanometer Structures*, **28** (6), pp. 1287.
- [A. K. Kambham, et al. 2013 ] Three-dimensional doping and diffusion in nano-scaled devices as studied by atom probe tomography, *Nanotechnology*, **24** (27), pp.275705.

- [H. Ko, et al. 2010] Ultrathin compound semiconductor on insulator layers for high-performance nanoscale transistors, *Nature*, **468** (7321), pp. 286-289.
- [K. J. Kuhn, 2012] Considerations for Ultimate CMOS Scaling, *IEEE Transactions on Electron Devices*, **59** (7), pp. 1813-1828.
- [T. Li, et al. 2010] III–V Compound Semiconductors: Integration with Silicon-Based Microelectronics, CRC.
- [C. Merckling, et al. 2013] Selective area growth of InP in shallow trench isolation on large scale Si(001) wafer using defect confinement technique, *Journal of Applied Physics*, **114** (3), pp.033708.
- [A. Merkulov 2015] Assesment of accurate analysis in low dimensional or confined SiGe structures using low energy dynamic SIMS technique, SIMS Conference XX, Seattle, USA.
- [K. a. B. T. Meura, et al. 2014] Characterization of arsenic PIII implants in FinFETs by LEXES, SIMS and STEM-EDX, International Conference on Ion Implantation Technology.
- [J. Mody, et al. 2010] Dopant and carrier profiling in FinFET-based devices with sub-nanometer resolution in VLSI Technology (VLSIT), 2010 Symposium on, pp. 195-196.
- [D. B. Noble, et al. 1990] Reduction in misfit dislocation density by the selective growth of Si<sub>1-x</sub>Ge<sub>x</sub>/Si in small areas, *Applied Physics Letters*, **56** (1), pp. 51-53.
- [J.-S. Park, et al. 2009] Low-defect-density Ge epitaxy on Si (001) using aspect ratio trapping and epitaxial lateral overgrowth, *Electrochemical and Solid-State Letters*, **12** (4), pp. H142-H144.
- [C. Shu-Lu, et al. 2010] Single-Crystal GaAs and GaSb on Insulator on Bulk Si Substrates Based on Rapid Melt Growth, *Electron Device Letters, IEEE*, **31** (6), pp. 597-599.
- [S. Takagi, et al. 2013] High mobility CMOS technologies using III–V/Ge channels on Si platform, *Solid-State Electronics*, **88**, pp. 2-8.
- [S. Takagi, et al. 2007] Device structures and carrier transport properties of advanced CMOS using high mobility channels, *Solid-State Electronics*, **51** (4), pp. 526-536.
- [R. Terao, et al. 2011] InP/InGaAs Composite Metal–Oxide–Semiconductor Field-Effect Transistors with Regrown Source and Al<sub>2</sub>O<sub>3</sub> Gate Dielectric Exhibiting Maximum Drain Current Exceeding 1.3 mA/μm, *Applied Physics Express*, **4** (5), pp. 054201.
- [W. Vandervorst, et al. 2014] Dopant/carrier profiling for 3D-structures, *Physica status solidi (c)*, **11** (1), pp. 121-129
- [Y. Q. Wu, et al. 2008] Atomic-layer-deposited Al<sub>2</sub>O<sub>3</sub>/GaAs metal-oxide-semiconductor-field-effect transistor on Si substrate using aspect ratio trapping technique, *Applied Physics Letters*, **93** (24), pp. 242106.
- www.itrs.net, International Technology Roadmap for Semiconductors.
- [W. Yang, et al. 1999] Single-crystal GaN pyramids grown on (1 1 1)Si substrates by selective lateral overgrowth, *Journal of Crystal Growth*, **204** (3), pp. 270-274.
- [Z. Zuoming, et al. 2009] Direct integration of III–V compound semiconductor nanostructures on silicon by selective epitaxy, *Nanotechnology*, **20** (3), pp. 035304.



## CHAPTER II

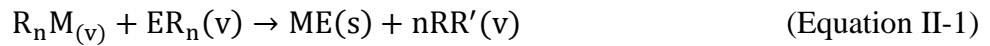
### II. Growth of III-V heterostructures and characterization methods

This chapter describes the basic principles of the growth and characterization techniques as well as the samples used in this thesis. The first section focuses on the epitaxial growth process of III-V heterostructures on Si substrates using MOCVD. The challenges and methods to obtain high-quality III-V layers on Si are underlined. III-V heterostructures grown on planar and non-planar Si wafers studied in this work are also discussed. The second section describes the characterization techniques. Both ToF-SIMS and magnetic sector SIMS are presented. Those techniques were used to investigate the physico-chemical composition of heteroepitaxial structures in 2D and 3D architectures. Finally, the basic principles of APT, Auger and Rutherford backscattering spectrometry (RBS) are explained. APT was used as a complementary technique for 3D reconstruction on single III-V trench whereas Auger and RBS were performed for accurate chemical quantitative analysis of thin III-V trench arrays.

#### II.1 Growth of III-V heterostructures on Si wafers by MOCVD

##### II.1.1 The basic principles of the MOCVD technique

MOCVD is a type of epitaxy process that is often used for the manufacturing of high-speed electronic and optoelectronic devices. In the literature MOCVD may also be referred as metal-organic vapor phase epitaxy (MOVPE). The principle of the MOCVD process is based on the following steps: the vapor phase compounds are introduced firstly into a reactor at approximately room temperature. Then, the precursors are thermally decomposed at high temperatures by a hot susceptor. As a result, the films are formed on a substrate in the reaction chamber. The chemical reaction for the MOCVD process is given by the following equation ([J. Zilko, 2012]):



Where R and R' represent a methyl (CH<sub>3</sub>) or ethyl (C<sub>2</sub>H<sub>5</sub>) radical or hydrogen, M is a Group II or Group III metal, E is a Group V or Group VI element, n=2 or 3 depending on II-VI or III-V growth, and v and s show if the species are in the vapor or solid phase. For example, following the Equation II-1, GaAs can be grown using precursors such as trimethyl gallium (CH<sub>3</sub>)<sub>3</sub>Ga or TMGa and arsine AsH<sub>3</sub>.

Figure I-1 illustrates the main components of the MOCVD system, such as (1) the gas handling system (sources of alkyls or hydrides), (2) reactor chamber, (3) heating system for

pyrolysis temperatures, (4) exhaust system and (5) safety apparatus. In MOCVD, the growth is performed under low pressure (between 15 and 750 Torr) compared to molecular beam epitaxy (MBE) is realized under ultra-high vacuum (UHV).

During the MOCVD growth, the following parameters have to be controlled, which are essential to obtain high-quality semiconductors: (i) the pressure in the reactor; (ii) the growth temperature; (iii) the input reactant molar flow and (iiii) carrier gasses flows. More can be found in reference [J. Zilko, 2012].

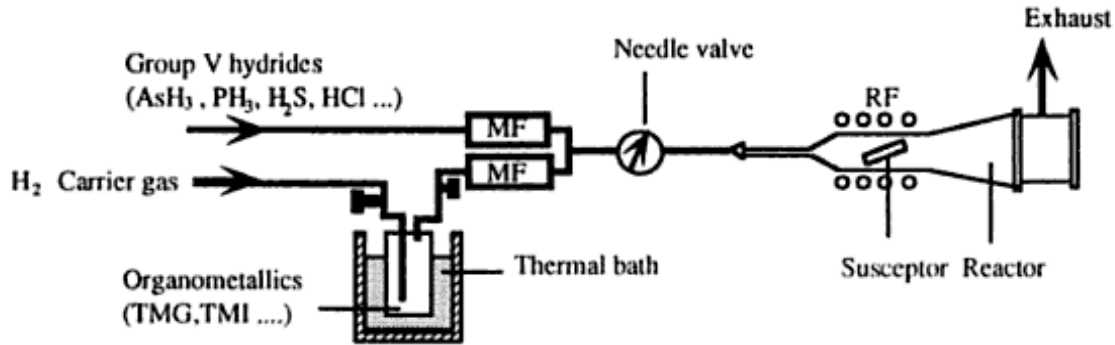


Figure II-1 Schematic diagram of MOCVD technique. Diagram is taken from reference [M. Razeghi, 1995].

One of the features of MOCVD is the possibility to obtain higher growth rates compared to the MBE technique. The growth rate in general strongly depends on the temperature, substrate decomposition, and precursor flow rates and is given for III-V group materials [S. Jiang, et al. , 2014]:

:

$$GR = \frac{dz}{dt} = \frac{(P_{\text{Group III, input}} - P_{\text{eq}})}{N \cdot R \cdot T} \quad (\text{Equation II-2})$$

Where  $z$  is the thickness of deposited III-V materials,  $t$  is the growth time,  $P_{\text{Group III, input}}$  and  $P_{\text{eq}}$  are the input partial pressure and the equilibrium vapor pressure of Group III for the III-V materials:  $N$  is the number of Group III atoms per volume, and  $R$  and  $T$  are the gas constant and the temperature.

To achieve a high growth rate, low molecular weight compounds, e.g. trimethylgallium (TMGa), are used. This is because low molecular weight compounds have higher vapor pressures at a certain temperature than higher molecular weight materials. For example, TMGa has a vapor pressure of 65.4 Torr at 0°C, whereas triethylgallium (TEGa) has a vapor pressure of only 4.4 Torr at the higher temperature of 20°C [J. Zilko, 2012]. The lower vapor pressure of TEGa can be used, for example, during the epitaxy of InGaAsP on InP substrate. Thus, the carrier gas flows have to be adjusted to provide high growth rates.

The features of the MOCVD reactor and experimental details are discussed in the next sections.

### II.1.2 MOCVD reactor

The MOCVD Applied Materials Tool (AMAT) reactor was installed in 2013 in the CEA/LETI clean room as part of a joint research project between AMAT, LETI, and LTM (Grenoble, France). The main feature of this reactor is the ability to grow III-V semiconductors on 300 mm Si wafers. The illustration of the MOCVD cluster tool can be found in APPENDIX II.A. It consists of a Siconi™ cleaning and the growth chambers connected by a transfer robot. An additional Adixen module is installed on this platform to transfer the wafers under vacuum directly from the epitaxy tool to an X-ray photoelectron spectroscopy (XPS) characterization module. The high temperature of 350°-650°C during epitaxy is obtained using lamps and additionally, the temperature of the Si wafer is controlled by pyrometers. The typical pressure in the MOCVD chamber is in the range of 10-600 Torr.

### II.1.3 Challenges of III-V growth on Si wafers

The epitaxial growth of III-V materials on Si wafers has been studied over the past 30 years and remains targeted for micro- and optoelectronic applications. The main difficulties for use in industrial applications are (i) possible formation of antiphase boundaries (APB) due to polar and non-planar character of materials; (ii) high dislocation density resulting from the large lattice mismatch; (iii) difference of thermal expansion coefficients of materials, which leads to thermal stress and possible cracks in thick GaAs layers.

The nucleation of high-quality III-V materials on Si is difficult to achieve due to the growth of a binary zinc-blende (III-V) on a diamond (Si or Ge) structured material [K.Werner, 2014]. In Si, the crystal structure consists of two interpenetrating face-centered cubic sublattices, which are different in spatial orientation. Figure II-2 illustrates the different A, B sublattices.

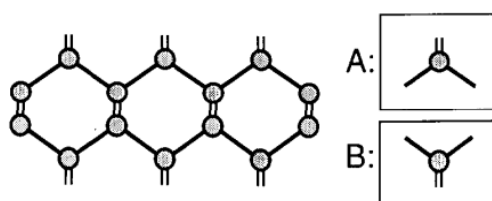


Figure II-2 Two sublattices in a Si crystal. This figure is taken from reference [H. Kroemer, 1987].

In GaAs two sublattices are occupied by Ga and As atoms. In the case of growth on Si, the allocation is changing inside the crystal. The Ga-Ga and As-As bonds for GaAs material can be formed along single-height steps. This structural defect with the sublattice site allocation of atoms opposite to each other is known as an antiphase boundary (APB) that delimits antiphase domains (APDs) (see Figure II-3). [H. Kroemer, 1987], [L. C. Bobb et al., 1966], [P. M. Petroff, 1986]. The growth on Si is shown on a (100)-oriented substrate. Here, the As atoms form strong bonds with Si, while Ga atoms do not, thus the first atomic layer will be an As layer [T. A. Langdo et al., 2000].

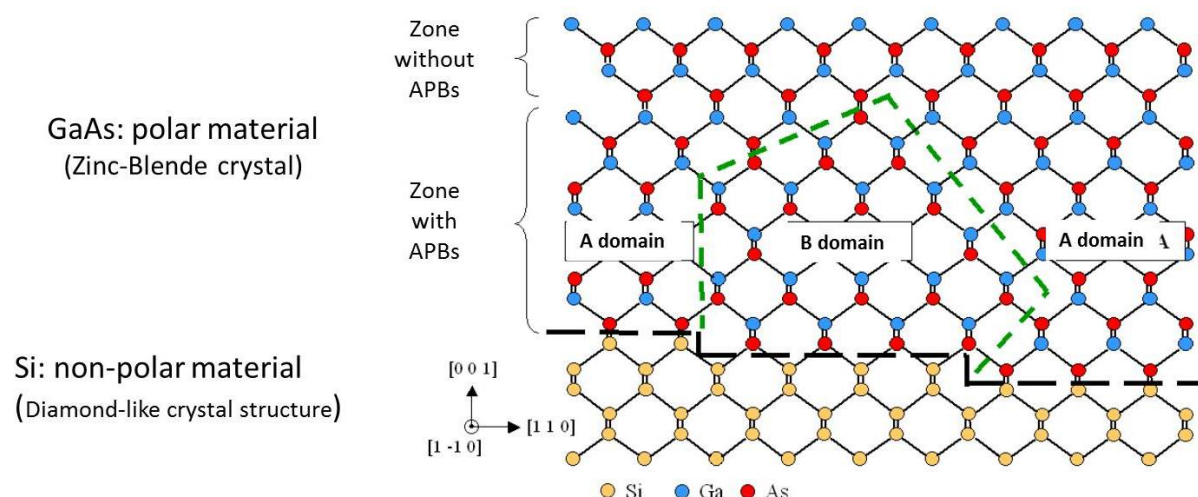


Figure II-3 Mechanism of APB formation during GaAs/Si due to the presence of single-height steps on the Si substrate surface.

To prevent the formation of APB the preparation of the Si surface can be done in two ways: a) by doubling the height of all surface steps using silicon tilted by a few degrees toward (011) ( $0\bar{1}\bar{1}$ ) [R.J. Malik, 2012]; or b) by changing the crystallographic orientation, e.g. to (211), as described by H. Kroemer [H. Kroemer, 1987].

As was mentioned before, the lattice mismatch between GaAs and the Si substrate of 4.1% leads to the formation of dislocations in the GaAs material. The dislocations are formed at the GaAs/Si interface finishing on the film surface as threading dislocations. The lowest density of threading dislocations in GaAs/Si material is approximately  $10^6$ - $10^7$  cm<sup>-2</sup> [J. Zilko, 2012]. Reducing threading dislocations is important to obtain a high-quality material. In 1991 a new method to reduce the propagation of dislocations in GaAs/Si was reported by E.A. Fitzgerald [E. A. Fitzgerald et al., 1991]. This method, known as the epitaxial necking process, is based on the epitaxy of material on small areas so that a dislocation-free surface can be achieved. The principle of epitaxial necking is shown in Figure II-4. To achieve defect-free material on top, the aspect ratio (the ratio of height to width) of the holes in the oxide mask should be higher than 1.4. It allows to block the dislocations and to annihilate the APDs by the oxide sidewall. A defect-free Ge top surface on Si was demonstrated using selective epitaxial growth by T. A. Langdo [T. A. Langdo et al., 2000].

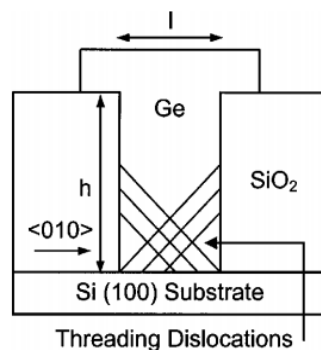


Figure II-4 The principle of epitaxial necking method. The diagram is taken from reference [T. A. Langdo et al., 2000].

Growing lattice mismatched material on a pre-patterned substrate in small areas is found to be attractive for III-V on Si devices. By optimization of lithography and epitaxy processes, high-quality III-V nanostructures on patterned Si, such as InGaAs quantum dots (QDs) [M. Usman et al., 2012], InGaAs QWs [R. Cipro et al., 2014], GaAs nanowires [Q. Li et al., 2015] were demonstrated.

### II.1.4 Sample description

The growth of samples was performed on a 300 mm Si wafers MOCVD Applied Materials tool. The basic principle of MOCVD technique is described section II.1.2. The hydrogen as carrier gas and trimethylgallium (TMGa), aluminium (TMAI), -indium (TMIn) as group-III precursors and tertiarybutylarsine (TBAs) as the group-V precursor were used. The growth was performed in several steps. Firstly, hydrogen was injected into the chamber. The native oxide was removed using the plasma  $\text{NF}_3/\text{NH}_3$  in a Siconi<sup>TM</sup> chamber. Then all gasses were introduced into a reactor and, therefore, the nucleation was performed at low temperatures between 300°C-400°C. The thickness of the nucleation layer was controlled by deposition time. Finally, the temperature was increased above 600°C for the remainder of the growth. Samples were provided by the material integration team from the LTM/CNRS Laboratory.

#### II.1.4.1 InGaAs/AlAs quantum wells on planar Si substrates

The structure of the samples containing nanometer scale InGaAs/AlAs QWs (less than 20 nm in thickness) were grown directly on Si substrates by MOCVD and is schematically shown in Figure II-5. The GaAs buffer layer (400 nm) and AlAs layers (45-50 nm) were used to reduce the number of dislocations close to the GaAs/Si interface. A nominal concentration of 10 % of Indium in the InGaAs layer was targeted during the growth.



Figure II-5 Structure of InGaAs/AlAs QW grown on Si substrate.

The surface morphology of the samples was studied using atomic force microscopy (AFM). A high density of randomly oriented APBs can be seen from Figure II-6. These can be identified

by typical V-groove shapes, which appear at the top of APBs. The surface roughness is measured and given by the root mean square (RMS) (see Table II-1).

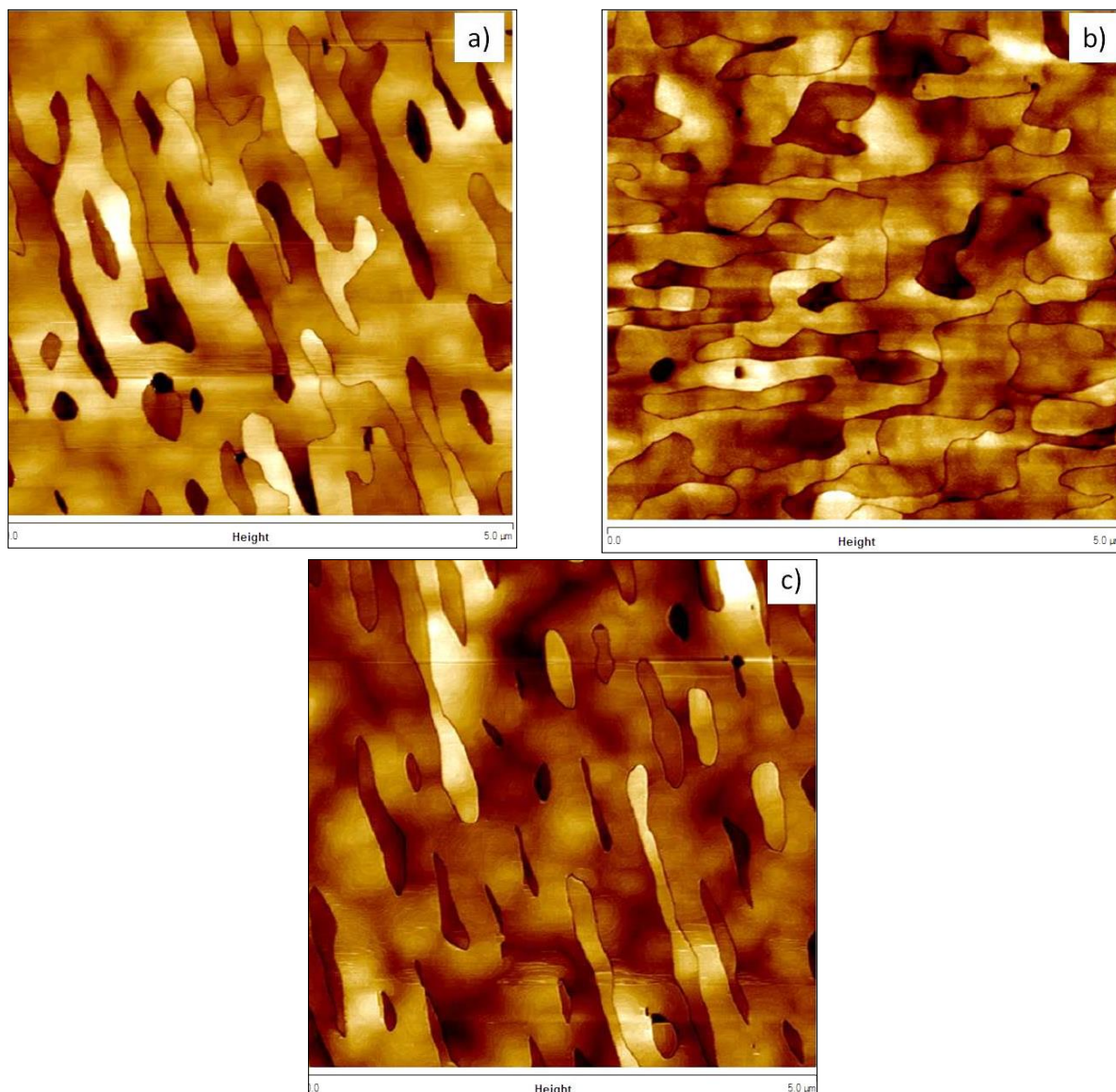


Figure II-6 AFM image of the samples containing InGaAs QWs of different thickness: a) 6 nm, ( $-8.8 \text{ nm} < z < 6.4 \text{ nm}$ ) b) 10 nm ( $-5.1 \text{ nm} < z < 4.7 \text{ nm}$ ) and c) 19 nm ( $-6 \text{ nm} < z < 6.4 \text{ nm}$ ) directly grown on Si substrates by MOCVD.

**Table II-1** RMS measurements of III-V heterostructures grown on Si substrates

Name	InGaAsQW7: 6 nm	InGaAsQW5: 10 nm	InGaAsQW6: 19 nm
RMS	1.6 nm	1.4 nm	2.3 nm

The thickness of each layer was measured by cross-section scanning transmission electron microscopy (STEM) and summarized in Table II-2. As an example, the cross section STEM of an InGaAs QW of 5 nm is shown in Figure II-7.

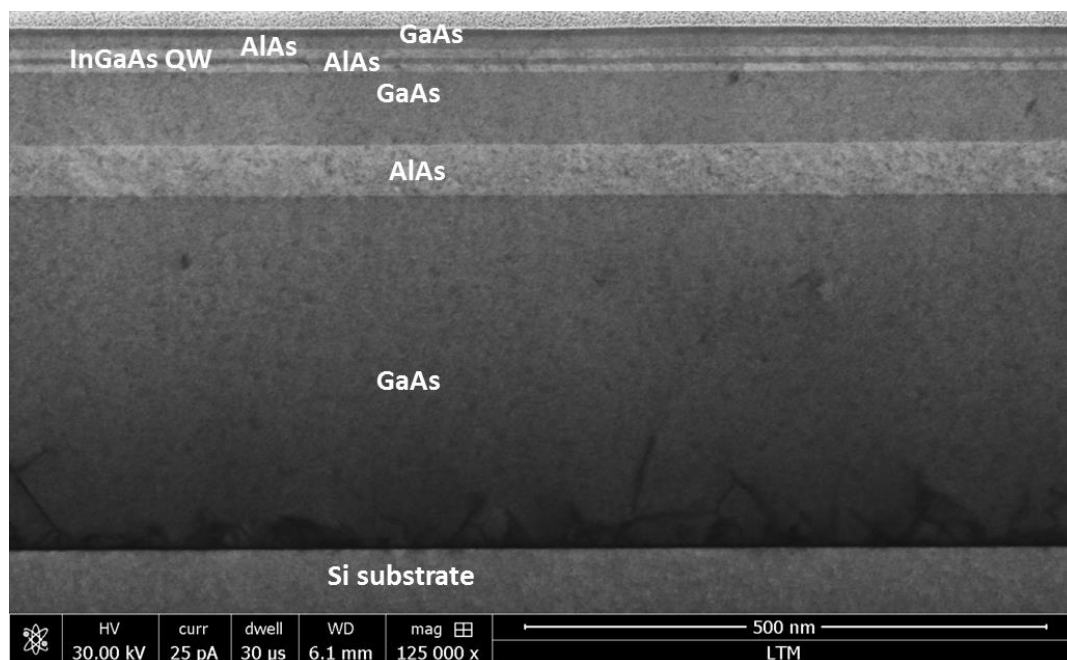


Figure II-7 Cross section FIB-STEM image of InGaAs QW of approximately 5 nm grown by MOCVD on Si substrate.

**Table II-2** Description of III-V samples grown on planar Si wafers by MOCVD

Sample	InGaAsQW5	InGaAsQW6	InGaAsQW7
GaAs(top layer)	20 nm	8 nm	19 nm
AlAs	8 nm	8 nm	8 nm
InGaAs	10 nm	19 nm	6 nm
AlAs	7 nm	7 nm	7 nm
GaAs	81 nm	69 nm	68 nm
AlAs	46 nm	47 nm	49 nm
GaAs	394 nm	347 nm	342 nm

#### II.1.4.2 InGaAs reference samples for quantitative SIMS analysis

The samples were designed as reference samples for quantitative analysis of InGaAs materials using SIMS. The nominal values of  $x=0.05$ ,  $x=0.15$ ,  $x=0.2$  in  $\text{In}_x\text{Ga}_{1-x}\text{As}$  layers were defined during the growth. A Ge buffer layer ( $1.6\ \mu\text{m}$ ) was used to reduce strain due to the lattice mismatch between Si and GaAs layers. Additionally, a reference sample GaAs/Ge/Si was designed for RBS and Particle-induced X-ray emission (PIXE) measurements in order to estimate the composition of each layer and contribution of Ga and As elements in InGaAs/GaAs/Ge/Si sample (see Figure I-8).



Figure II-8 Structure of InGaAs/GaAs/Ge/Si (IGA #1, 2, 3) and GaAs/Ge/Si (GaAs ref #12) samples grown on Si substrate.

Additionally series of  $\text{In}_x\text{Ga}_{1-x}\text{As}/\text{GaAs}/\text{Si}$  samples were used for SIMS analysis and studied by X-Ray diffraction and ellipsometry techniques. The  $\text{Al}_x\text{Ga}_{1-x}\text{As}/\text{GaAs}/\text{Si}$  sample was designed also as a reference sample for SIMS analysis. The GaAs/Si sample was used for RBS and PIXE measurements to estimate the composition of each layer. The summarized data can be found in Table II-3. The thickness of layers was measured using STEM.



Figure II-9 Structure of AlGaAs/GaAs/ Si (AlGa #13) and GaAs/ Si (GaAs ref #14) samples grown on Si substrate.

**Table II-3** Description of series  $\text{In}_x\text{Ga}_{1-x}\text{As}$  standards

Name of standards	Structure of materials	Method of measurement
IGA #1	$\text{In}_x\text{Ga}_{1-x}\text{As}$ : 100 nm/GaAs: 400 nm/Ge:1,6 $\mu\text{m}$ /Si	RBS, PIXE
IGA #2	$\text{In}_x\text{Ga}_{1-x}\text{As}$ : 100 nm/GaAs: 400 nm/Ge:1,6 $\mu\text{m}$ /Si	RBS, PIXE
IGA #3	$\text{In}_x\text{Ga}_{1-x}\text{As}$ : 100 nm/GaAs: 400 nm/Ge:1,6 $\mu\text{m}$ /Si	RBS, PIXE
IGA #4	$\text{In}_x\text{Ga}_{1-x}\text{As}$ : 158 nm/GaAs: 200 nm/Si	XRD
IGA #5	$\text{In}_x\text{Ga}_{1-x}\text{As}$ : 98 nm/GaAs: 200 nm /Si	XRD
IGA #6	$\text{In}_x\text{Ga}_{1-x}\text{As}$ : 76 nm/GaAs: 200 nm /Si	XRD
IGA #7	$\text{In}_x\text{Ga}_{1-x}\text{As}$ : 143 nm/GaAs: 200 nm/Si	XRD
IGA #8	$\text{In}_x\text{Ga}_{1-x}\text{As}$ : 83 nm/GaAs: 200 nm/Si	XRD
IGA #9	$\text{In}_x\text{Ga}_{1-x}\text{As}$ : 113 nm/GaAs: 200 nm/Si	XRD
IGA #10	$\text{In}_x\text{Ga}_{1-x}\text{As}$ : 76 nm/GaAs: 200 nm/Si	XRD
IGA#11	$\text{In}_x\text{Ga}_{1-x}\text{As}$ : 190 nm/InP	Ellipsometry
GaAs ref #12	GaAs: 400 nm/Ge:1,6 $\mu\text{m}$ /Si	PIXE
AlGa #13	AlGaAs: 240 nm/GaAs: 230 nm/Si	RBS, PIXE, PIGE
GaAs ref #14	GaAs: 230 nm/Si	RBS, PIXE, PIGE

### II.1.4.3 Selective growth of III-V heterostructures on non-planar Si-substrates by MOCVD

The III-As based heterostructures were grown selectively in  $\text{SiO}_2$  trenches of different widths on (100) oriented Si substrates. 180-200 nm deep  $\text{SiO}_2$  trenches aligned along the [110] direction with widths ranging from 100 nm to 300 nm were patterned on 300 mm Si (100) substrates using standard e-beam lithography and plasma etching. A stack of GaAs/AlAs/InGaAs/AlAs/GaAs layers was grown under similar epitaxial steps described in section II.1.4.1. The schematic illustration is presented in Figure II-10. The V/III ratio was fixed at a value between 5-50 during the growth.

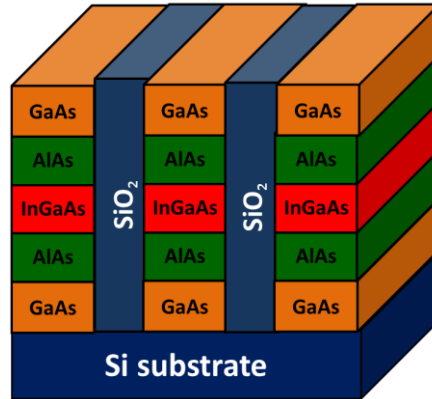


Figure II-10 The schematic illustration of III-V heterostructures selectively grown on non-planar Si wafers by MOCVD.

Figure II-11 a) b) shows the cross-sectional STEM images and top view STEM image, which reveal a good uniformity of the MOCVD selective area growth of III-V heterostructures in this patterned substrate. Figure II-11 a) shows the cross-sectional view of a single trench of width 150 nm, where the stack of GaAs/AlAs/InGaAs/AlAs/GaAs layers can be seen. At the bottom of the trench, many dislocations exist, due to the high lattice mismatch between GaAs and Si. Some threading dislocations may propagate towards the surface, but most of them are blocked in the  $\text{SiO}_2$  walls leading to low defect density in the upper region. Note that the surface is not completely flat and exhibits facets due to the presence of stacking faults. The decrease and even the absence of APBs for III-V trenches with a width of less than 200 nm ( $\text{AR}=0.9$ ) were observed. A good quality of InGaAs layer was confirmed by micro-photoluminescence signals from InGaAs QWs at room temperature.

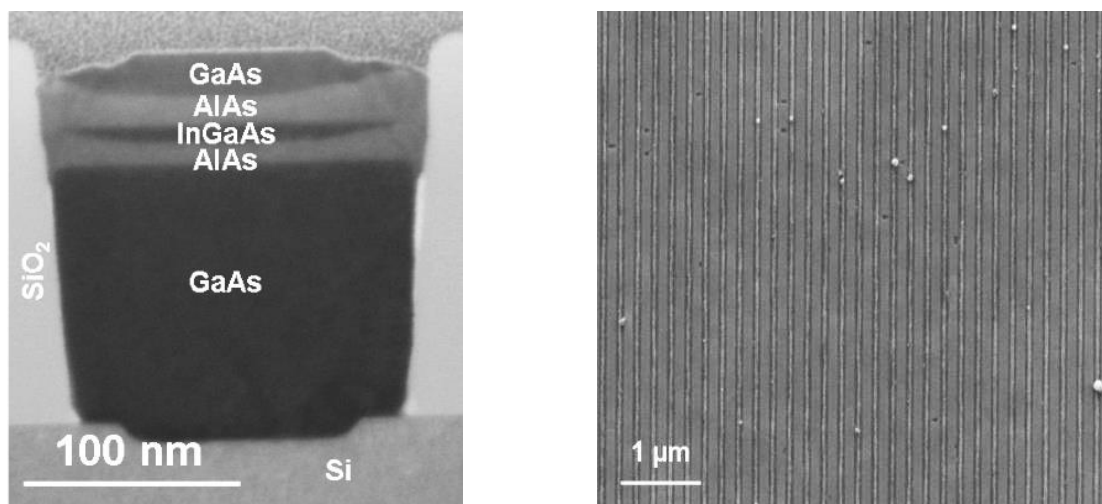


Figure II-11 a) Cross-sectional view of a single trench with a width of 150 nm with the stack of GaAs/AlAs/InGaAs/AlAs/GaAs layers, b) SEM top view of III-V trenches.

#### II.1.4.4 Doping in planar and non-planar samples

Si-doped GaAs samples on planar and non-planar Si substrates were specially designed to study SIMS doping profiling in 2D and 3D architectures. The samples were n-doped during growth with Si concentration of  $4 \cdot 10^{18} \text{ at/cm}^3$ . The schematic structures of the studied samples are presented in Figure II-12. The thickness of Si-doped GaAs region and for non-doped GaAs region was 70 nm and 140 nm, respectively.

The GaAs growth conditions were used under similar conditions described above. Additionally, for Si-doping the silane  $\text{SiH}_4$  gas precursor was used for Si incorporation in GaAs. The concentration of Si doping was controlled by the growth temperature.

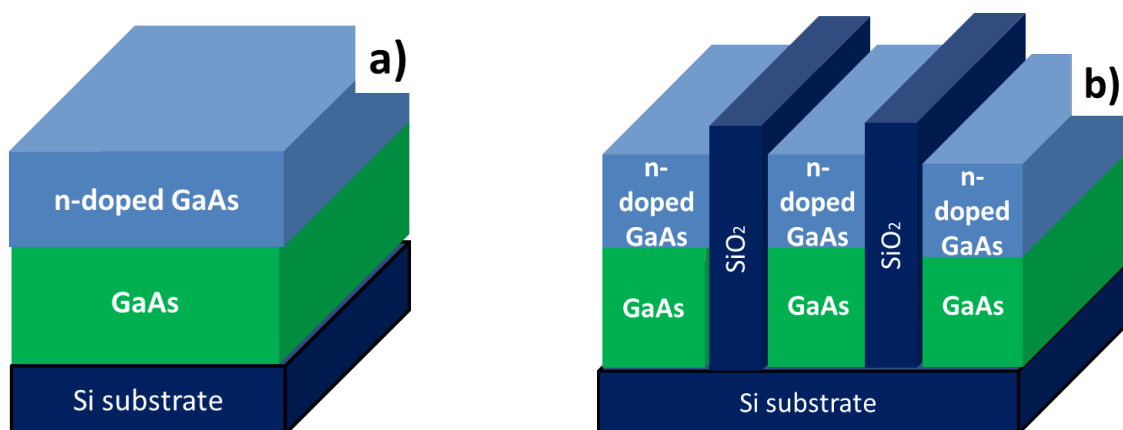


Figure II-12 Si-doped GaAs samples grown on a) planar, b) patterned Si 300 mm wafers by MOCVD. The nominal n-doping level is  $4 \cdot 10^{18} \text{ at/cm}^3$ .

### II.2 Ion beam characterization techniques

#### II.2.1 Secondary ion mass spectrometry

SIMS is an analytical technique used for physico-chemical studies of III-V heteroepitaxial structures in this work. This technique is based on the bombardment of the surface using a focused and energetic primary ion beam and identification of the chemical elements by mass spectrometry of the ejected secondary ions. SIMS is a destructive technique, as atoms are removed from the sample by sputtering, where some of them are ionized (positive or negative) during the bombardment. These are called secondary ions. The fraction of sputtered and ionized particles is very small. The atomic and cluster ions are emitted as secondary ions, over 99% of sputtered species are neutrals. The sputtered ions depend on the relative probabilities of ionization and de-excitation. The high dependence of ion yield (ionization efficiency) on the electronic properties of the sample matrix is called a matrix effect.

The phenomena of the formation of positive ions and neutral atoms for a solid surface under ion beam sputtering was observed by J.J. Thomson in 1910 [J. J. Thomson, 1910]. The energetic primary ions transfer kinetic energy to the target atoms through nuclear collisions while the target atoms are in motion. The displaced atom may transfer a part of its energy to another target atom by a billiard-ball-type collisional process. Some target atoms in the near-surface region with sufficient momentum and energy to overcome the surface bonding energy leave the target. The small fraction of emitted particles or secondary ions is collected and analyzed by a mass spectrometer. Different models exist to explain the secondary ionization processes: electron tunneling, bond breaking, local thermal equilibrium (LTE), and recombination amongst others. The efficiency of secondary ion formation can be represented by a useful yield. It is based on the ratio of the number of detected secondary ions per number of sputtered ions by primary ion bombardment. Useful yield depends on the chemical nature and energy, mass and angle of the primary ion and transmission and mass resolution of the mass analyzer.

SIMS can be classified into static and dynamic types. In static SIMS, the disturbance of the surface is insignificant and the low primary ion current density is used to study the small surface areas. While in dynamic SIMS the continuous bombardment of bulk material is employed [G. Slodzian, 1983]. The basic components of a SIMS instrument include a primary ion source, mass spectrometer, high vacuum sample chamber, an electron gun for charge neutralization, and detectors for detection of secondary ions. Primary ion sources are used to produce the energetic primary ions, such as noble gases ( $\text{Ar}^+$ ,  $\text{Xe}^+$ ), oxygen ( $\text{O}^-$ ,  $\text{O}_2^+$ ,  $\text{O}_2^-$ ), cesium etc. The selection of the primary beam depends on the application addressed. Basically, in dynamic SIMS in order to enhance the ion yield of electropositive and electronegative elements the oxygen and cesium primary ion source are used, respectively. The primary energy and incident angle are related to the number of sputter atoms per incident ion (sputter yield) and ion yield. The erosion or sputter rate is defined as a ratio of the thickness of sputtered layer per time of sputtering. It depends on the surface binding energy of the atoms and a current density of the primary beam and extent on the crystal orientation

and sample temperature. The types of detectors that are commonly used for the detection of secondary ions: (i) the electron multiplier (EM), (ii) the microchannel plate and (iii) the Faraday cup (FC). ToF-SIMS and magnetic SIMS are described in detail in the sections II.2.1.1 and II.2.1.3.

### II.2.1.1 Time of flight mass spectrometry

ToF-SIMS is a technique, which is based on the determination of the mass to charge ratio of ions by measuring their flight times. The pulsing of the primary ion beam is used in most instruments to enable the flight time to be measured. Secondary ions are accelerated by an electrostatic field into a field-free drift tube of length  $l$ , where ions are separated [J. C. Vickerman et al., 2013]. The potential energy  $E_p$  of a charged particle converted to kinetic energy  $E_k$  is following:

$$q \cdot U = \frac{1}{2}mv^2 \quad (\text{Equation II-3})$$

Where  $q$  is the charge and  $U$  is the secondary ion acceleration voltage.

The ion velocity ( $v$ ) can be found from relation of the length of the flight path ( $l$ ) per the time of flight  $t$ :

$$q \cdot U = \frac{1}{2}m \cdot \frac{l^2}{t^2} \quad (\text{Equation II-4})$$

From the previous equations the flight time can be found using:

$$t = l \sqrt{\frac{m}{2 \cdot q \cdot U}} \quad (\text{Equation II-5})$$

Secondary ion flight time depends on the mass to charge ratio, thus, ions with lower masses (with equivalent charge state) will arrive at the detector faster than the heavier ones. The presence of cluster ions should be considered during the SIMS analysis. Often sufficient mass resolution ( $M/\Delta M$ ) must be used to avoid the mass interferences. The mass resolution can be improved using a Reflectron and a Triple Focusing Time of flight (TRIFT) analyzer [P. van der Heide, 2014]. Here, energy filtering is used in the case when ions with the same mass but different kinetic energies (higher velocities) will arrive in the very small time interval.

The ToF-SIMS technique has many applications in the elemental compositional analysis for organic and inorganic materials. The Recent development of polyatomic ion beams, such as

$C_{60}^+$ ,  $Ar_n^+$  ( $n=50-10000$ ) clusters and  $SF_5^+$ , allows to enhance ion yield of organic species and to perform compositional analysis with extremely low damage [J. C. Vickerman et al., 2013].

### II.2.1.2 Experimental conditions

In this work a new generation of ToF-SIMS V ION-TOF instrument was used for chemical depth profiling using sample rotation and 3D imaging of III-V trenches (see Chapter IV.3). The TOF-SIMS analysis was performed using a primary  $Bi_n^+$  at 60 keV source and an  $O_2^+$  sputter ion beam at energy 250-500 eV and incident angle of  $45^\circ$ .

### II.2.1.3 Magnetic sector SIMS

A magnetic sector spectrometer is based on the separation of secondary ions according to their mass/charge ratios. The applied magnetic field (B) is perpendicular to the direction of the ion motion.

$$\frac{m \cdot v^2}{2} = q \cdot U \quad (\text{Equation II-6})$$

The ions pass through the magnetic field. The Lorentz force is equal to the centrifugal force:

$$\frac{m \cdot v^2}{r} = q \cdot v \cdot B \quad (\text{Equation II-7})$$

Where  $r$  is the radius of curvature of ion path. The magnetic analyzer selects the ions according to their momentum.

The velocity can be found by rearranging the previous equation:

$$v = \frac{q \cdot B \cdot r}{m} \quad (\text{Equation II-8})$$

Substituting the Equation II-6 and Equation II-7 the mass to charge is equal to applied magnetic field and the radius of curvature of the ion path and inversely proportional to the ion acceleration voltage.

$$\frac{m}{q} = \frac{B^2 \cdot r^2}{2 \cdot U} \quad (\text{Equation II-9})$$

The separation of secondary ions is based on their mass to charge ratios through the analyzer and is illustrated in Figure II-13.

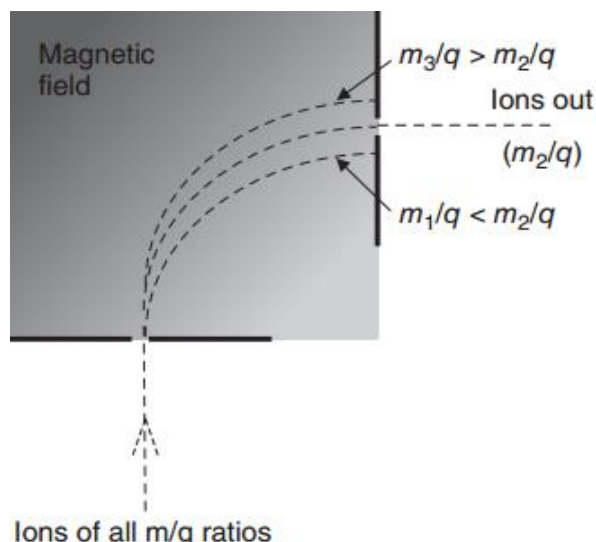


Figure II-13 Schematic of mass filtering in a magnetic sector mass filter. The figure is taken from reference [P. van der Heide, 2014].

When the ions have different kinetic energy, they will follow different trajectories through the magnetic field, this is called energy dispersion. To compensate the energy dispersion of the magnetic field the electrostatic sector analyzer (ESA) is used [A. Benninghoven et al., 1987]. This principle is called a double focusing spectrometer. The electric field energy dispersive effect can be found from the non-mass dependent equation [CAMECA, 2014]:

$$r = -\frac{2U}{E} \quad (\text{Equation II-10})$$

Where  $r$  is the trajectory curvature radius and  $r=8.5$  cm for a magnetic sector SIMS SC-Ultra instrument. The electrostatic lens (coupling lens or spectrometer lens) are placed between the ESA and the magnet to reduce the energy dispersion (Figure II-14).

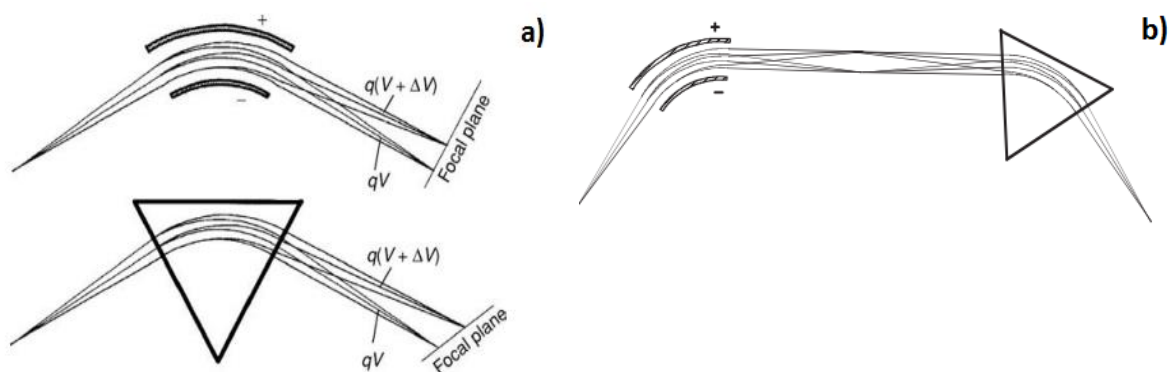


Figure II-14 a) Schematic diagram of energy dispersion in an electric sector ( above) and in a magnetic sector (below), b) Double focusing as a combination of magnetic and electric sectors. The figure is taken from reference [E. de Hoffmann et al., 2007].

The main advantages of magnetic sector SIMS are the higher sensitivity of detection (less than  $1 \cdot 10^{15}$  at/cm<sup>3</sup>) and high mass resolution  $\Delta M/M=10000$ . However, achieving high mass

resolution by closing the exit slits decreases detection sensitivity. The main disadvantage of most magnetic SIMS techniques, such as IMS 7F, SC Ultra, IMS 1280-HR, is low sub-micron lateral resolution. For instance, to improve the spatial resolution the special instrument, the Cameca NanoSIMS 50L was developed. The high spatial resolution of better than 50 nm using  $\text{Cs}^+$  primary ions can be achieved thanks to a coaxial optical design of the ion gun [P. Hoppe, 2006]. It is important to note that the NanoSIMS instrument has parallel acquisition of masses while the sequential acquisition is used for most magnetic SIMS.

### II.2.1.4 Instrumentation of Cameca SC-Ultra magnetic SIMS

The Cameca SC-Ultra is an instrument developed for the characterization of advanced semiconductor materials (Cameca, France). (Appendix II. B). This instrument is designed to achieve extremely low primary beam impact energy (EXLIE). Thus, profiles of shallow implants, dopant, and thin layer materials can be obtained with excellent depth resolution (better than 1-2 nm/decade) and high sensitivity [W. Vandervorst, 2008, A. Merkulov, 2013]. As an example, Figure II-15 shows a profile of boron delta-doped layers measured using the RF-plasma oxygen source with sub-nm resolution. High depth resolution profiling using low energy ion beam sputtering is one of the most common applications of Cameca SC-Ultra technique.

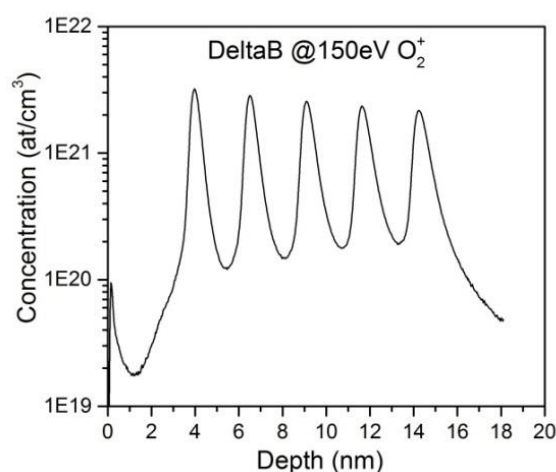


Figure II-15 High depth resolution profile of boron delta layers in silicon using 150 eV  $\text{O}_2^+$  ion beam sputtering in Camera SC-Ultra instrument.

The Cameca SC-Ultra ion optics consist of a 60° floating column (commonly mounted with a cesium source) and a 36° column (commonly mounted with an oxygen Radio Frequency (RF) plasma ion source) and the secondary ion optics (Appendix II. C). The primary ion beam sources are described in detail below. The variable rectangular ion beam shape can be produced by both columns. To form the ion beam spot from the ion source to the sample plane, the ion optics contain a set of electrostatic lenses.

In the non-floating column the space between two lenses are at ground potential [CAMECA, 2014]. The usual primary column cannot work at low impact energy when primary ions are of positive polarity and the sample voltage is required to be negative. If the negative voltage of -3 keV is applied to the sample and +500 eV of impact energy is required, then the source will be at -2.5 kV voltage. Thus, the floating voltage (Float Volt) of -6.3 kV can be used at an acceleration voltage of +3.8 keV and, as a result, the primary energy of 500 eV will be obtained. The principle is illustrated in Figure II-16. The floating column can be biased at any voltage.



Figure II-16 Illustration of the principle of work of floating column.

The cesium microbeam source is based on cesium carbonate ( $\text{Cs}_2\text{CO}_3$ ) contained in a reservoir heated to  $400^\circ\text{C}$  to release the cesium vapor. In contact with the surface of a tungsten plate at a temperature of  $1100^\circ\text{C}$  the cesium vapor ionizes into Cs positive ions. Then,  $\text{Cs}^+$  ions are extracted and accelerated by the applied electric field. (Figure II-17)

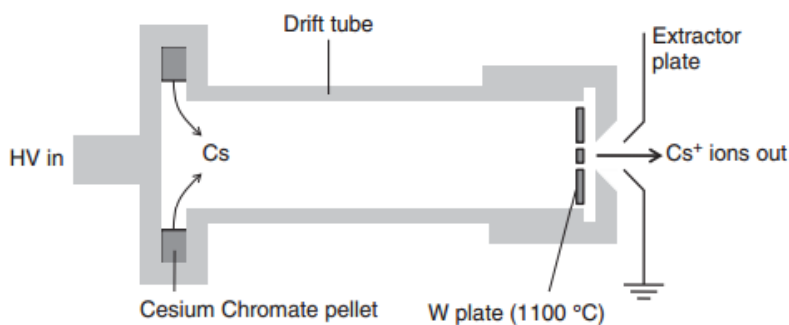


Figure II-17 Illustration of the principle of cesium microbeam. The figure is taken from reference[P. van der Heide, 2014].

The RF plasma ion source is produced by Hyperion™. The H100 Ion Source is mounted on the  $36^\circ$  column. This oxygen source has high brightness and current at low impact energy compared to the duoplasmatron source. The principle of the RF plasma source is based on the magnetic field (B) produced by the RF current flowing through the antenna that induces an RF magnetic field, which penetrates through the dielectric. According to Maxwell-Faraday's law, the time-varying RF magnetic field induces an azimuthal electric field E [P. van der Heide, 2014, N. S. Smith et al., 2007]:

$$\nabla \times \mathbf{E} = -\frac{\partial \mathbf{B}}{\partial t} \quad (\text{Equation II-11})$$

The electric field induces a current in the plasma and causes an ionization of the resident gas molecules (see Figure II-18). Different gas species such as Xe and O<sub>2</sub> can be used. Oxygen produces positive ion beams, which are composed of O<sub>2</sub><sup>+</sup> and O<sup>+</sup>. The abundance ratio O<sub>2</sub><sup>+</sup>/O<sup>+</sup> is very high and approximately 5 (or 18-20% of O<sup>+</sup> approximately) [CAMECA, 2014].

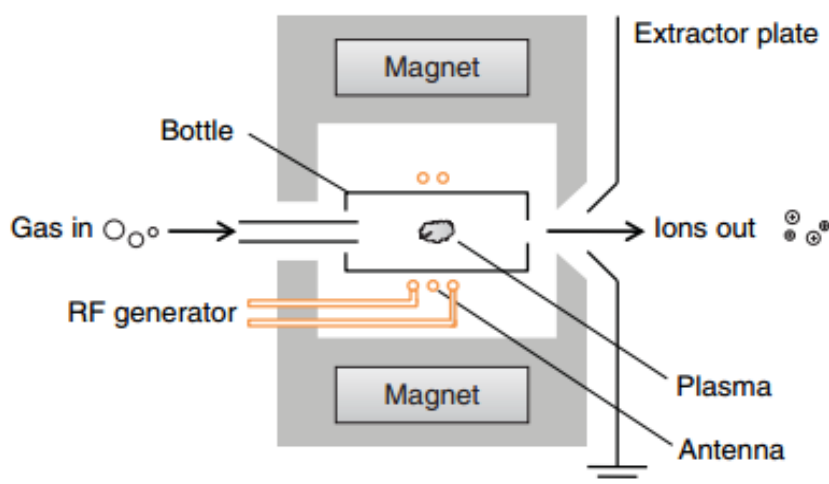


Figure II-18 Illustration of the RF plasma source. The figure is taken from reference [P. van der Heide, 2014].

The secondary ion optics of the SIMS SC-Ultra consist of [CAMECA, 2014]: (i) the matching transfer optics, which consists of lenses to match the emitted secondary beam to the mass spectrometer; (ii) the double focusing mass spectrometer, which contains a magnet and an electrostatic sector (ESA) and Exit Slits; (iii) the projection ion optics used to project the ion sample image onto a microchannel plate. A schematic diagram of the secondary ion optics is presented in Appendix II.C.

### II.2.1.5 Experimental conditions

III-V heterostructures on Si substrates were studied using the SIMS SC-Ultra instrument. The SIMS measurements were performed under oxygen and cesium sputtering. The primary oxygen ion beam was used with energy range 5 keV to 250 eV was used. The contrast and field apertures were fixed to 100 μm and 400 μm, respectively. The entrance and exit slits were fixed at 400 μm and 600 μm. The energy slits were optimized as well. SIMS analysis conditions using the oxygen primary source are presented in Table **III-4**

**Table II-4** SIMS analysis parameters under oxygen ion beam sputtering

Primary source	Primary ion acceleration voltage (V)	Sample voltage (kV)	Impact energy (eV)	Angle of incidence, °	Ion current (nA)	Raster size (μm)	Beam density (μA/μm <sup>2</sup> )
O <sub>2</sub> <sup>+</sup> plasma	8000	3000 polarity +	5000	40	21 ± 0.1	250±2	0.34
O <sub>2</sub> <sup>+</sup> plasma	4000	3000 + polarity	1000	39	26 ± 0.1	250±2	0.41
O <sub>2</sub> <sup>+</sup> plasma	3500	3000 polarity +	500	42	25 ± 0.1	200±2	0.63
O <sub>2</sub> <sup>+</sup> plasma	3250	3000 polarity +	250	50	29,6 ± 0.1	200±2	0.74

The cesium ion beam sputtering using MCs<sup>+</sup> mode using the energy of cesium source in a range of 1 keV to 250 eV was used. The field and contrast apertures were fixed at aperture values of 200 μm 750 μm respectively. SIMS analyzes conditions using the cesium beam are presented in Table III-5.

**Table II-5** SIMS analysis parameters under cesium ion beam sputtering

Primary source	Primary ion acceleration voltage (V)	Sample voltage (kV)	Impact energy (eV)	Angle of incidence, °	Ion current (nA)	Raster size (μm)	Beam density (μA/μm <sup>2</sup> )
Cs <sup>+</sup> non-floating mode	4000	3000 polarity +	1000	63.4°	18± 0.1	250±2	0.3
Cs <sup>+</sup> floating mode	3800	3000 polarity +	500	65.5°	15± 0.1	250±2	0.24
Cs <sup>+</sup> Floating mode	1800	2000 polarity +	250	69°	13± 0.1	250±2	0.2

### II.2.1.6 Depth calibration

The x-axis (time in seconds) is calibrated using the sputter rate (SR). The SR is defined as the relation of depth of sputtered material to sputtering time.

$$SR = \frac{d[nm]}{t[s]} \quad (\text{Equation II-12})$$

The sputter rate depends on the mechanism of energy transfer to the sample ( a type of primary energy, mass, angle of incidence etc.) [R. G. Wilson et al., 1989]. For example, for equivalent conditions, the sputter rate is higher using cesium bombardment than with oxygen bombardment. The primary ion beam and raster size should be considered during the sputter rate measurements. As sputter rate is directly proportional to the primary ion beam current and inversely proportional to the raster area. Hence, sputter rate can be increased by increasing the primary ion current and decreasing the raster size (area).

Sputter rate can be calculated from the film thickness. In the case when the thickness is unknown, surface profilometry measurements can be used. In this case, the depth of the resulting crater corresponds to the thickness of the layer. Figure II-19 shows the image of a crater measured using the 3D optical SensoScan profiler used for depth calibration in this thesis.

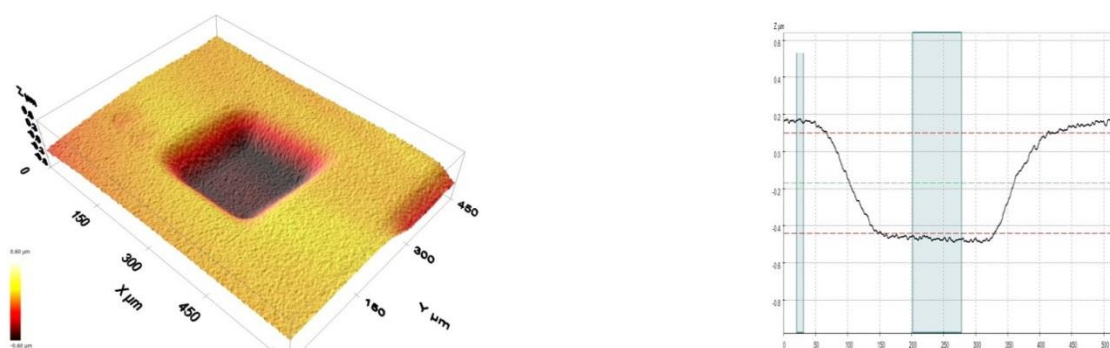


Figure II-19 Image of the crater after Cs ion beam sputtering using 3D optical SensoScan profiler.

Multicalibration or point-by-point calibration is mainly used for multilayers structures. Thus, the sputter rate of each monolayer should be defined.

### II.2.2 Atom probe tomography

Atom probe tomography (APT) is based on an atom by atom-field evaporation from a sharply pointed sample. It is expected to be one of the tools of choice for the analysis of current and future devices in terms of morphology and composition in three dimensions [D. Blavette et al., 1993, Gault B. et al., 2012].

It can be considered as a quantitative 3D chemical high-resolution microscope, with a field of view (FOV) up to 150 nm, that allows the spatial distribution of atoms in a sample to be mapped in 3D with a sub-nanometre scale ( $< 0.5$  nm).

This technique is based on the field evaporation effect requiring the sample to be prepared in the form of a needle with a small curvature radius ( $R < 50$  nm) and is illustrated in Figure II-20. This tip is submitted to an electric voltage ( $V \sim 1-15$  kV) leading a high electrical field ( $E$ ) of several ten volts per nm at the sample surface:

$$E = \frac{V}{\beta \cdot R} \quad (\text{Equation II-13})$$

Where  $\beta$  is a geometric factor due to tip shape.

The use of ultra-fast laser pulses added to the electrical voltage allows the control and ionization of surface atoms up to a time and spatially resolved detector. The measure of the time of flight ( $t_v$ ) allows the chemical identification of ions ( $m/n$ ) by time of flight mass spectrometry to be determined:

$$n \cdot q \cdot V = \frac{1}{2} \cdot m \cdot v^2 \quad (\text{Equation II-14})$$

Where  $n$  is the number of electrons removed in the field ionization process,  $V$  is the applied voltage to the specimen,  $m$  and  $v$  are the mass and velocity of the ion.

The velocity of ions can be found through the relation of the flight distances  $d$  from the specimen to the single-atom detector per the time  $t_v$ . Thus, Equation II-14 is given by:

$$\frac{m}{n} = 2 \cdot V \cdot \left(\frac{t_v}{d}\right)^2 \quad (\text{Equation II-15})$$

The coordinates of ion impacts on the detector give access to the initial position of ions at the tip surface. The depth is obtained from the total number of cumulated ions. Hence, a 3D mapping of the spatial distribution of atoms is obtained.

The focused ion beam (FIB) method is used for the preparation of a needle-shaped tip with a radius of curvature of less than 50-100 nm for APT analysis. The focused gallium ion beam is often used for milling of the specimen. The preparation of a needle-shaped tip for APT analysis is described in detail in the next section.

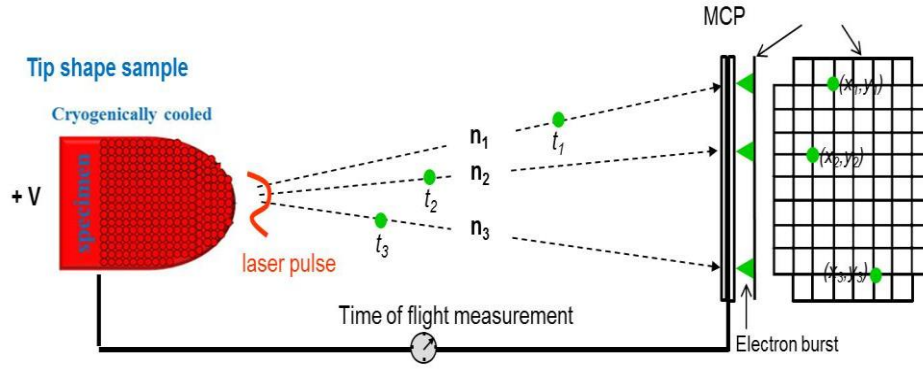


Figure II-20 Illustration of the principle of atom probe tomography.

### II.2.2.1 Sample preparation for APT using the focused ion beam technique

FIB preparation was used to prepare a needle-shaped tip containing an InGaAs/AlAs QW of 9 nm selectively grown on patterned Si wafers (see Figure II-21 shows the different steps of preparation of a needle-shaped tip using FIB milling. The preparation of a tip was performed using a FEI<sup>TM</sup> dual column FIB instrument with a scanning electron microscope (SEM). To protect the sample from Ga<sup>+</sup> ion beam damage a layer of nickel was deposited on top of the region of interest (Figure II-21 a). After it, two parallel trenches were milled to obtain a thin lamella containing the III-V trenches (Figure II-21 b, c). This lamella was welded to the micromanipulator Figure II-21 d) and extracted.

This lamella was then welded to the top of a support tip (Figure II-22 a). The next step of the preparation is based on the annular milling perpendicular to the support point. Therefore, different milling steps are used to reduce the radius of curvature by reducing the ion beam current and interradius of the milling, pattern to gradually reduce the sample diameter (Figure II-21 b, c). The last step of preparation is a cleaning of the tip using low tension to reduce the damage from Ga implantation (Figure II-22 d). After preparation, a radius of curvature of less than 50 nm was obtained.

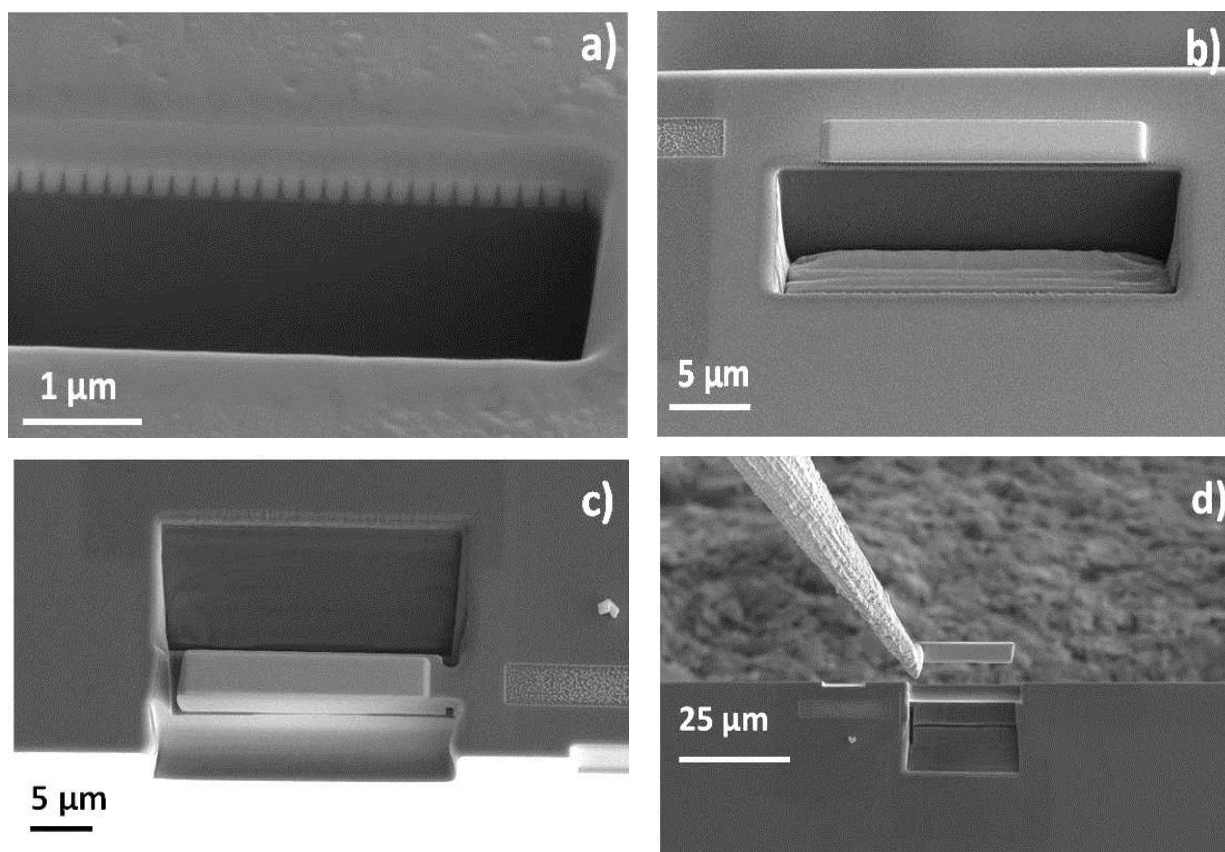
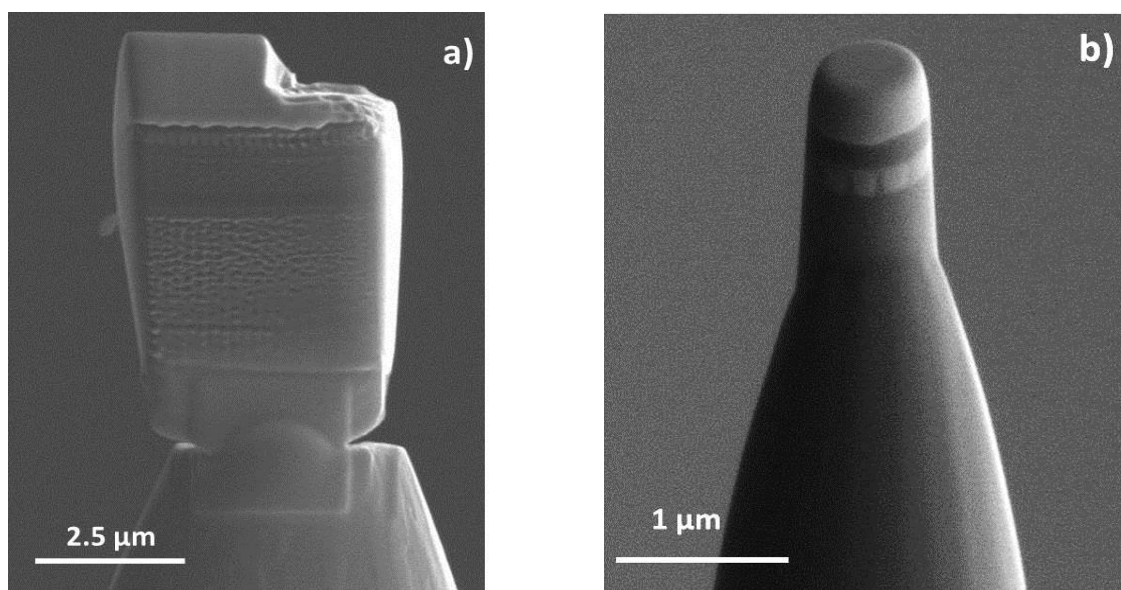


Figure II-21 Illustration of the lift-out steps of preparation of selectively grown InGaAs QW of 9 nm on non-planar Si 300 mm substrate.

Note that during the FIB preparation the ions from the liquid metal ion source are implanted into the surface layers of the specimen but this effect is greatly reduced by the final low energy cleaning step.



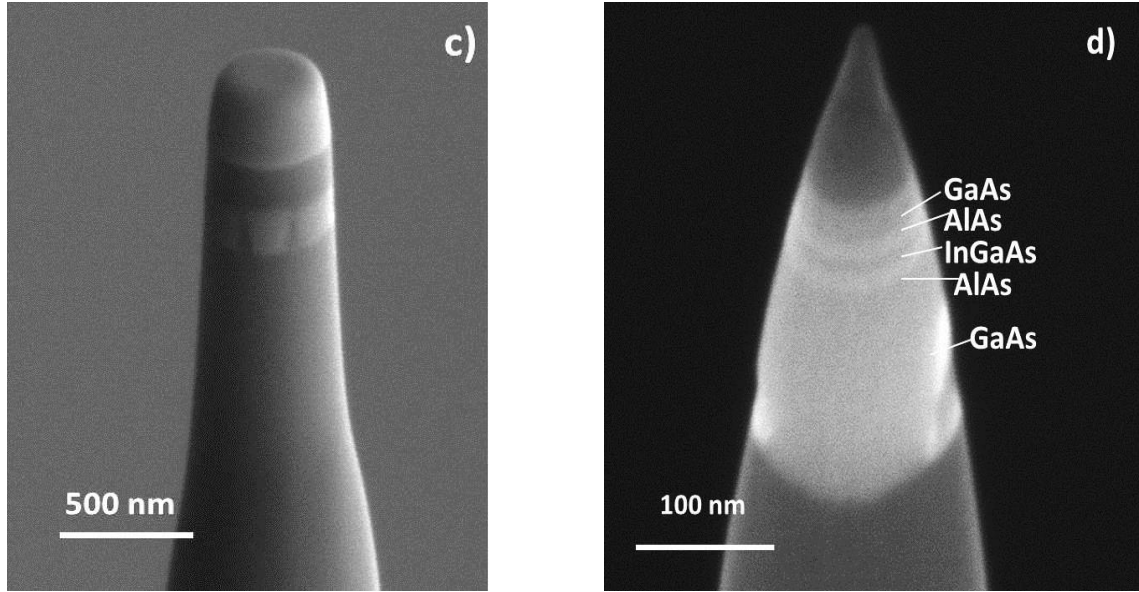


Figure II-22 Preparation of a needle-shaped tip from a sample containing selectively grown InGaAs QW of 9 nm in thickness using FIB milling: a) the lamella is welded to the top of a support tip, b), c) the reducing the sample diameter, d) cleaning of the tip.

### II.2.2.2 Experimental conditions

A needle-shaped tip described above was studied using APT. APT measurements were performed using a Cameca FlexTAP instrument. The laser was operated at a UV wavelength (343 nm) and a pulse frequency of 100 kHz and energy below 1 nJ/pulse. The sample was cooled at 20 K to minimize surface migration of atoms that may deteriorate spatial resolution.

### II.2.3 Auger technique

The Auger technique is a surface characterization technique, which can be used for chemical quantitative depth analysis of nanostructures with its high lateral (less than 10 nm) and depth resolutions (less than 2nm) [E. Martinez et al., 2013], [W. Hourani et al., 2015]. The principle is based on the Auger effect. The sample is hit by an electron beam ( $E_p$ ) of 3-20 keV in energy causing the ejection of a core electron from the energy level K, thus leaving behind a hole in the core level K by ionization. For this,  $E_p$  has to be more than  $5E_k$  for efficient ionization. The core hole can be filled by an electron from the energy level  $L_1$  releasing an amount of energy ( $E_k - E_{L1}$ ), which can be transferred to a third electron. In this case, the third electron in the  $L_{2,3}$  shell will be then ejected with energy ( $E_k - E_{L1} - E_{L2,3}^*$ ) (see Figure II-23). This ejected electron is called an Auger electron and the energy of this electron is given by [D. Briggs et al., 1990]:

$$E_{KL1L2,3} = E_K - E_{L1} - E_{L2,3}^* \quad (\text{Equation II-16})$$

Where  $E_i$  is the binding energies of its atomic energy levels

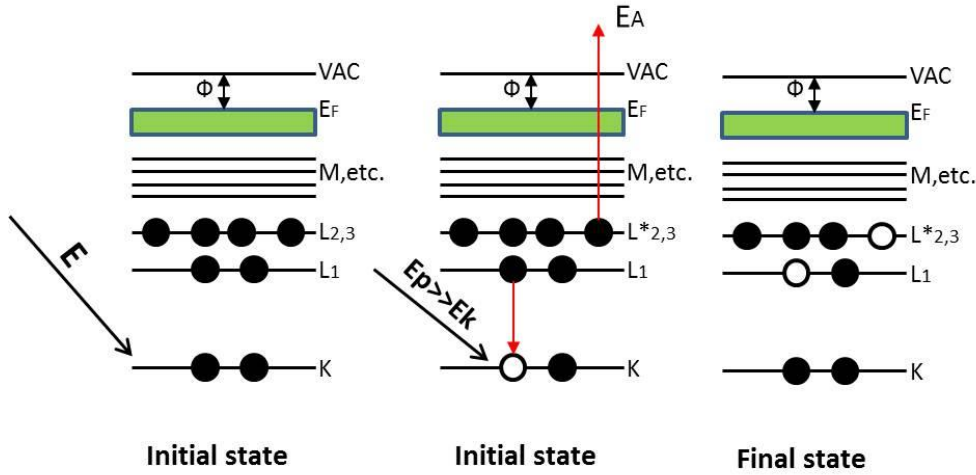


Figure II-23 Schematic diagram of Auger emission.

The probability of releasing an Auger electron depends on the atomic number  $Z$ . Since the probability of transition radiation increases with increasing  $Z$  ( $Z > 10$ ), the probability of an Auger transition is decreasing [D. Briggs et al., 1990]. For Equation II-16, it can be seen that the Auger energy is a function only of atomic energy levels. By knowing the energy of each atom, all the peaks can be easily identified, except for hydrogen and helium.

The electron leaving the sample should overcome the scattering interactions with electrons in the solid, which depend on the energy of the transported electron and the matrix electron density. The surface sensitivity of Auger electron spectra depends on the short inelastic mean free path (4-50 Å) of the Auger electrons [D. Childs et al., 1995].

Auger electrons leave the sample in the near surface region of less than 5 nm. Figure II-24 shows the “pear” shape where the different regions of backscattered electrons, X-Rays, and Auger electrons are presented after interaction of the high energy electron beam and a solid material. Diminishing the electron energy reduces the interaction volume and transforms to a more spherical shape.

Auger intensity for the  $E_k - E_{L1} - E_{L2,3}^*$  transition of the element is given [D. Childs et al., 1995]:

$$I_{\text{Auger}} \approx I_0 \cdot N_i \cdot G(r \cdot \sigma \cdot \gamma \cdot \lambda) = I_0 \cdot N_i \cdot S_i \quad (\text{Equation II-17})$$

Where  $I_0$  is the primary electron beam current,  $N_i$  is the density,  $r$  is the secondary ionization of scattered electrons,  $\sigma$  is the ionization cross section,  $\gamma$  is the Auger transition probability,  $\lambda$  is the inelastic mean free path,  $G$  is the instrumental factor (detector efficiency and analyzer transmission).

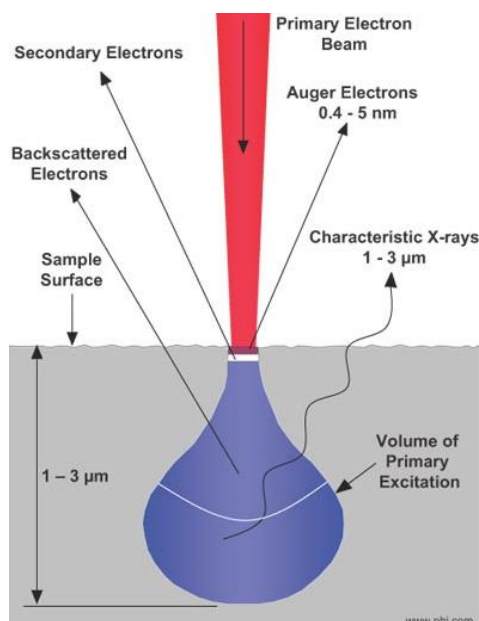


Figure II-24 The basic principle of emission of Auger electrons. The figure is taken from reference [D. Childs et al., 1995].

To find the relative atomic concentration from Auger spectra, the following relation is used [D. Childs et al., 1995]:

$$X_a = \frac{I_a/S_a}{\sum_k I_k/S_k} \quad (\text{Equation II-18})$$

Where  $I_k$  is the intensity of element of interest,

Auger is often used for chemical compositional analysis of nanomaterials. The main advantage of this technique over the static and dynamic SIMS is the possibility to obtain quantitative information about the composition of a material without standard reference samples. Although the use of reference samples can improve the quantitative analysis.

### II.2.3.1 Experimental conditions

The Auger experiments were carried out using a PHI 700Xi Auger nanoprobe equipped with a co-axial cylindrical mirror analyzer. An SEM image is obtained while scanning the surface of the sample by the electron beam. The measurements were performed with an incident electron beam at 10 kV and 1 nA (probe size  $\sim 30$  nm) with a tilt angle of  $30^\circ$ . For depth profiling the sputtering using  $\text{Ar}^+$  ions at an energy of 500 eV (500 nA) with a raster size of  $1 \times 1 \text{ mm}^2$  was performed.

The series of RBS standard samples described in II.1.4.2 were studied in order to evaluate the relative sensitivity factor (RSF) of Al, In and Ga elements in InGaAs and AlGaAs semiconductors.

Auger measurements were carried out on an individual III-V trench and area of  $30 \times 30 \mu\text{m}^2$  that averages several trenches. In-depth composition profiles were measured by combining ion sputtering and Auger electron spectroscopy, acquiring the following Auger lines: In (MNN) at 404 eV, Ga (LMM) at 1070 eV, As (LMM) at 1228 eV, Al (LMM) at 1396 eV, O (KLL) at 510 eV, C (KLL) at 272 eV and Si (KLL) at 1619 eV.

### II.2.4 Rutherford backscattering spectrometry

RBS is a non-destructive quantitative chemical technique. The technique is named after Ernest Rutherford who studied the backscattering of alpha particles through metal foils. Later on, the nuclear scattering and nuclear reactions by high energy protons and deuterons were implemented for analysis of solid surfaces by the group of Rubin [S. Rubin et al., 1957]. The principle of the technique is based on the elastic scattering of high energy ions from target atoms. The energy  $E$  of the backscattered projectile is defined by:

$$E = k \cdot E_0 \quad (\text{Equation II-19})$$

Where  $E_0$  is the initial energy and  $k$  is the kinematic factor.

As the mass of the projectile is known and assuming the elastic collision takes place at the sample the corresponding energy can be found from the kinematic factor [J. R. Tesmer et al., 1995]:

$$k = \frac{E}{E_0} = \left( \frac{m_1}{m_1 + m_2} \right)^2 \left( \cos\theta \pm \sqrt{\left( \frac{m_2}{m_1} \right)^2 - \sin^2\theta} \right)^2 \quad (\text{Equation II-20})$$

Where  $\theta$  is the scattering angle,  $m_1$  is mass measured by the detector system and  $m_2$  is a mass of target element (see Figure II-25 ).

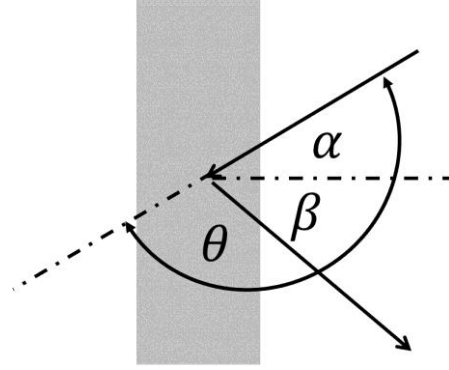


Figure II-25 Principle of RBS backscattering,  $\theta$  is the scattered angle and  $\alpha$  is the incident angle.

From the Equation, II-20 can be seen that particles backscattered from heavier elements will have a higher energy in the RBS spectra. To improve the mass resolution in RBS spectra  $[\sim(\partial K/\partial m_2)^{-1}]$  the higher scattering angles ( $\theta \sim \pi$ ) are used.

The probability of scattering or sensitivity used for quantification of elements is defined by the scattering cross-section for large angle scattering ( $\theta \sim \pi$ ) into differential solid angles  $d\Omega$  [R. Escobar Galindo et al., 2010]:

$$\frac{d(\theta)}{d\Omega} \xrightarrow{\theta \rightarrow \pi} \left( \frac{Z_1 Z_2 e^2}{4E} \right)^2 \frac{1}{\sin^4 \theta} \quad (\text{Equation II-21})$$

Where  $e$  is the electron charge,  $Z_1$  and  $Z_2$  are the atomic numbers of projectile and target elements. From this equation, it follows that sensitivity is increasing with atomic number  $Z$  and decreasing with backscattered energy  $E$ .

The depth resolution ( $\delta x$ ) of RBS spectra is inversely proportional to the energy loss of the ions  $S$  on their way through the material and is given [R. Escobar Galindo et al., 2010]:

$$\delta x = \frac{\delta E}{[S]} \quad (\text{Equation II-22})$$

The energy resolution is 15-20 keV and depth resolution of an RBS concentration profile can be as good as 5-10 nm. Basically, the depth resolution of the RBS profile depends not only on the energy resolution of the detector but also on other parameters, such as material and elements to be detected, the surface roughness of the sample, and quality of the interfaces etc. Similar to SIMS depth profiling, the depth resolution will degrade with increasing depth. It can be explained by straggling effects and the loss of beam monochromaticity [R. Escobar Galindo et al., 2010].

The basic components of the RBS technique are (i) ion beam source (alpha particles or protons), (ii) linear particle accelerator which accelerates the incident ions to high energies, (iii) detector which measures the energies of backscattered ions.

Techniques such as Particle Induced X-ray Emission (PIXE) and Particle Induced Gamma-Ray Emission (PIGE) are often used also for quantitative analysis to compensate weaknesses of RBS. The former technique provides better mass separation for heavy elements while the latter is implemented for analyzing the light elements such as aluminum. In PIXE, the principle is based on the ejection of an inner shell electron under high energy proton bombardment. The created vacancy will be filled by an outer-shell electron, which lowers its energy by emitting X-rays at an energy characteristic of the element involved. PIGE technique is similar to PIXE technique, except that the elemental information comes from the detection of  $\gamma$  rays.

### II.2.4.1 Experimental conditions

RBS experiments were performed at the CENBG (Centre d'Etudes Nucléaires de Bordeaux), Bordeaux, France. RBS analysis of III-V materials was carried out in a vacuum of  $2 \cdot 10^{-6}$  Torr. The source of  $^4\text{He}^+$  at an energy of 2.2 MeV (1.6 MeV for some samples) was delivered by the electrostatic accelerator type Singletron. The target incident current of 3 nA for a few  $\text{mm}^2$  scanning surface was used during experiments.

The incident particles were detected at an angle of  $160^\circ$ . Samples were tilted by  $4^\circ$  or  $15^\circ$  to overcome the channeling effect when the ion beam is aligned along a crystallographic direction of the target. In monocrystalline samples, the bombardment in random direction gives higher RBS signal than in channeling. Additionally, PIXE measurements were performed for series of samples (see Chapter III). Proton energy of 2.83 MeV was used. To confirm the results obtained using RBS and PIXE, the measurements using PIGE were performed. For PIGE experiments, proton energy of 2.83 MeV was used while the samples were inclined at  $45^\circ$  to the beam axis and the detection was carried out at  $90^\circ$ . To determine Al composition, the gamma-ray yield from the reaction  $^{27}\text{Al} (p,p'\gamma)^{27}\text{Al}$  was compared with the reference thin Al sample ( $\text{Al} = 163 \cdot 10^{15} \text{ at/cm}^2$ )

## REFERENCES:

- [A. Benninghoven, et al. 1987] Secondary Ion Mass Spectrometry: Basic Concepts, Instrumental Aspects, Applications and Trends, Wiley.
- [D. Blavette, et al. 1993] An atom probe for three-dimensional tomography, *Nature*, **363** (6428), pp. 432-435.
- [L. C. Bobb, et al. 1966] Oriented growth of semiconductors. III. Growth of gallium arsenide on germanium, *Journal of Applied Physics*, **37** (13), pp. 4687-4693.
- [D. Briggs, et al. 1990] Practical Surface Analysis: Auger and X-ray photoelectron spectroscopy, Wiley.
- [Cameca, 2014] The CAMECA IMS WF SC-Ultra ion source user's guide.
- [D. Childs, et al. 1995] Handbook of Auger Electron Spectroscopy, Physical Electronics.
- [R. Cipro, et al. 2014] Low defect InGaAs quantum well selectively grown by metal organic chemical vapor deposition on Si(100) 300 mm wafers for next generation non planar devices, *Applied Physics Letters*, **104** (26), pp. 262103.
- [E. De Hoffmann, et al. 2007] Mass Spectrometry: Principles and Applications, Wiley.
- [R. Escobar Galindo, et al. 2010] Towards nanometric resolution in multilayer depth profiling: a comparative study of RBS, SIMS, XPS and GDOES, *Analytical and Bioanalytical Chemistry*, **396** (8), pp. 2725-2740.
- [E. A. Fitzgerald, et al. 1991] Epitaxial necking in GaAs grown on pre-patterned si substrates, *Journal of Electronic Materials*, **20** (10), pp. 839-853.
- [Gault B, et al. 2012] Atom Probe Microscopy, Springer-Verlag.
- [P. Hoppe, 2006] NanoSIMS: A new tool in cosmochemistry, *Applied Surface Science*, **252** (19), pp. 7102-7106.
- [W. Hourani, et al. 2015] Nanoscale elemental quantification in heterostructured SiGe nanowires, *Nanoscale*, **7** (18), pp. 8544-8553.
- [H. Kroemer 1987] Polar-on-nonpolar epitaxy, *Journal of Crystal Growth*, **81** (1-4), pp. 193-204.
- [T. A. Langdo, et al. 2000] High-quality Ge on Si by epitaxial necking, *Applied Physics Letters*, **76** (25), pp. 3700-3702.
- [Q. Li, et al. 2015] Growing antiphase-domain-free GaAs thin films out of highly ordered planar nanowire arrays on exact (001) silicon, *Applied Physics Letters*, **106** (7), pp. 072105.
- [A. Merkulov, 2013] The secondary ions emission from Si under low-energy Cs bombardment in a presence of oxygen, *Surface and Interface Analysis*, **45** (1), pp. 90-92.
- [N. S. Smith, et al. 2007] A High Brightness Source for Nano-Probe Secondary Ion Mass Spectrometry.
- [P. M. Petroff ,1986] Nucleation and growth of GaAs on Ge and the structure of antiphase boundaries, *Journal of Vacuum Science & Technology B*, **4** (4), pp. 874-887.
- [M. Razeghi, 1995] The MOCVD Challenge: Volume 2: A Survey of GaInAsP-GaAs for Photonic and Electronic Device Applications: Taylor & Francis.
- [S. Jiang et al., 2014] Growth rate for the selective epitaxial growth of III- compounds inside submicron shallow-trench-isolation trenches on Si(001) substrates by MOVPE: Modeling and experiments, *Journal of Crystal Growth* **391**, pp 59-63.

- [S. Rubin, et al. 1957] Chemical Analysis of Surfaces by Nuclear Methods, *Analytical Chemistry*, **29** (5), pp. 736-743.
- [G. Slodzian, 1983] Remarks on Some Factors Influencing the Charge State of Sputtered Particles, *Physica Scripta*, pp. 54.
- [J. R. Tesmer, et al. 1995] Handbook of modern ion beam materials analysis: Materials Research Society.
- [J. J. Thomson, 1910] Rays of positive electricity, *Philosophical Magazine Series 6*, **20** (118), pp. 752-767.
- [M. Usman, et al. 2012] Nanostructuring of silicon substrates for the site-controlled growth of GaAs/In<sub>0.15</sub>Ga<sub>0.85</sub>As/GaAs nanostructures, *Microelectronic Engineering*, **97**, pp. 59-63.
- [P. Van Der Heide, 2014] Secondary Ion Mass Spectrometry: John Wiley & Sons, Inc.) pp 145-194.
- [W. Vandervorst, 2008] Semiconductor profiling with sub-nm resolution: Challenges and solutions, *Applied Surface Science*, **255** (4), pp. 805-812.
- [J. C. Vickerman, et al. 2013] ToF-SIMS: Materials Analysis by Mass Spectrometry: IM Publications.
- [R. G. Wilson, et al. 1989] Secondary ion mass spectrometry: a practical handbook for depth profiling and bulk impurity analysis, Wiley.
- [J. Zilko 2012] Handbook of Thin Film Deposition, Elsevier, pp 151-204.

## CHAPTER III

### III. Quantitative chemical analysis of III-V elements using SIMS

This chapter deals with the chemical compositional analysis for InGaAs channel materials and doping profiling for the future generation of transistors. An accurate quantitative analysis for III-V materials in 3D architecture is challenging. Firstly, the theoretical background for quantitative SIMS analysis and description of reference samples are given in detail in sections III.1 and III.2. Additionally, SIMS protocols and quantification of InGaAs/AlAs QW are described in section III.3. Finally, the SIMS and ToF-SIMS protocols for doping metrology for GaAs semiconductors in 2D and 3D architectures are discussed in the last section.

#### III.1 Theoretical aspects of quantitative SIMS analysis

SIMS quantitative analysis is based on the conversion of measured secondary ion intensity (counts per second) of an element in a matrix into its concentration (atoms per cm<sup>3</sup>). The secondary ion emission is a complex phenomenon, which depends on the surface chemistry during sputtering (primary ion implantation, damage, and segregation) and matrix effects. Thus, quantitative analysis is challenging.

The empirical (calibration) and semi-theoretical methods are proposed for SIMS quantitative analysis. The semi-theoretical method is based on the physical explanations of the ion emission model. More than fifteen different models have been proposed to explain the secondary ion emission, such as band structure model, the kinetic, the local thermal equilibrium (LTE), the work function, the molecular, electron tunneling models etc. These models are based on the explanation of the influence of the ionization energy on the ion yield considering such parameters as the work function (energy required to extract an electron from a solid), ionization potential, electron affinity and the emission velocity (in the electron tunneling model). However, there is no complete model developed to explain the secondary ion emission and which can be successfully applied to quantify SIMS data. [P. van der Heide, 2014].

Fundamentally, the secondary ion signal is proportional to the primary ion current  $I_p$ , sputter yield  $Y$  and instrumental transmission including detection efficiency  $f$  (e.g. more than 70% for dynamic SIMS), instrumental transmission factor, and the fractional concentration of element A in the surface layer  $C_A$ :

$$I_A = I_p \cdot Y \cdot \beta_A \cdot f \cdot C_A \quad (\text{Equation III-1})$$

The empirical method is based on a calibration curve generated by measurements of series of matrix-matched samples. Basically, the empirical method is often used for SIMS quantification.

Figure III-1 shows a calibration curve  $I=f(C)$  for element A using the reference sample with known concentration  $C_A$ . The slope of this curve  $\frac{dI}{dC} = \rho$  is called sensitivity factor and depends on the concentration. The linear dependence is preferable whereas the non-linear variation often occurs in alloy semiconductor materials. To find the concentration in an unknown sample X, the analytical function of  $C_A = f^{-1}(I_A/I_R)$  is used.

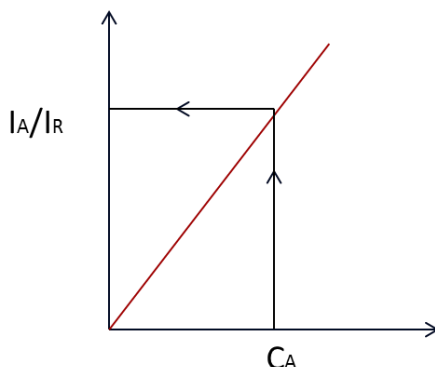


Figure III-1 Calibration curve  $I=f(C)$ , where  $I_R$  and  $C_R$  are the intensity and concentration of reference sample A.

The ratio of intensities of the reference element and the element of interest A can be expressed using the previous equation to give the value of the relative sensitive factor (RSF) used for calibration:

$$RSF = C_A \cdot \frac{I_R}{I_A} \cdot \frac{k_R}{k_A} \quad (\text{Equation III-2})$$

Where  $k_R$  and  $k_A$  are the isotope abundances,  $I_R$  and  $C_R$  are secondary ion intensity and concentration of the reference element, respectively.

The RSF value expressed through the concentration of elemental concentration can be calculated by:

$$C_A = RSF \cdot \frac{I_A}{I_R} \cdot \frac{k_A}{k_R} \quad (\text{Equation III-3})$$

Ion implanted reference samples are often used for determination of low dose composition in a matrix. However, the calibration curve is not necessary to be estimated, the direct RSF value estimated from one reference sample can be applied. RSF value for ion-implanted standards with known dose  $\phi$  of impurity can be calculated with the help of the next equation:

$$RSF = \frac{\phi}{\int_{d2}^{d1} \left( \frac{I_A}{I_R} \right)} \quad (\text{Equation III-4})$$

As was mentioned before, the ion yields of secondary ions can change over several orders of magnitude depending on the element and on the surface composition of the materials [A. Benninghoven et al., 1987]. The ion yield can be enhanced by choosing the sputtering ion beam (cesium or oxygen) depending on the polarity (electropositive or electronegative) elements. [R.G. Wilson et al., 1989, C. A. Andersen et al., 1972].

RSF for various semiconductor materials (e.g. GaAs, InP, Si) was studied over a period of a decade [R.G. Wilson et al., 1989, R. G. Wilson, 1995, H. Yamamoto et al., 2013, Y. Homma et al., 1992]. RSF time-dependence was reported using the old series of SIMS instruments (CAMECA 3f, 4f, and 5f) [Y. Homma et al., 1991]. The low accuracy of  $\pm 50\%$  can be obtained depending on the material as a result of the difference between the instruments. The instrument modifications include such differences as a mass analyzer and the incident angle of primary ions, the detection efficiency of the detector etc. Basically, the high precision of quantitative analysis (less than 5%) can be obtained using matrix-matched reference samples and controlled analysis conditions (vacuum, instrumental presets).

One of the most effective techniques to quantify the SIMS analysis was proposed by M. Gauneau in 1984. In his work, he proposed to detect  $\text{MCs}^+$  molecular ions rather than  $\text{M}^{\pm}$  ions, where M is the element of interest under  $\text{Cs}^+$  bombardment. The formation  $\text{MCs}^+$  ion is based on the recombination of a neutral  $\text{M}^0$  atom with a  $\text{Cs}^+$  ion and is given by.



The binding energy between M and Cs and atomic polarizability of M play an important role in the formation of  $\text{MCs}^+$  molecular ions.  $\text{MCs}_2^+$  molecular ions can be used for electronegative elements M, which give higher yield compared to  $\text{MCs}^+$  ions. The formation process can be expressed for electropositive and electronegative elements M through the following formulas:



The intensity of  $\text{MCs}^+$  clusters can be found using the next equation [T.Wirtz et al., 2001]:

$$I(\text{MCs}^+) = I_p \cdot Y^2 \cdot C_M \cdot C_{\text{Cs}} \cdot \beta_{\text{Cs}}^+ \cdot \gamma_{\text{M}^0-\text{Cs}^+} \cdot f \quad (\text{Equation III-9})$$

Where  $I_p$  is the primary current, Y is the sputtering yield,  $C_M$  is the surface concentration of the element M,  $C_{\text{Cs}}$  is the Cs surface concentration,  $\beta_{\text{Cs}}^+$  is the ionization probability of a sputtered Cs atoms,  $\gamma_{\text{M}^0-\text{Cs}^+}$  is a factor, which represents the recombination probability between  $\text{M}^0$  and  $\text{Cs}^+$  and f is the instrumental transmission factor (detection efficiency of the  $\text{MCs}^+$  cluster).

The ionization probability is given by [Y. Kudriavtsev et al., 2013]

$$\beta_{Cs}^+ \propto \exp \left[ -\frac{I_p(CsM) - \Phi^*}{\varepsilon_p} \right] \quad (\text{Equation III-10})$$

Where  $I_p(CsM)$  is the ionization potential of a CsM cluster,  $\Phi^*$  the work function of the targets surfaces exposed to cesium ions,  $\varepsilon_p$  is a factor characterizing the ion sputtering conditions.

The work function for semiconductor materials under cesium bombardment described as ionization potential with band gap shift due to cesium ion implantation [Y. Kudriavtsev et al., 2013]:

$$\Phi^* = A + E_g - \Delta\Phi \quad (\text{Equation III-11})$$

Where  $E_g$  is the band gap and  $A$  is the electron affinity of the semiconductors. For GaAs a work function shift  $\Delta\Phi$  is found of 0.58 eV [Y. Kudriavtsev et al., 2013]. For GaAs compared to Si has higher ionization potential  $\Phi_{GaAs}^* = 4.96\text{eV}$  and for  $\Phi_{Si}^* = 3.64\text{eV}$ . [Y. Kudriavtsev et al., 2013].

The  $MCs^+$  and  $MCs_2^+$  yields strongly depend on the stationary cesium surface concentration incorporated in the specimen during cesium sputtering. The increasing of the Cs surface concentration may lead to a lowering of the electron work function below a critical value, which is located slightly below the ionization energy of Cs. Thus, the probability of formation of  $MCs^+$  and  $MCs_2^+$  decreases according to the electron tunneling model [T. Wirtz et al., 2001]. The  $MCs^+$  technique is often used for quantification of semiconductor alloys as the matrix effects are reduced. The disadvantages of using the  $MCs^+$  and  $MCs_2^+$  are poor sensitivity and detection limits. Thus, this method is rarely used for depth profiling of low-dose dopant profiles by SIMS.

## III.2 Description of reference standards for accurate measurements of composition in $In_xGa_{1-x}As$ and $Al_xGa_{1-x}As$ matrices

### III.2.1 Ion-implanted standards

The quantification of impurities and dopants in semiconductor materials is an important analysis for doping, contamination and diffusion studies for semiconductor materials. Ion implantation is often used to create the reference standards for SIMS quantitative analysis of low-dose elements. A dose measurement with less than 1% reproducibility has been reported using magnetic sector, quadrupole, and ToF-SIMS techniques [R. G. Wilson, 1995, F. A. Stevie et al., 2008].

The ion dose represents the number of ions implanted into the sample and is given in units of  $\text{cm}^{-2}$ . The depth (range) distribution of the implanted ions is approximately Gaussian in shape

and is characterized by a projected range  $R_p$  and a straggling  $\Delta R_p$ . The projection range depends on ion mass  $M_1$ , incident energy  $E$  and relative width ratio  $\Delta R_p/R_p$ , on the ratio between ion mass and the mass of the substrate ion  $M_2$  [J. W. M. M. Nastasi, 2006]. The concentration of the implant depends on the ion dose  $\phi$  or fluence, which is controlled by the measured ion current. More information on the ion implantation process can be found in reference [J. W. M. M. Nastasi, 2006].

For this work, ion-implanted reference samples with low concentration of impurities in a GaAs matrix were designed. The projection range  $R_p$  of 100 nm and 200 nm for high (Al, In, Si) and low mass (C, H, O) ions with dose of  $\phi=5 \cdot 10^{14}$  atoms/cm<sup>2</sup> were respectively defined. To avoid the possible mass interferences, the major isotopes of ions were implanted separately (except C, H, O reference sample). The energy of implantation  $E$  for target  $R_p$  was calculated by Monte Carlo simulation using TRIM software [J. F. Ziegler]. The description of ion-implanted samples is presented in Table III-1.

**Table III-1.** Description of ion-implanted reference samples

Target ion	Matrix	$\phi$ , atoms/cm <sup>2</sup>	$R_p$ , nm	$E$ , keV
28Si	GaAs	$5 \cdot 10^{14}$	100	125
27Al	GaAs	$5 \cdot 10^{14}$	100	95
115 In	GaAs	$5 \cdot 10^{14}$	100	380
$^{18}O^1$ , $^{12}C^2$ , $^1H^3$	GaAs	$5 \cdot 10^{14}$	200	$^{133}1$ ; $^{105}2$ ; $^{27,5}3$

The Monte Carlo simulation and SIMS experimental data for indium in gallium arsenide are shown in Figure III-2.

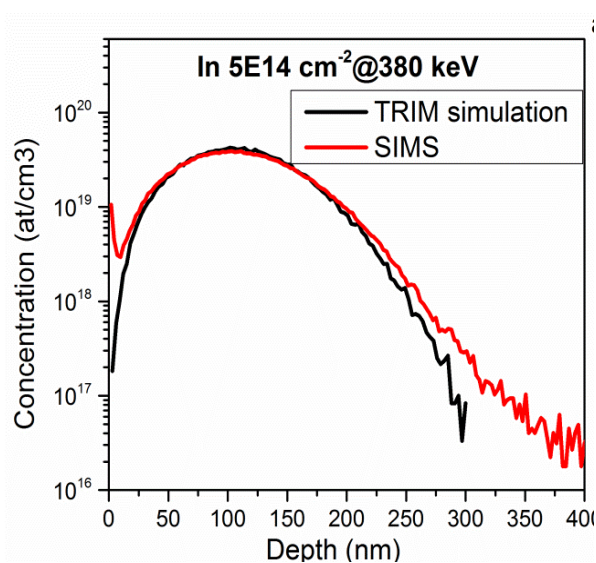


Figure III-2 Depth profiles of ion-implanted samples a) In in GaAs b) Al in GaAs using Monte Carlo simulation and SIMS measurements.

### III.2.2 Standards for accurate measurements of $x$ in $\text{In}_x\text{Ga}_{1-x}\text{As}$ matrix

Samples were designed as reference samples for indium quantification in InGaAs and additionally Al in  $\text{Al}_x\text{Ga}_{1-x}\text{As}$  samples. All reference samples were grown on planar Si wafers by MOCVD. These materials were described in section II.1.4. The values of  $x=0.1$ ,  $x=0.28$ ,  $x=0.4$  in the  $\text{In}_x\text{Ga}_{1-x}\text{As}$  matrix were defined as nominal values during the growth. The additional samples such as GaAs/Si and GaAs/Ge/Si were designed to determine Ga and As composition in GaAs layers.

The series of samples were measured using the RBS technique using a  $^4\text{He}^+$  ion beam at an energy of 2.2 MeV. Sample tilting was used to avoid the channeling effect in which the ion beam is aligned with a crystalline axis. Detail information about RBS experimental conditions can be found in section II.2.4. The simulation for each RBS spectra was performed using SIMNRA software[www.simnra.com]. The RBS spectra for GaAs/Ge/Si and GaAs/Si samples are presented in Figure III-3. It can be seen that the Ga and As peaks are not separated. In Figure III-4 the peak for In element (a, b, c) and for (d) Al can be observed, whereas peaks for Ga, Ge and As elements are not separated as well, thus cannot be quantified.

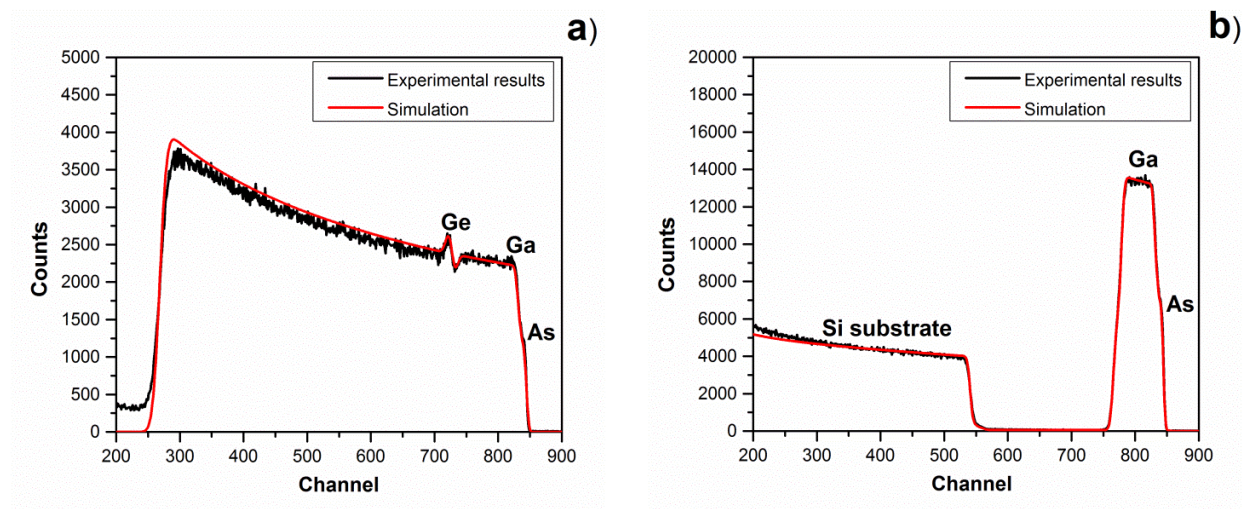


Figure III-3 RBS spectra of a) GaAs/Ge/Si (Ref. GaAs) and b) GaAs/Si (Ref. GaAs) reference samples using a  $^4\text{He}^+$  beam at 2.2 MeV, incident angle at  $\alpha=15^\circ$  with respect to the normal to the target surface and a detection angle of  $\theta=160^\circ$ .

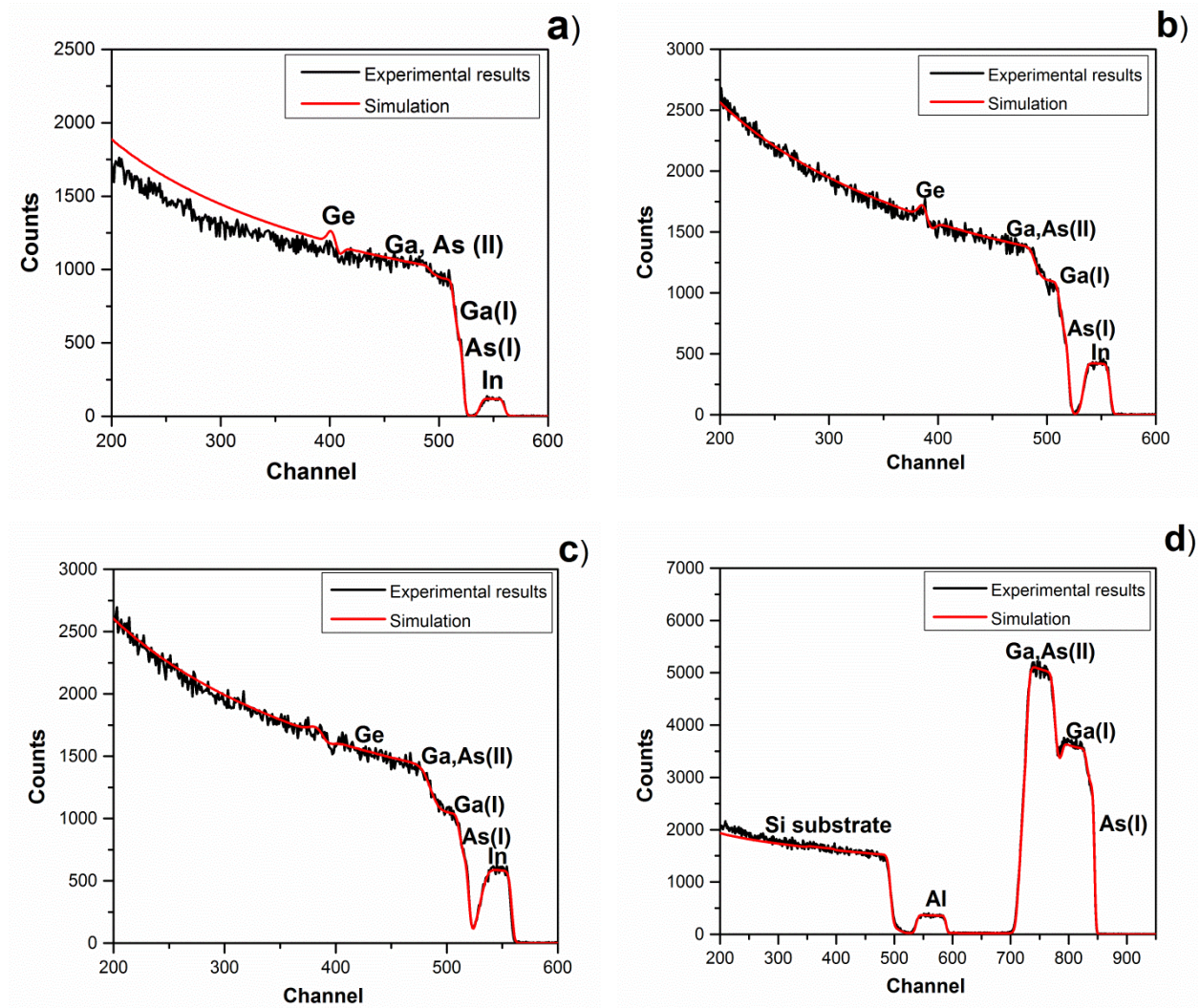


Figure III-4 RBS spectra a) b) c) of series InGaAs/GaAs/Ge/Si (IGA #1, 2, 3) samples and d) AlGaAs/GaAs/Si (AlGa #1) sample using  $^4\text{He}^+$  ion source at energy of 1.6 MeV, sample angle  $\alpha=4-5^\circ$  and backscattering angle  $\theta=160^\circ$ .

To quantify the Ga and As elements coming from each layer, PIXE measurements using protons energy of 2.83 MeV were performed. The PIXE results for GaAs/Ge/Si and InGaAs/GaAs/Ge/Si samples are presented in Figure III-5 a. Additionally, the measurements were performed for AlGaAs/GaAs/Si and GaAs/Si samples and are given in Figure III-5 b.

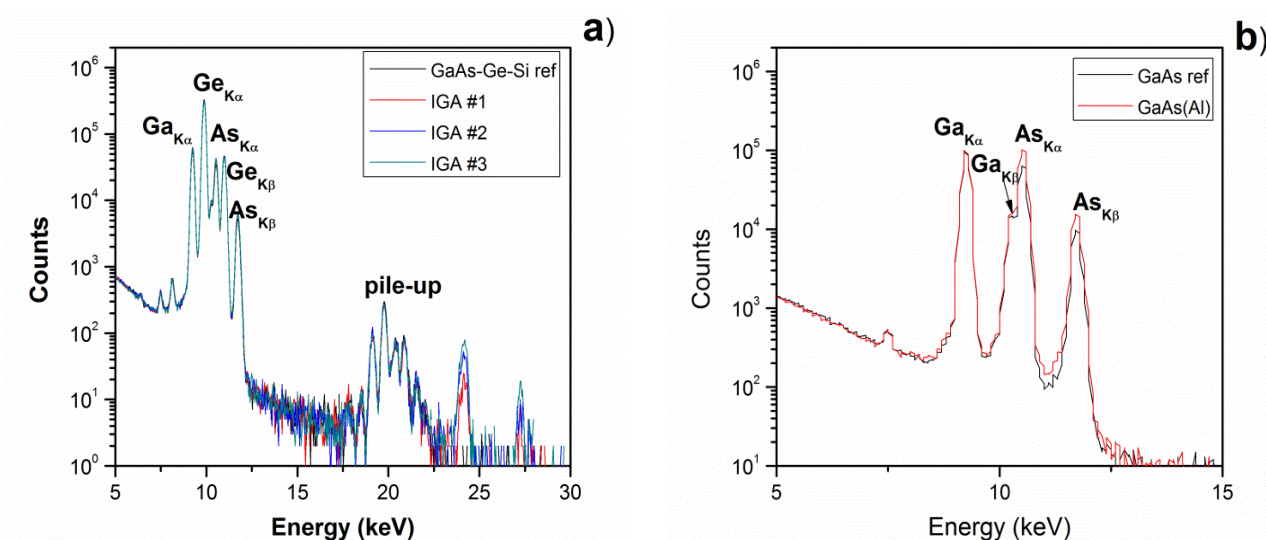


Figure III-5 PIXE spectra for a) series InGaAs/GaAs and reference GaAs/Ge/Si samples and b) AlGaAs/GaAs/Si and GaAs/Si samples using protons  $^1\text{H}^+$  at an energy of 2.83 MeV, sample angle  $\alpha=0^\circ$  and backscattering angle  $\theta=135^\circ$ .

Furthermore, PIGE measurements were performed to estimate Al composition in the AlGaAs/GaAs/Si sample and to confirm PIXE results. The PIGE spectrum is given in Figure III-6. The chemical composition data of the series of measurements are summarized in Table III-2 and Table III-3. The presence of oxygen was assumed for AlGaAs/GaAs/Si sample during the simulations.

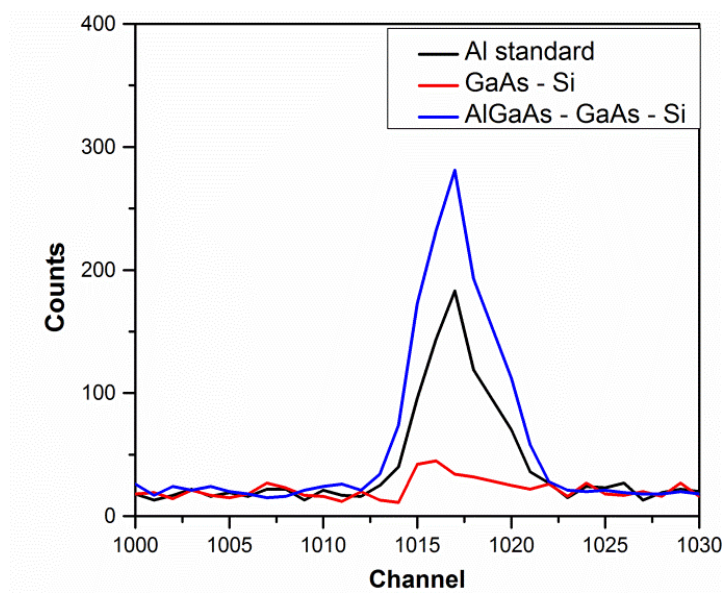


Figure III-6 PIGE spectra of AlGaAs/GaAs/Si and GaAs/Si samples using protons  $^1\text{H}^+$  at an energy of 2.83 MeV.

**Table III-2.** Chemical composition of  $\text{In}_x\text{Ga}_{1-x}\text{As}$  standards using RBS and PIXE techniques

Name of standards	Structure of materials	Ga ( $\pm 15$ ), $10^{15}$ at/cm <sup>2</sup>	As ( $\pm 20$ ), $10^{15}$ at/cm <sup>2</sup>	In ( $\pm 10$ ), $10^{15}$ at/cm <sup>2</sup>	Total $10^{15}$ at/cm <sup>2</sup>	Ga/As
IGA #1	$\text{In}_x\text{Ga}_{1-x}\text{As}$ :100 nm / GaAs:400 nm/Ge:1.6 $\mu\text{m}$ /Si	170.3	190.0	19.8	380	0.89
IGA #2	$\text{In}_x\text{Ga}_{1-x}\text{As}$ :100 nm /GaAs/ Ge: 1.6 $\mu\text{m}$ /Si	136.8	190.0	53.2	380	0.72
IGA #3	$\text{In}_x\text{Ga}_{1-x}\text{As}$ :100 nm / GaAs:400 nm/Ge:1.6 $\mu\text{m}$ /Si	135.0	225.0	90.0	450	0.60
Ref .GaAs	GaAs:400 nm /Ge:1.6 $\mu\text{m}$ /Si	873.3	876.7	-	1750	1

**Table III-3** Chemical composition of  $\text{Al}_x\text{Ga}_{1-x}\text{As}$  standards using RBS and PIXE techniques

Name of standards	Structure of materials	Ga ( $\pm 10$ ) $10^{15}$ at/cm <sup>2</sup>	As ( $\pm 10$ ) $10^{15}$ at/cm <sup>2</sup>	Al ( $\pm 20$ ) $10^{15}$ at/cm <sup>2</sup>	O ( $\pm 10$ ) $10^{15}$ at/cm <sup>2</sup>	Total $10^{15}$ at/cm <sup>2</sup>	Ga/As
AlGa #1	AlGaAs:240nm/ GaAs:230nm/Si	148.4	503.5	360.4	47.7	1060	0.29
Ref. GaAs	GaAs:230 nm/Si	529.7	520.3	-	-	1050	1.02

Additional series of InGaAs/GaAs/Si samples were measured by X-ray diffraction (XRD) and ellipsometry techniques. The results of measurements are summarized in

Table III-4. The concentrations in atoms/cm<sup>3</sup> for XRD and PL measurements were found using Vegard's law [A. R. Denton et al., 1991]. To calculate the density, the lattice parameter for  $\text{In}_x\text{Ga}_{1-x}\text{As}$  was found through the following equation:

$$a_{\text{In}_x\text{Ga}_{1-x}\text{As}} = x \cdot a_{\text{InAs}} + (1 - x) \cdot a_{\text{GaAs}} \quad (\text{Equation III-12})$$

Where  $a_{\text{InAs}}$  and  $a_{\text{GaAs}}$  are lattice parameters for InAs and GaAs layers ( $a_{\text{InAs}}$ =6.05 Å and  $a_{\text{GaAs}}$ =5.65 Å). The indium concentration (atoms/cm<sup>3</sup>) is found through the calculated density  $\rho$  and fraction  $x$  using the following formula:

$$C_A = \rho \cdot [x] \quad (\text{Equation III-13})$$

**Table III-4** Description of the series of additional  $\text{In}_x\text{Ga}_{1-x}\text{As}$  reference samples measured using XRD technique

Name of standards	Structure of materials	fraction x	Method of measurement
IGA #1	$\text{In}_x\text{Ga}_{1-x}\text{As}$ : 100 nm /GaAs: 400 nm/Ge:1,6 $\mu\text{m}$ /Si	$0.1 \pm 0.01$	RBS, PIXE
IGA #2	$\text{In}_x\text{Ga}_{1-x}\text{As}$ : 100 nm /GaAs: 400 nm/Ge: 1,6 $\mu\text{m}$ /Si	$0.28 \pm 0.014$	RBS, PIXE
IGA #3	$\text{In}_x\text{Ga}_{1-x}\text{As}$ : 100 nm /GaAs: 400 nm/Ge: 1,6 $\mu\text{m}$ /Si	$0.4 \pm 0.01$	RBS, PIXE
IGA #4	$\text{In}_x\text{Ga}_{1-x}\text{As}$ : 158 nm/GaAs: 200 nm/Si	$0.52 \pm 0.01$	XRD
IGA #5	$\text{In}_x\text{Ga}_{1-x}\text{As}$ : 98 nm/GaAs: 200 nm /Si	$0.29 \pm 0.01$	XRD
IGA #6	$\text{In}_x\text{Ga}_{1-x}\text{As}$ : 76 nm/GaAs: 200 nm /Si	$0.062 \pm 0.01$	XRD
IGA #7	$\text{In}_x\text{Ga}_{1-x}\text{As}$ : 143 nm/GaAs: 200 nm/Si	$0.45 \pm 0.01$	XRD
IGA #8	$\text{In}_x\text{Ga}_{1-x}\text{As}$ : 83 nm /GaAs: 200nm/Si	$0.175 \pm 0.01$	XRD
IGA #9	$\text{In}_x\text{Ga}_{1-x}\text{As}$ : 113 nm/ GaAs: 200nm/Si	$0.36 \pm 0.01$	XRD
IGA #10	$\text{In}_x\text{Ga}_{1-x}\text{As}$ : 76nm /GaAs: 200nm/Si	$0.13 \pm 0.01$	XRD
IGA#11	$\text{In}_x\text{Ga}_{1-x}\text{As}$ : 190 nm /InP	$0.57 \pm 0.02$	Ellipsometry

### III.3 Development of a SIMS protocol for InGaAs channel material

#### III.3.1 Quantitative analysis of InGaAs QW using $\text{O}_2^+$ ion beam bombardment

To study the III-group elements with high sensitivity and achieve lower detection limits the experiments were carried out using oxygen sputtering with the Cameca SIMS SC-Ultra. The primary ion energy  $E_p$  between 5000 eV and 250 eV was used. More information can be found in Chapter II.2.1. The spectrometer presets were optimized to provide the detection of secondary ions on the same detector (EM). A typical SIMS depth profile for InGaAs under oxygen sputtering is presented in Figure III-7. No enhancement of ion yield using oxygen flooding contrary to what happens with Si was observed, thus, the oxygen flooding was not used.

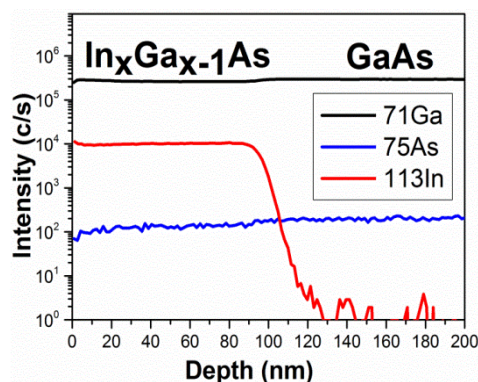


Figure III-7 SIMS depth profile of  $\text{In}_{0.05}\text{Ga}_{0.95}\text{As}/\text{GaAs}$  under 500 eV  $\text{O}_2^+$  ion beam bombardment.

To calculate the unified sputter rate for InGaAs series samples at a given primary current  $I_p$  and raster of ion beam  $R$  the next relation was used:

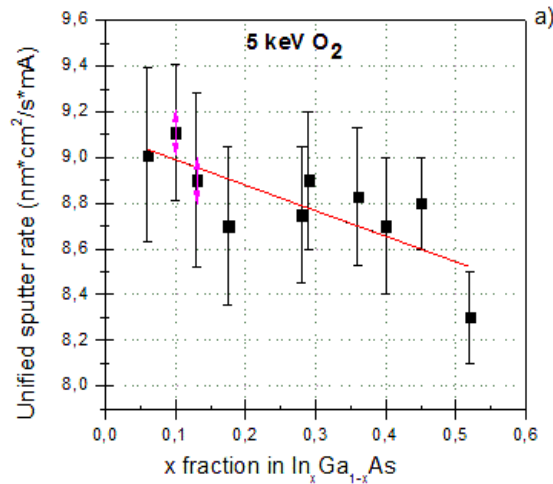
$$U_{SR} = \frac{SR \left[ \frac{nm}{s} \right] \cdot R^2 [cm^2]}{I_p [mA]} \quad (\text{Equation III-14})$$

The unified sputter rate is plotted as a function of  $x$  in  $In_xGa_{1-x}As$  series samples under high and low energy oxygen bombardment and is shown in Figure III-8. The uncertainty of unified sputter rate is through the next relation:

$$\Delta U_{SR} = |U_{SR}| \cdot \sqrt{\left( \frac{\delta d}{d} \right)^2 + \left( \frac{\delta I_p}{I_p} \right)^2 + 4 \cdot \left( \frac{\delta R}{R} \right)^2} \quad (\text{Equation III-15})$$

Where  $\delta d$  is the standard deviation of layer thickness;  $\delta I_p$  is a standard deviation of measured primary current, and  $\delta R$  is a standard deviation of sputtered area.

The decrease of sputter rate with increasing  $x$  fraction in  $In_xGa_{1-x}As$  is observed for 5 keV oxygen bombardment, whereas at a primary energy less than 1 keV the sputter rate variation with composition is minor. In general, the sputter rate decreases with decreasing primary energy.



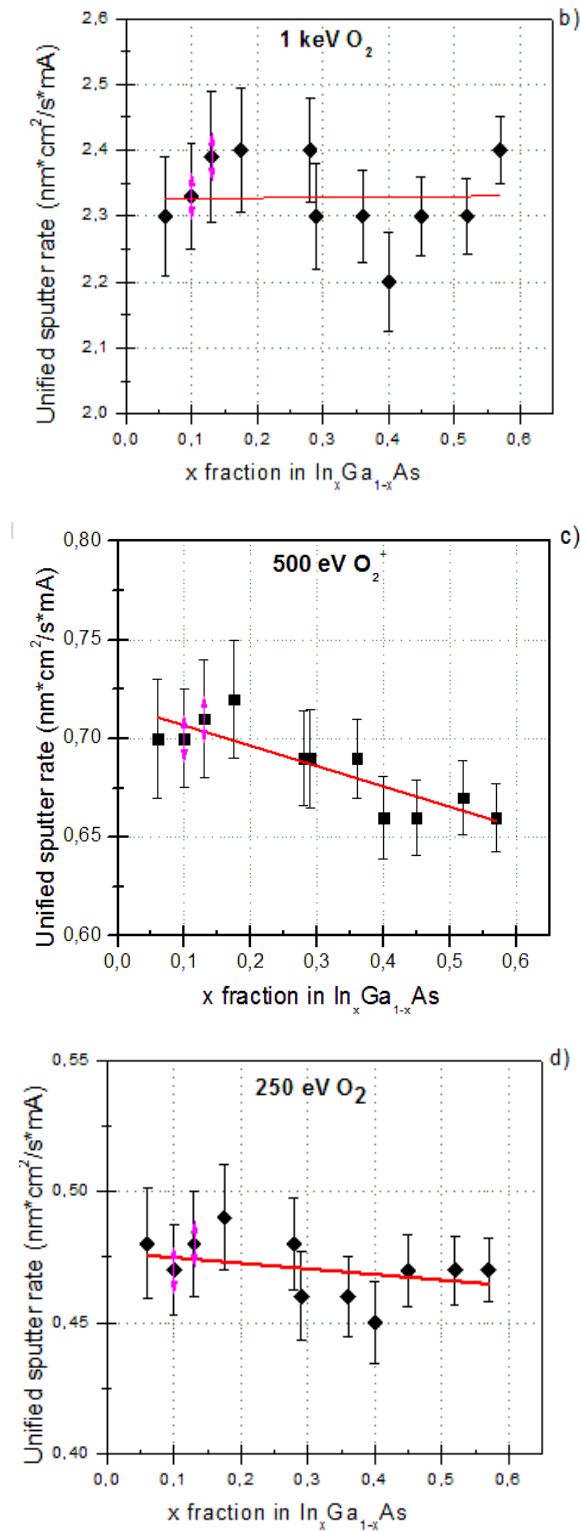


Figure III-8 Unified sputter rate as a function of x function in the  $\text{In}_x\text{Ga}_{1-x}\text{As}$  matrix under oxygen bombardment with the energy of a) 5 keV, b) 1 keV, c) 500 eV and d) 250 eV.

To estimate sputter yield  $Y$  as the ratio of sputtered atoms per target primary ion at given primary energy and incident angle the following formula was used [M. J. P. Hopstaken et al., 2010]:

$$USY = \frac{SR \left[ \frac{\text{nm}}{\text{s}} \right] \cdot R^2 [\text{cm}^2] \cdot \rho \left[ \frac{\text{atoms}}{\text{cm}^3} \right]}{I_p [\text{ions}] \cdot \cos(\theta)} \quad (\text{Equation III-16})$$

Where  $\theta$  is the incident angle, and  $\rho$  is the density of the material ( $\text{atoms}/\text{cm}^3$ ). The primary current  $I_p$  can be presented through the number of ions pulsed per second. Assuming that one ion is equal to  $1.602 \cdot 10^{-19}$  Coulomb, and 1 nA can be expressed as  $6.24 \cdot 10^9$  ions/s.

The sputter yield as a function of primary energy for InGaAs (at density value  $\rho = 4.3 \cdot 10^{22}$   $\text{at}/\text{cm}^3$ ) is presented in Figure III-9. It can be seen that at higher energies the sputter yield is higher.

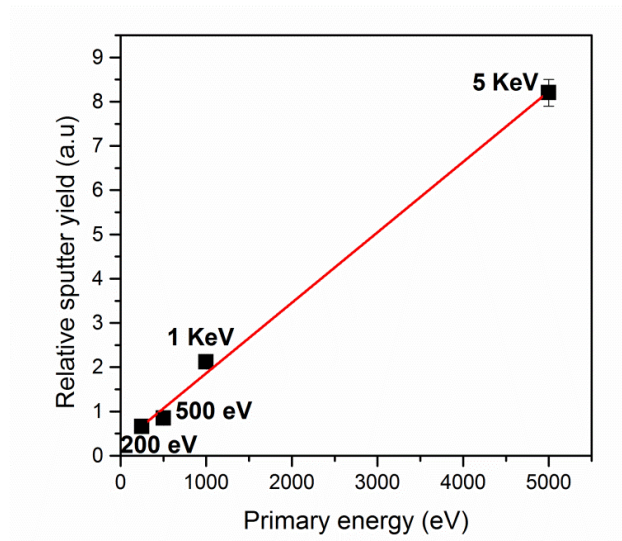


Figure III-9 Sputter yield of  $\text{In}_{0.1}\text{Ga}_{0.9}\text{As}$  as a function of the primary energy of oxygen beam.

The surface oxygen concentration  $[\text{O}]$  of implanted primary species at the sample surface can be described by the following relation [T.Wirtz et al., 2001]:

$$[\text{O}] \propto \frac{1}{1 + Y} \quad (\text{Equation III-17})$$

Low energy ion beam bombardment leads to a significant decrease of sputter yield and therefore, increasing O-concentration (or “O-retention”). This tendency is similar to what happens in Ge material [C. Huyghebaert et al., 2004], in which the oxygen incorporation remains very low at high sputtering energy and at low energy full oxidation can occur.

To understand the oxygen concentration implanted in the sample surface at different energies considering the incident angle the Equation III-16 and Equation III-17 can be combined to give the following equation:

$$[O] \propto \frac{\cos(\theta)}{\cos(\theta) + Y} \quad (\text{Equation III-18})$$

Following the equation Equation III-18 to reduce the oxygen incorporation at low bombardment energy can be reduced with increasing the incident angle ( $\theta > 40^\circ$ ), and thus, such analysis conditions will be preferable for quantitative analysis and depth profiling using magnetic SIMS.

The secondary ion intensity ratio In/Ga as a function of composition  $x/(1-x)$  in InGaAs under the different energy of oxygen sputtering energies is presented in Figure III-10. The Figure shows the linear ion intensity ratio dependence on an x fraction ( $x > 0.1$ ) is observed for high and low energy oxygen sputtering. Ga ion intensity is higher compared to In ion intensity at all sputter energies. It can be observed also that decreasing the energy of the primary ion beam leads to an increase of In/Ga ion intensity ratio. For  $x > 0.1$  the In/Ga ion intensity ratio gives a slope of 0.2 at 5 and 1 keV while 0.24 and 0.34 values at 500 and 250 eV oxygen sputtering.

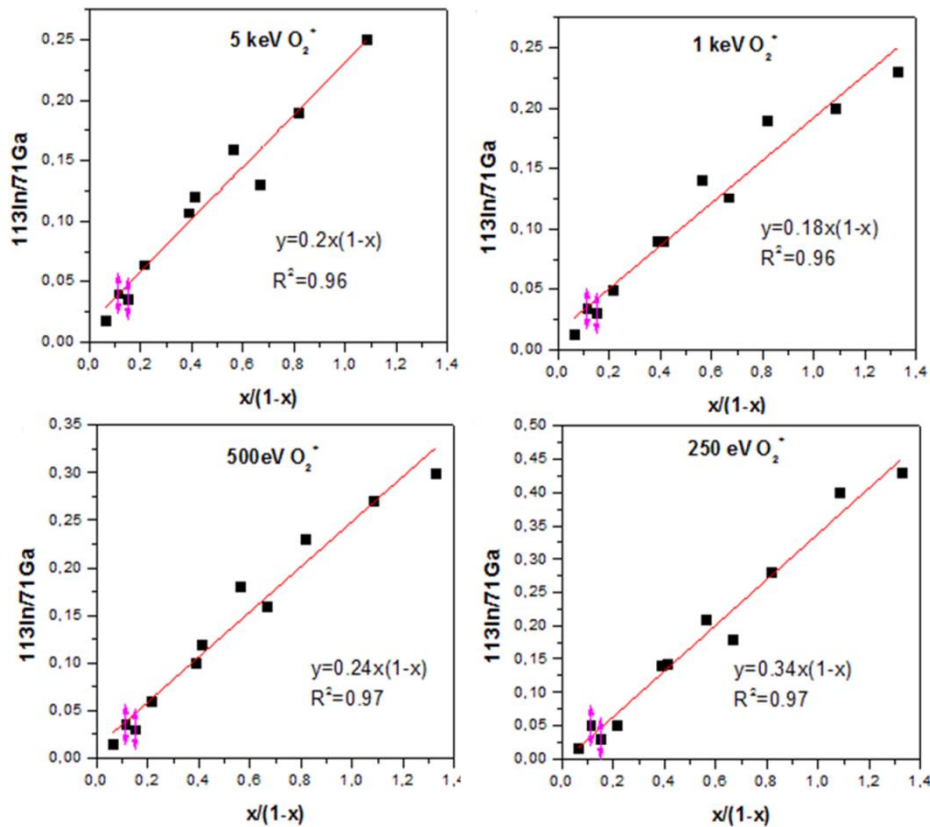


Figure III-10 Ion intensity ratio  $^{113}\text{In}/^{71}\text{Ga}$  as a function of In fraction  $x$  in  $\text{In}_x\text{Ga}_{1-x}\text{As}$  under different oxygen sputtering energies a) 5 keV ( $40^\circ$ ), b) 1 keV ( $39^\circ$ ), c) 500 eV ( $42^\circ$ ) and d) 250 eV ( $49^\circ$ ).

To study the ion yield as the number of detected ions  $I_A$  per the number of sputtered atoms the useful ion yield  $\tau_A$  is considered [R. G. Wilson et al., 1989]:

$$\tau_A = \frac{\frac{1}{n} \sum_{i=1}^n I_A [c/s]}{C_A[at/cm^3] \cdot R^2[cm^2] \cdot SR[cm/s]} \quad (\text{Equation III-19})$$

The useful ion yield for In and Ga as a function of composition  $0.1 < x < 0.4$  for different primary impact energies is given in Figure III-11. The In and Ga ion yields increase with decreasing primary impact energy of the oxygen beam. For indium fraction  $0.1 < x < 0.4$  the ion yield depends on the composition  $x$  in  $\text{In}_x\text{Ga}_{1-x}\text{As}$ . Indium ion yield decreases with increasing fraction  $x$  in  $\text{InGaAs}$  whereas the Ga ion yield is less dependent on Ga composition in  $\text{In}_x\text{Ga}_{1-x}\text{As}$ .

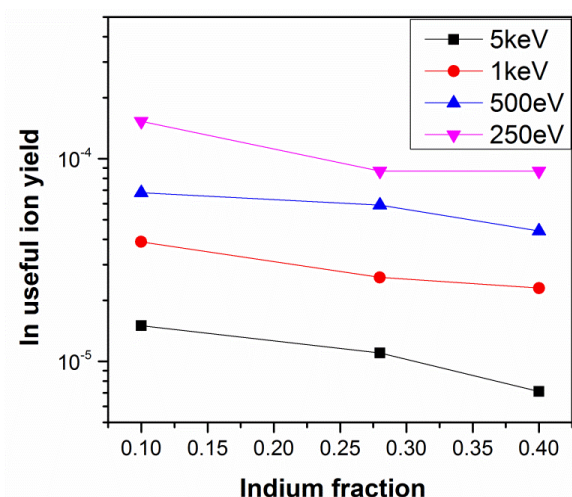


Figure III-11 Indium ion yield as a function of In fraction  $0.1 < x < 0.4$  in  $\text{In}_x\text{Ga}_{1-x}\text{As}$  under oxygen beam sputtering.

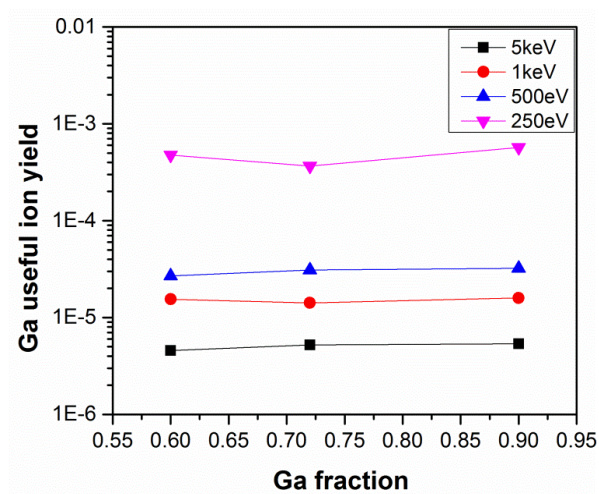


Figure III-12 Gallium useful ion yield as a function of Ga  $[1-x]$  fraction in  $\text{In}_x\text{Ga}_{1-x}\text{As}$  under oxygen beam sputtering.

The incident angle should be considered to understand the In and Ga ion yield. Note that with decreasing impact energy the incident angle increases. At high energy (5 keV) the incident angle corresponds to  $40^\circ$  whereas at 250 eV the incident angle is  $49^\circ$ . Thus, the next relation is used:

$$\tau_A = \frac{\frac{1}{n} \sum_{i=1}^n I_A [c/s]}{C_A[at/cm^3] \cdot R^2[cm^2] \cdot SR[cm/s] \cdot \cos(\theta)} \quad (\text{Equation III-20})$$

The useful ion yield for In and Ga considering the incident angle is presented in Figure III-13 and Figure III-14.

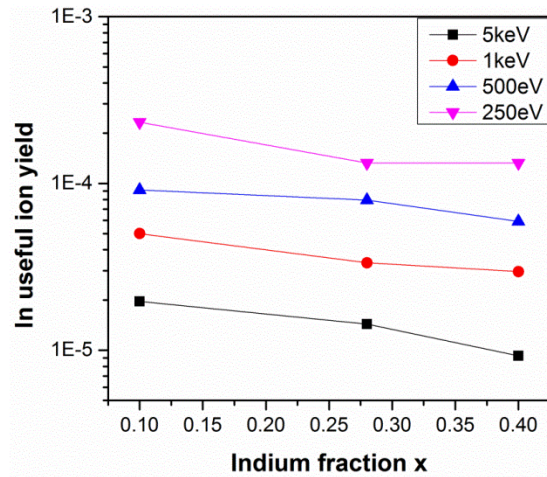


Figure III-13 Indium ion yield as a function of  $0.1 < x < 0.4$  in  $\text{In}_x\text{Ga}_{1-x}\text{As}$  under oxygen beam sputtering at  $40^\circ$  (5 keV),  $39^\circ$  (1 keV),  $42^\circ$  (500 eV),  $49^\circ$  (250 eV) angles.

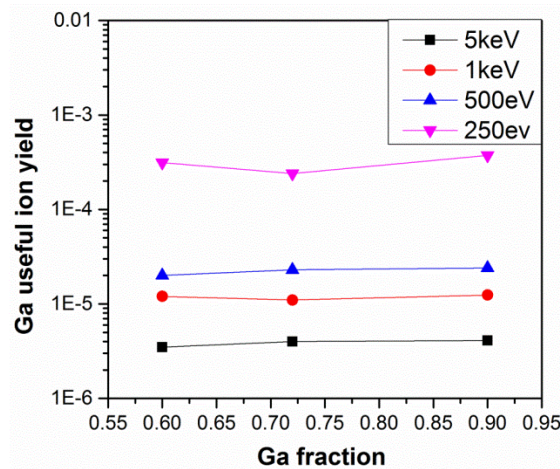


Figure III-14 Gallium ion yield as a function of Ga  $[1-x]$  fraction in  $\text{In}_x\text{Ga}_{1-x}\text{As}$  under oxygen beam sputtering at  $40^\circ$  (5 keV),  $39^\circ$  (1 keV),  $42^\circ$  (500 eV),  $49^\circ$  (250 eV) angles.

The relative useful yield can be found from Equation III-19 and can be expressed as well as an RSF ( $1/\text{RSF}_{\text{In}}$ ). The relative ion yield for In and Ga is shown in Figure III-15. The In ion yield is about three or four times higher than the Ga ion yield and this is observed for all primary energies (5000-250 eV). It could be explained by the bond strength of In-O ( $< 320.1$  KJ/mol) which is lower compared to Ga-O (353.5 KJ/mol) [D. R. Lide, 2005].

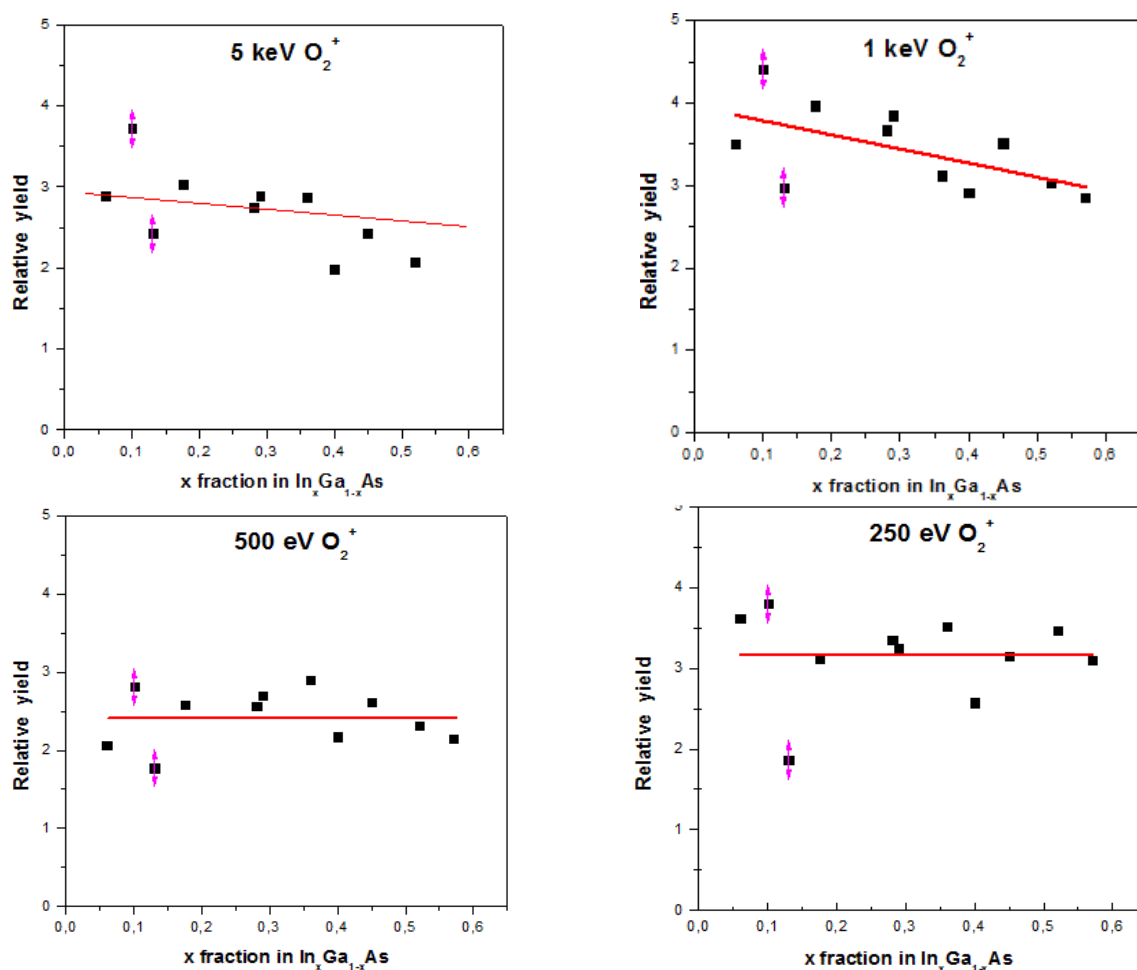
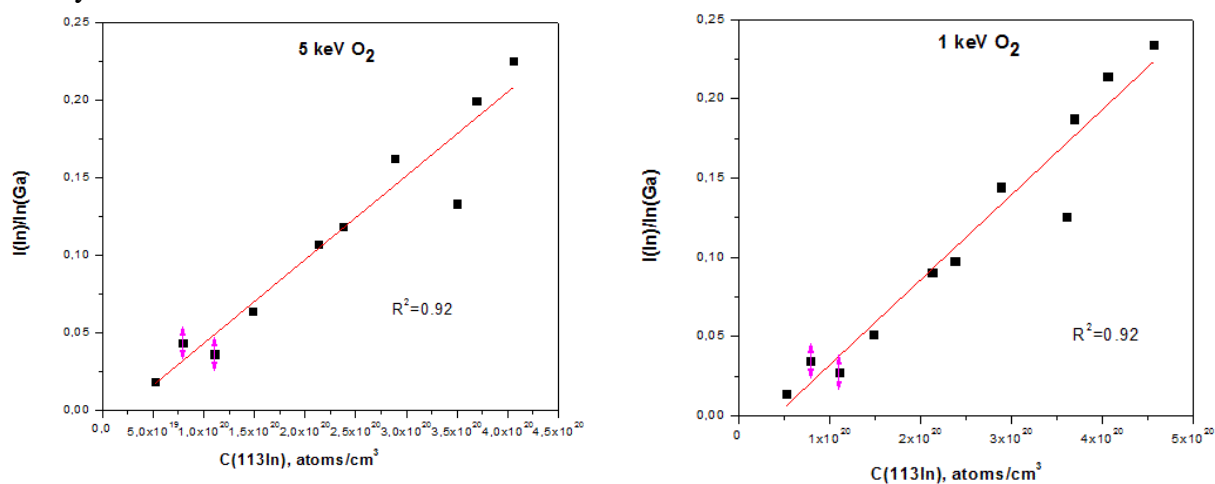


Figure III-15 Relative ion yield as a function of indium composition in  $\text{InGaAs}$  under oxygen sputtering at a) 5 keV, b) 1 keV, c) 500 eV and d) 250 eV energies.

The RSF for the indium signal can be found using the Equation III-3. The concentration of indium as a function of ratio of secondary is presented in Figure III-16. The slope (RSF) values are given in Table III-5, which was used to calibrate the indium secondary ions signal in  $\text{InGaAs}$  thin layers.



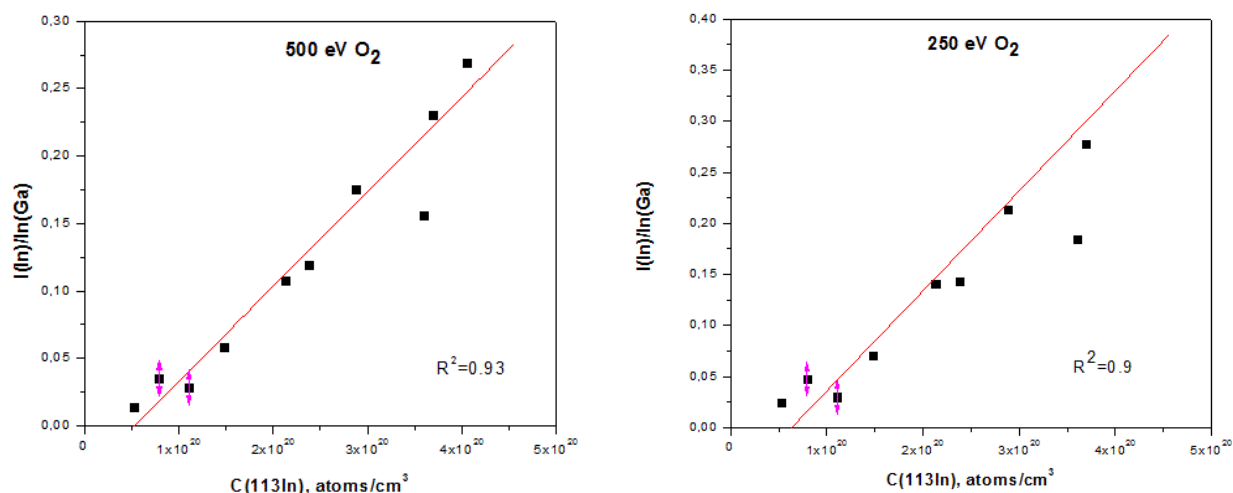


Figure III-16 The concentration of indium as a function intensities ratio under oxygen sputtering at a) 5 keV, b) 1 keV, c) 500 eV, d) 250 eV energies.

**Table III-5** RSF value for Indium under oxygen sputtering at the energy range 5000-250 eV

Impact energy	5 keV	1 keV	500 eV	250 eV
RSF <sup>-1</sup> [113In]	1.85·10 <sup>21</sup>	1.85·10 <sup>21</sup>	1.42·10 <sup>21</sup>	1.02·10 <sup>21</sup>

Finally, to find concentration of Ga the next relation is used:

$$C_{Ga} = \frac{\rho}{2} - C_{In} \quad (\text{Equation III-21})$$

### III.3.2 Quantitative analysis of InGaAs quantum well using SIMS

Investigation of composition in thin films (in thickness of less than 10 nm) is difficult, as it requires the high depth resolution of the technique. In general, the symmetry and abruptness of QW interfaces in III-V heterostructures is an essential parameter for optical and electronic properties of devices. An asymmetry in the QW shape can result in significant changes in the properties of QW structures although a symmetrical rectangular form of QW is aimed during growth [W. C. H. Choy et al., 1998]. Here, the quantification of thin films of few nanometers in thickness using magnetic SIMS is discussed.

The three samples containing the InGaAs/AlAs QWs (described in Chapter II.1.4.1) with the same nominal indium composition (10%) and 6-19 nm in thickness were studied using magnetic SIMS. The low oxygen ion beam sputtering ( $E = 500$  eV) was used to study the indium composition in InGaAs QWs. The experimental conditions can be found in detail in Chapter II.2.1.5. In general, the low energy ion beam bombardment has to be employed to obtain high

depth resolution. Additionally, it was mentioned above, the low oxygen ion beam sputtering leads to an increase of the ion yield of In and Ga.

Figure III-17 shows the SIMS depth profiling of three InGaAs QWs in thickness 6, 10 and 19 nm are presented. The thickness of layers was measured using STEM. To calibrate the x-scale time (count/sec) into depth (nm), the sputter rate was estimated for each layer and point-to-point calibration was applied. The sputter rate for each layer is given in Table III-6. The variation of sputter rate for GaAs, InGaAs and AlAs can be explained by the local bond breaking ion emission model. The binding energy of In-In bond strength is lower ( $100 \pm 8$  KJ/mol) than Ga-Ga ( $112 \pm 7$  KJ/mol) and Al-Al bonds ( $133 \pm 6$  KJ/mol), and accordingly, the sputter rate is higher for InGaAs [D. R. Lide, 2005].

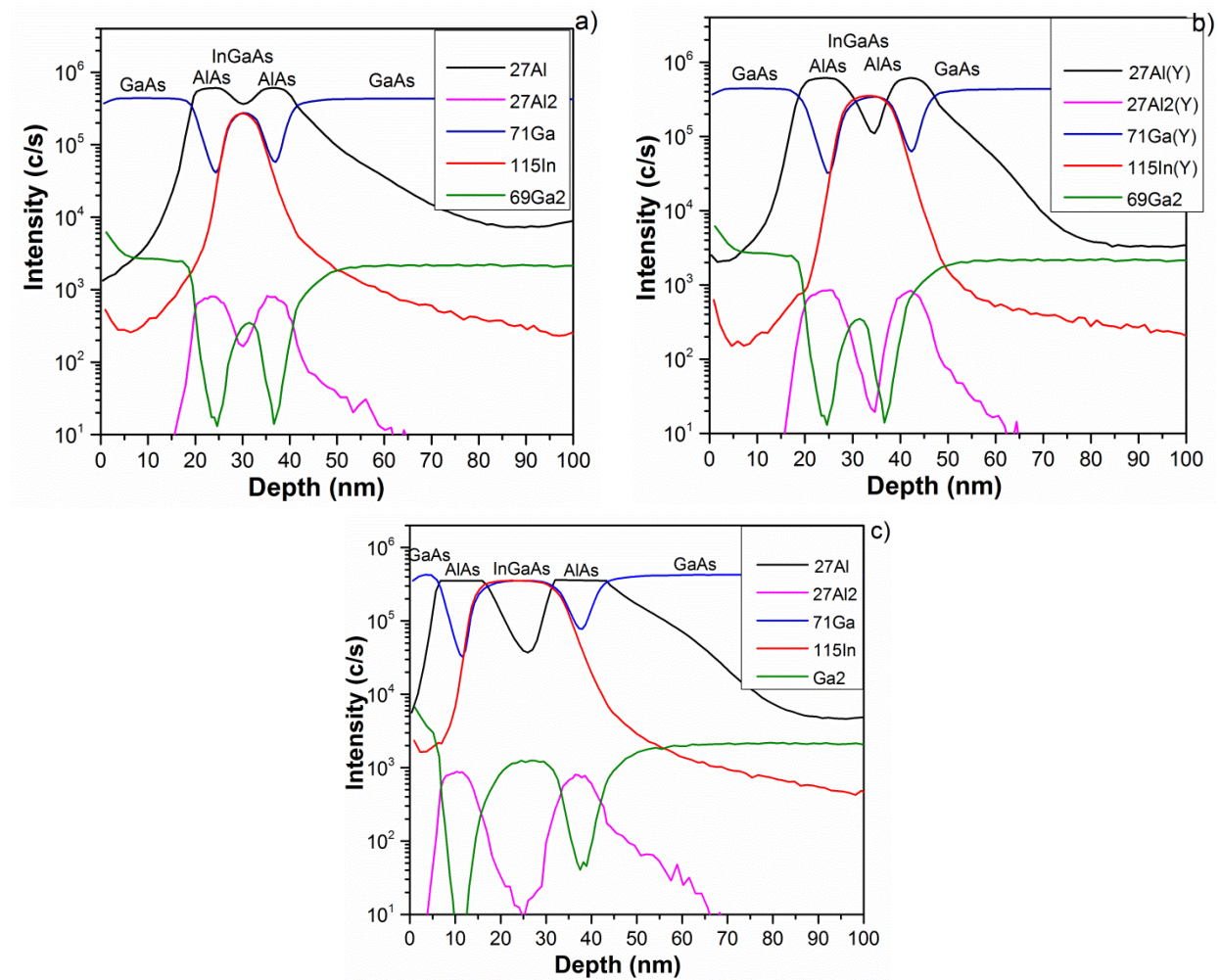


Figure III-17 SIMS profiles of InGaAs/AlAs QWs under oxygen bombardment, a) InGaAsQW7 of 6 nm in thickness, b) InGaAsQW5 of 10 nm in thickness and c) InGaAsQW6 in 19 nm

The flat indium signal for thick InGaAs QW in 19 nm (Figure III-17 c) is observed, whereas reducing the thickness (less than 10 nm) of the QW leads to reducing the signal in a shape (Figure III-17 a). This is explained by the limited depth resolution of the instrument. The depth resolution will be discussed in details in the next Chapter IV. Figure III-18 shows the comparison of quantified In profiles using RSF values described above. Indium secondary ion

signal (over the curve) was normalized by the average Ga signal. To superpose the profiles the sputter rate  $SR=0.03$  nm/s was applied to all three profiles. Note that the measurements were performed consecutively and under the same experimental conditions used for the reference sample. The indium composition in InGaAs QWs is given in

Table III-7. The decreasing of indium composition with reducing InGaAs layer thickness is observed. The significantly reduced indium composition is observed for InGaAs QW7 in thickness of 6 nm compared to InGaAs QW5 in thickness of 19 nm.

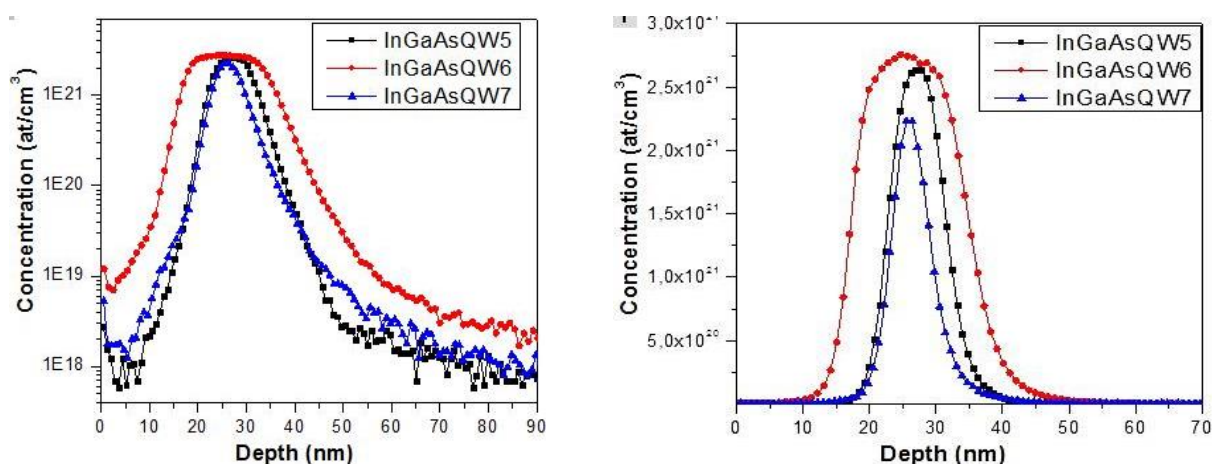


Figure III-18 Indium profiles of InGaAs/AlAs QWs with the different thickness (in logarithmic and linear scales): red color line corresponds to InGaAsQW6 in 19 nm, blue line to InGaAsQW7 in thickness of 6 nm and black line to InGaAsQW5 of 10 nm in thickness

**Table III-6 Sputter rate measurements of III-V heterostructures under oxygen sputtering**

	GaAs	AlAs	InGaAs
Sputter rate, nm/s	0.04	0.03	0.20

**Table III-7 Concentration comparison of InGaAs QWs**

	InGaAs QW7: 6 nm	InGaAs QW5: 10 nm	InGaAs QW6: 19 nm
Concentration, at/cm <sup>3</sup>	$2.2 \cdot 10^{21}$	$2.6 \cdot 10^{21}$	$2.8 \cdot 10^{21}$
fraction x, %	10	13	13

### III.3.3 Quantitative analysis of InGaAs quantum well using complementary techniques

The InGaAs/AlAs QWs (discussed above) were studied by  $\mu$ PL measurements performed at room temperature. Experimental details can be found in Appendix III.C. As expected, one can observe a blue shift of the InGaAs band-to-band emission when decreasing the InGaAs QW thickness. The energy values of RT PL peaks are reported in Table III-8. From the thicknesses measured from STEM images on these different samples and from the position of the PL peak, one can extract from simulation the In composition of the InGaAs QW. We found an In

composition of 15% for all these QWs. The calculation is performed using the 3D nanodevice simulator “Nextnano”.

Table III-8 Characteristics of the InGaAs QWs obtained using PL

	Measured InGaAs thickness (nm)	PL peak energy (eV)	Extracted In content at. (%)
<b>InGaAs QW7</b>	6	1.326	15
<b>InGaAs QW5</b>	10	1.254, 1.3015	15
<b>InGaAs QW6</b>	19	1.25, 1.276	15

Furthermore, Auger measurements were performed under Ar<sup>+</sup> sputtering with the energy of 500 eV and electron beam of 10 keV. The experimental details can be found in Chapter II.2.3. The indium composition was estimated using the reference samples described in section III.3.1. The RSF values used to calibrate Auger profiles are given in Table III-9.

Table III-9 Relative sensitivity factors for III-V elements using Auger

$S_x = \frac{[As]}{[X]} \frac{I_{p-p\ x}}{I_{p-p\ As}} S_{As}$	<b>Ga</b> (LMM, 1070 eV)	<b>As</b> (tabulated value) (LMM, 1228 eV)	<b>In</b> (MNN, 404 eV)
<b>RSF</b>	0.179	0.11	0.386

The Indium profiles of InGaAs QWs are plotted in Figure III-19. The flat shaped indium signal coming from InGaAs QW of 19 nm in thickness is observed, whereas reduced indium signal is observed in InGaAs QW7 in thickness of 7 nm. This observation is similar to the SIMS observation described in the previous section. Note, the slight variation of indium composition(in depth 40 nm) following the downslope is observed for InGaAs QW6 using both SIMS and Auger techniques. It can be explained by the slight non-uniformity layer in thickness and presence of defects(APBs)(see Figure III-7). Indium composition comparison using the SIMS, Auger and PL measurements is given in Table III-10. The Auger and SIMS values for InGaAs QW6 are close to that obtained by PL measurements (14 %). While the indium composition in InGaAs QW5 and InGaAs QW7 by Auger and SIMS is lower than values extracted by PL. The measurement for InGaAs QW6 of 19 nm in thickness shows more reliable analysis than for thinner layers (less than 5-10 nm). It can be seen that the indium composition is underestimated for thin InGaAs QWs. These observations can be explained by the limitations of depth resolution (less than 3-4 nm) for both techniques, which is in the same magnitude that thickness of layers. This prevents the maximum of indium signal to be reached. The presence of aluminum using SIMS and Auger in the InGaAs QWs can be also explained by the fact that the depth resolution is insufficient to discriminate whether Al decays in the InGaAs layer. (see Figure II-17).

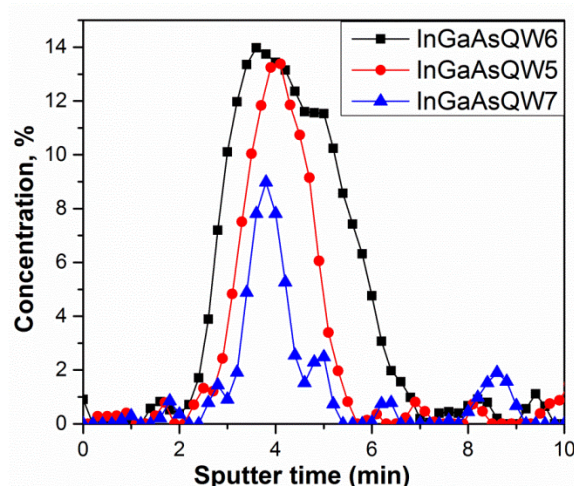


Figure III-19 Indium profiles obtained using Auger technique, where black color corresponds to InGaAsQW6 of 19 nm in thickness, red corresponds to InGaAsQW5 in thickness of 10 nm and blue corresponds to InGaAsQW7 of 6 nm in thickness.

**Table III-10** Comparison of results obtained by SIMS, Auger, and PL

	InGaAs QW7	InGaAs QW5	InGaAs QW6
Thickness, nm	6	10	19
SIMS [x], $\pm 0.03$	10	13	13
Auger [x], $\pm 0.03$	9	13,3	14
PL [x], $\pm 0.01$	15	15	15

### III.3.4 Quantification using molecular $\text{MCs}^+$ ions under low energy sputtering

The linear calibration and absence of matrix effect for III-V materials were observed under high cesium ion beam sputtering (5 keV) by Y.Gao [Y. Gao, 1988]. The absence of matrix effect is reported for III-V materials using  $\text{MCs}^+$  mode.  $\text{MCs}^+$  ion yield is independent of the primary current density. The higher ion yield of III-Group elements compared to V group was reported. The V-group elements have a higher electronic affinity and higher negative elementary ion yield than V-group elements and, as a result, a lower neutral yield [Y. Gao, 1988]. The composition of alloy materials can be found using the following equation:

$$x[A] = \left( 1 + \frac{\alpha_B}{\alpha_A} \cdot \frac{I_{\text{CsB}}}{I_{\text{CsA}}} \right)^{-1} \quad (\text{Equation III-22})$$

Where  $x$  is the composition of element A,  $I_{\text{CsB}}$ , and  $I_{\text{CsA}}$  are intensities for element A and reference element B, and  $\frac{\alpha_B}{\alpha_A}$  is an RSF value.

It is important to understand the influence of cesium sputtering energy on quantitative analysis for InGaAs material. The RSF calibration curve for the energy range 1000-250 eV for cesium sputtering is plotted in Figure III-20. The linear dependence on the ratio of CsIn/CsAs to CsGa/CsAs is observed for all energies and the slope is given in Table III-11. The slope or RSF for a primary energy of 1 keV (at an incident angle  $63^\circ$ ) is found to be similar to that at 250 eV (at an incident angle of  $69^\circ$ ).

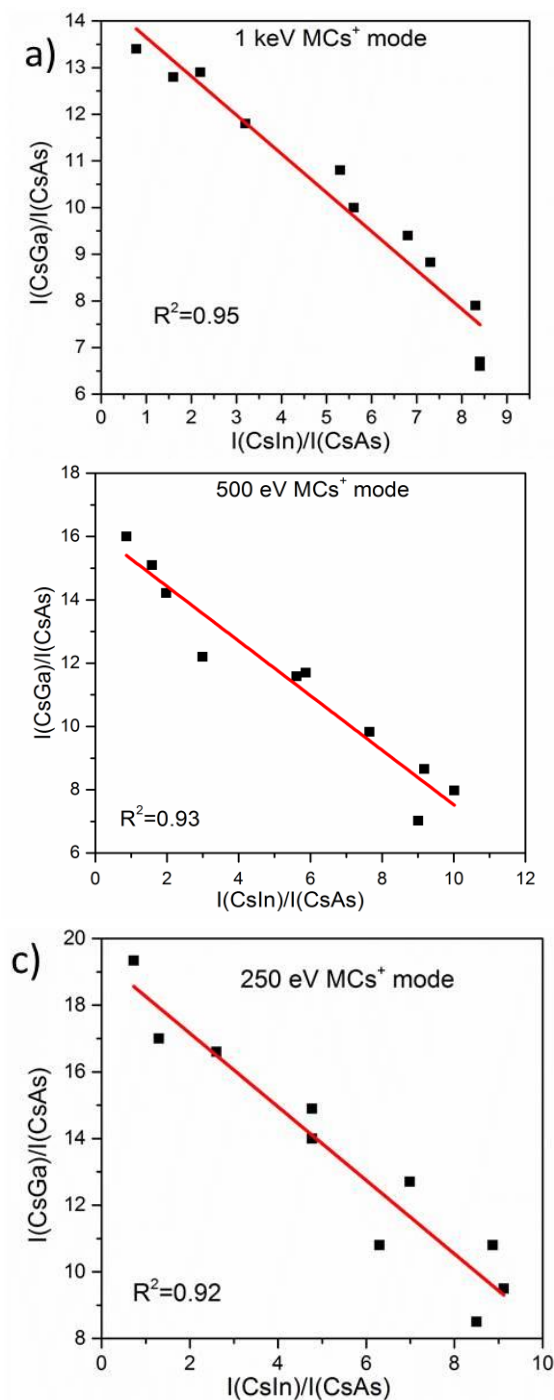


Figure III-20 RSF calibration curve for InGaAs under low ion beam sputtering at a) 1keV, b) 500eV , c) 250eV energies.

**Table III-11** RSF value for indium under cesium sputtering using  $\text{MCs}^+$  mode at the energy range 1000-250 eV

Energy, eV	1000	500	250
RSF	0.8	0.86	1.1

### III.4 Development of a SIMS protocol for n-doped GaAs in 2D and 3D architectures

Silicon (IV-group element) is often used to obtain n-type doping in GaAs. The silicon incorporation in GaAs is known as amphoteric. It means that either the gallium or arsenic atoms can be replaced by silicon atoms and behaves as donors and acceptors, respectively. The incorporation of silicon atoms in GaAs is controlled by the growth conditions (temperature, pressure etc.). The doping efficiency, i.e. the incorporation of Si atoms in Ga sites, can be estimated by knowing the total number Si dopants (concentration) and carrier concentration measured by Hall effect and presented later. Here, the doping profiling using SIMS and ToF-SIMS is described in detail.

Doping concentration in planar III-V materials and III-V trenches was measured using magnetic sector SIMS and ToF-SIMS techniques. The n-doped GaAs/non-doped GaAs sample was grown by MOCVD on planar and patterned 300 mm Si wafers. More details can be found in Chapter II.1.4.4. The experiments were performed under cesium sputtering at an energy of 9 keV and incident angle of  $55^\circ$  using SIMS SC-Ultra instrument. For ToF-SIMS measurements, the  $\text{B}_1^+$  ions (dose= $4.5 \cdot 10^{14}$  at/cm<sup>2</sup>) at energy 25 keV and cesium ion beam sputtering at an energy of 1 keV and an incident angle of  $45^\circ$  were used.

For quantitative analysis of silicon dopants in GaAs, the reference sample was used. The Si-ion implanted reference sample with known Si-dose ( $5 \cdot 10^{14}$  atoms/cm<sup>2</sup>) was studied using SIMS. Figure III-21 shows the SIMS profile of the Si-implanted sample. Si signal was followed using with  $^{28}\text{Si}^{75}\text{As}$ ,  $^{28}\text{Si}^{69}\text{Ga}$ , and  $^{28}\text{Si}$  signals. The higher ion yield of  $^{28}\text{Si}^{75}\text{As}^-$  compared to  $\text{Si}^-$  the signal can be observed (Figure III-21) and thus, allows this signal for quantification of silicon dopants be used.

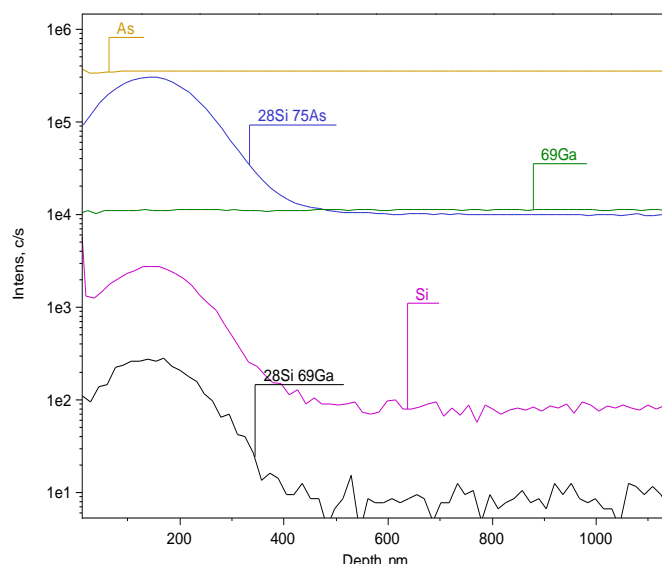


Figure III-21 SIMS profile of Si-implanted reference sample in GaAs matrix under  $\text{Cs}^+$  bombardment at 9 keV primary energy using SIMS.

The silicon concentration was estimated through the known dose and using Equation III-4. Figure III-22 shows the quantified profile of  $^{28}\text{Si}^{75}\text{As}^-$ ,  $^{28}\text{Si}^-$  and  $^{28}\text{Si}^{69}\text{Ga}^-$  signals. The estimated RSF values using magnetic SIMS and ToF-SIMS are given in Table III-12.

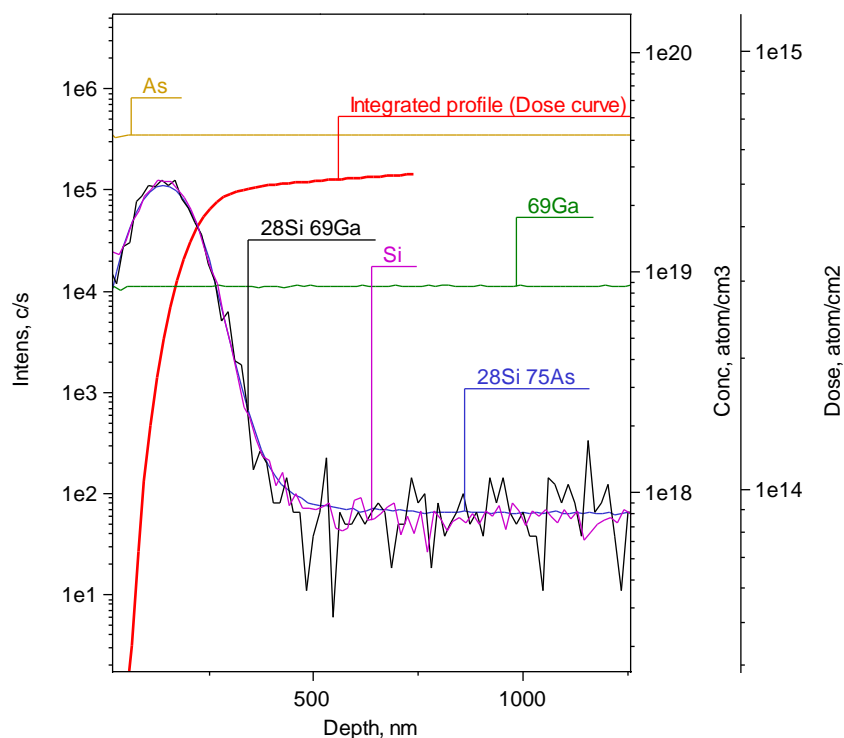


Figure III-22 Concentration profile of Si-ion implanted reference sample using under  $\text{Cs}^+$  bombardment at 9 keV primary using SIMS.

**Table III-12** RSF values using magnetic SIMS and ToF-SIMS

	$^{28}\text{Si}/\text{Ref. } (^{75}\text{As})$	$^{28}\text{Si}^{69}\text{Ga}/\text{Ref. } (^{75}\text{As})$	$^{28}\text{Si}^{75}\text{As}/\text{Ref. } (^{75}\text{As})$
<b>RSF [SIMS], atom/cm<sup>3</sup></b>	$3.3 \cdot 10^{21}$	$3.3 \cdot 10^{22}$	$2.9 \cdot 10^{19}$
<b>RSF [ToF-SIMS], atom/cm<sup>3</sup></b>	$3.6 \cdot 10^{21}$	-	$1.5 \cdot 10^{20}$

The n-doped GaAs/non-doped GaAs/Si sample(see Chapter II.1.4.4) was studied using magnetic and ToF-SIMS techniques. The SIMS and ToF-SIMS profiles are shown in Figure III-23 and Figure III-24. Si profiling in GaAs matrix has good correspondence obtained using both SIMS techniques. The sample thickness was measured by ellipsometry. The Si-doped region in GaAs can be observed following the  $^{28}\text{Si}$ ,  $^{28}\text{Si}^{69}\text{Ga}^-$  and  $^{28}\text{Si}^{75}\text{As}$  signals which are abruptly decreased in the non-doped GaAs region. Note that  $^{28}\text{Si}^{69}\text{Ga}^-$  signal is not observed using ToF-SIMS due to lower sensitivity compared to magnetic SIMS instrument. Si concentration of  $8.9 \cdot 10^{18}$  atoms/cm<sup>3</sup> and  $1 \cdot 10^{19}$  atoms/cm<sup>3</sup> was estimated in the doping region up to 70 nm using magnetic SIMS and ToF-SIMS, respectively.

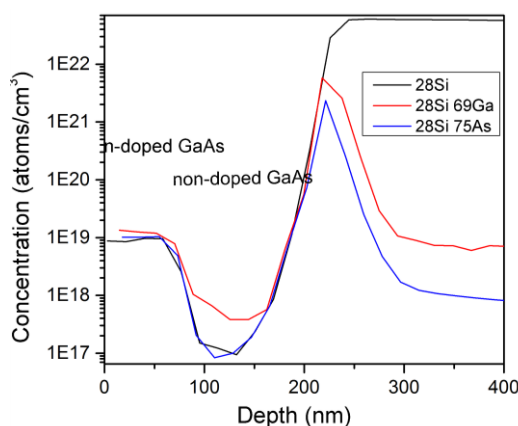


Figure III-23 SIMS profiling of Si-doped GaAs/non-doped GaAs/Si under cesium sputtering.

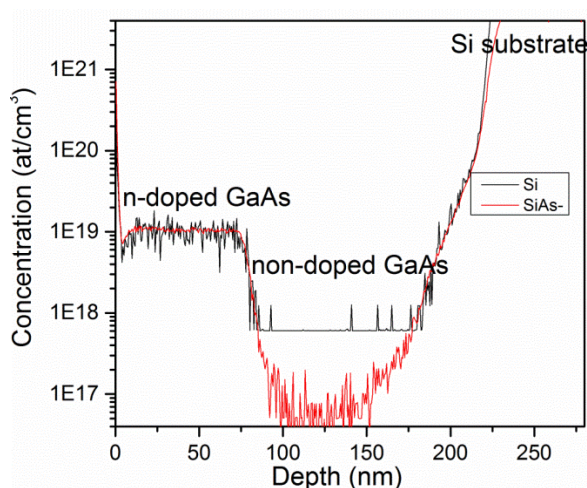


Figure III-24 ToF-SIMS profiling of GaAs/non-doped GaAs/Si under cesium sputtering.

Si-doped GaAs/non-doped GaAs/Si trenches(see Chapter II.1.4.4) were studied using ToF-SIMS technique. The similar experimental conditions were as for n-doped GaAs/non-doped GaAs, described above. To reduce the contribution of Si from SiO<sub>2</sub> walls (see II.1.4.3) surrounding the

III-V trenches were etched using hydrogen fluoride (HF) 10% during 2 minutes. The initial state of trenches after HF etching is given in Figure III-25. The roughness of the surface was measured by AFM. The low roughness and absence of SiO<sub>2</sub> walls were observed.

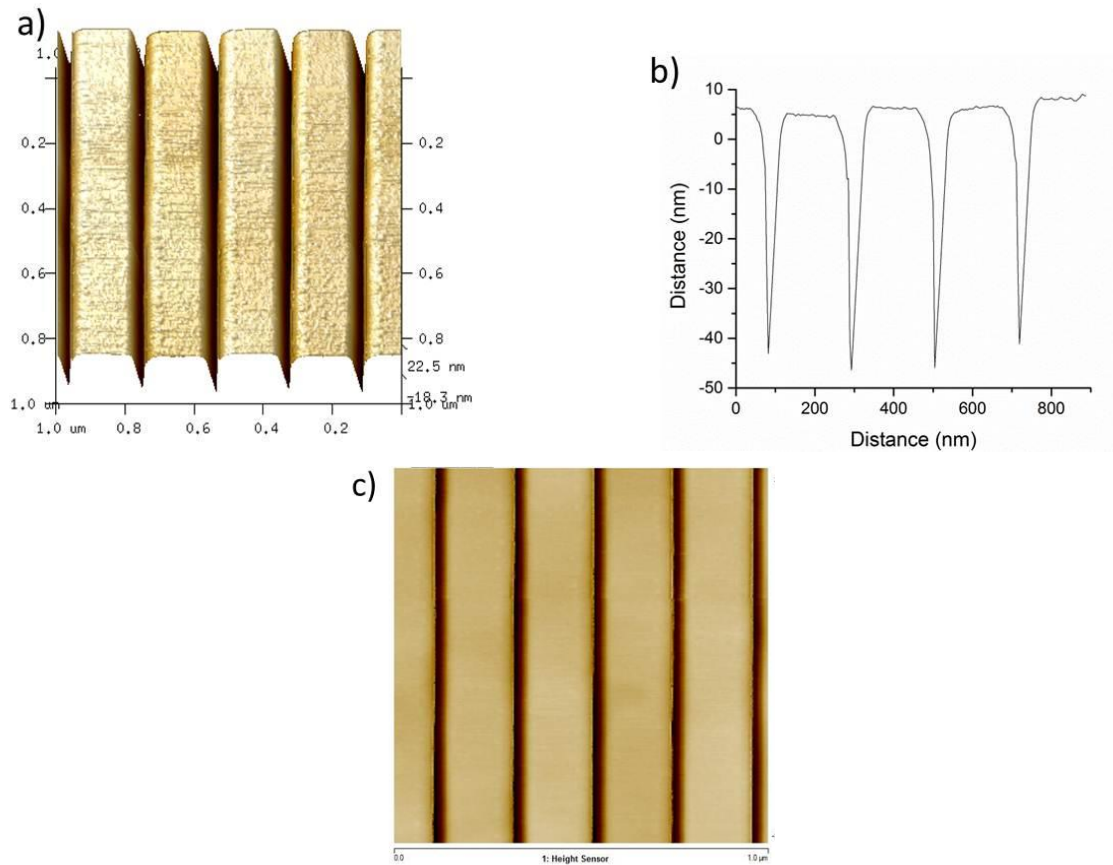


Figure III-25. Initial topography of n-doped GaAs trenches selectively grown on patterned 300 mm wafers, where a) 3D image, b) profile along the trenches and c) 2D view of III-V trenches ( $-59 \text{ nm} < z < 22.5 \text{ nm}$ )

The samples were studied in parallel and perpendicular orientation to the trenches using ToF-SIMS technique (see Figure III-26).

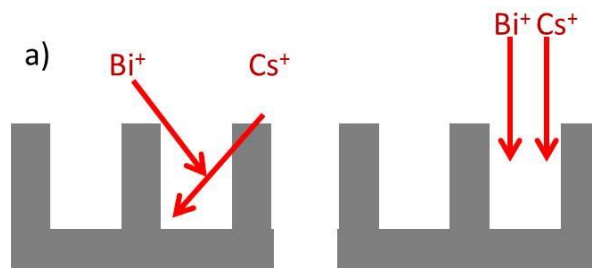


Figure III-26 Schematic illustration of sputtering of GaAs trenches using Cs<sup>+</sup> sputtering beam at an incident angle of 45° and aligned a) perpendicular to the trenches, b) parallel to the trenches by ToF-SIMS technique.

A ToF-SIMS profile of n-doped GaAs trenches in parallel orientation to the trenches is shown in Figure III-27. The Si-doped layer is not distinguished following the Si<sup>-</sup> and SiAs<sup>-</sup> signals.

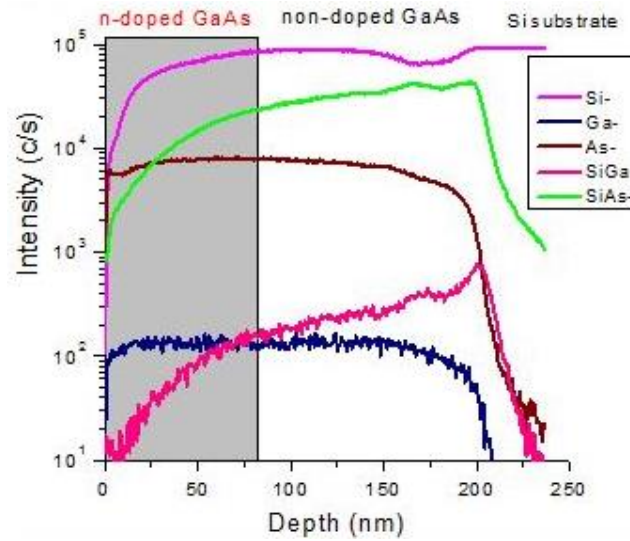


Figure III-27 ToF-SIMS profile of Si-doped GaAs/non-doped GaAs/Si trenches under cesium bombardment aligned in a parallel direction to the trenches and using a  $\text{Bi}^+$  ion analysis beam.

AFM image of topography formation under cesium sputtering in parallel orientation to the GaAs trenches is shown in Figure III-28. It can be observed that hillocks form on the surface of GaAs and are distributed homogeneously.

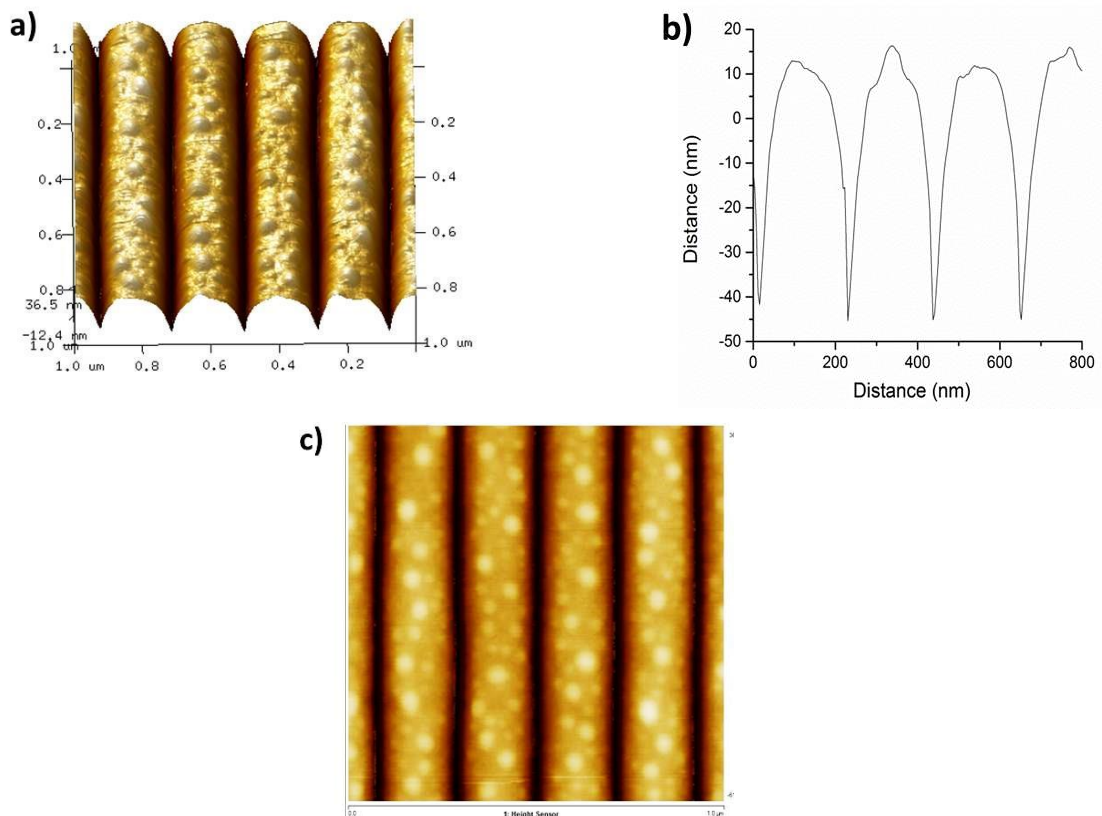


Figure III-28 Topography image of GaAs trenches under sputtering  $\text{Cs}^+$  bombardment aligned in perpendicular to the trenches and using  $\text{Bi}^+$  analysis ion beam, where a) 3D image, b) profile along the trenches and c) 2D view of III-V trenches ( $-61.3 \text{ nm} < z < 36.5 \text{ nm}$ )

Figure III-29 shows the Si-doping profiling in trenches in a perpendicular orientation of the cesium ion beam with respect to the III-V trenches. The  $^{28}\text{Si}^{75}\text{As}^-$  signal obtained under perpendicular orientation is distinguished. The slight instability of  $\text{As}^-$  signal is observed and explained by the non-homogeneous  $\text{Cs}^+$  sputtering, which occurs in this orientation of the trenches. The topography formation under perpendicular orientation with respect to the trenches is shown in Figure III-30.

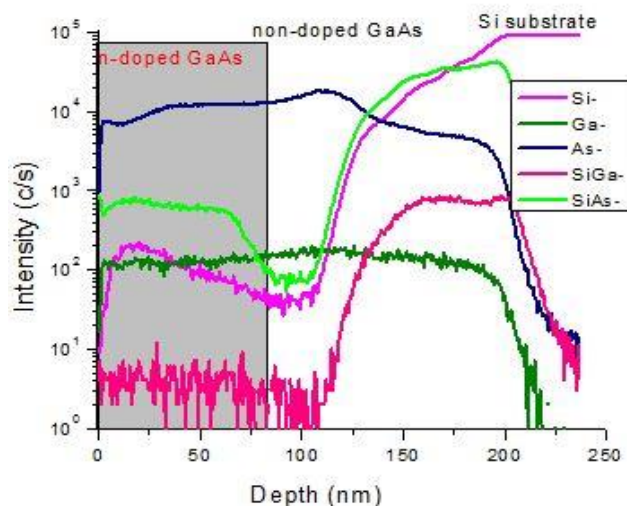


Figure III-29 ToF-SIMS profile of Si-doped GaAs under sputtering  $\text{Cs}^+$  bombardment aligned in a perpendicular direction to the trenches and using  $\text{Bi}^+$  analysis ion beam.

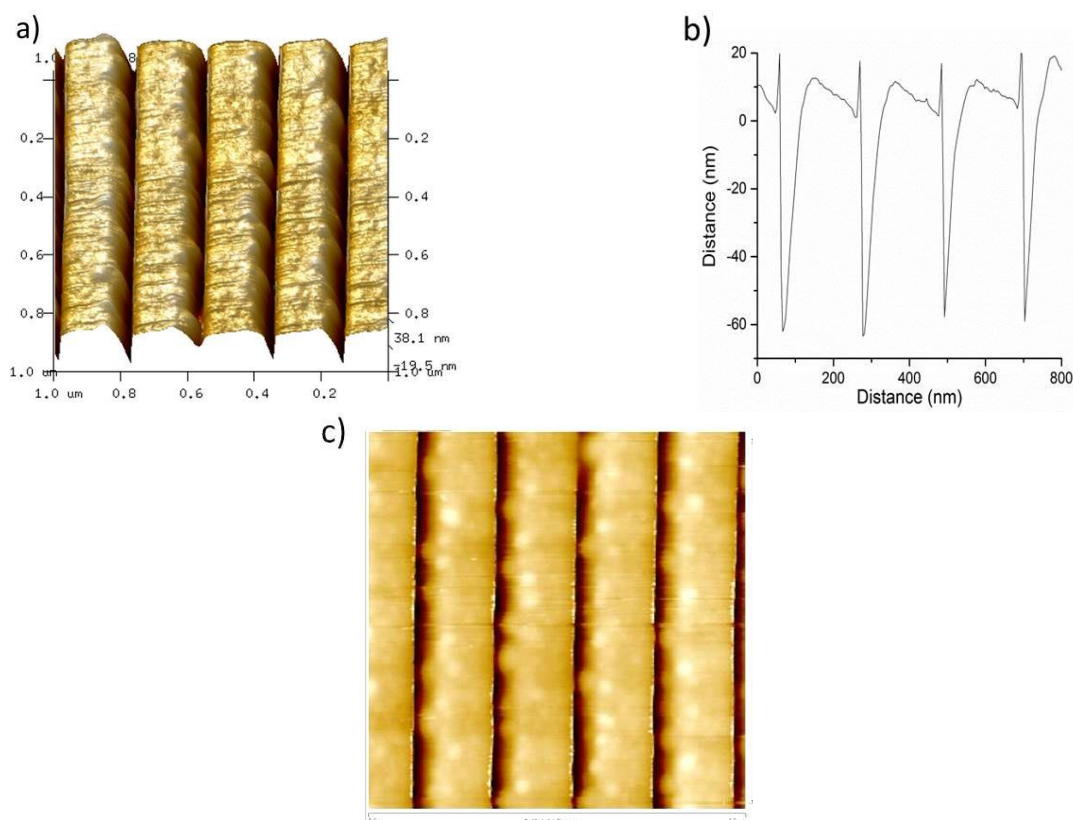


Figure III-30 Topography image of GaAs trenches under  $\text{Cs}^+$  bombardment (1 keV) aligned perpendicular orientation to the trenches and using  $\text{Bi}^+$  analysis beam (25 keV), where a) 3D image, b) profile along the trenches and c) 2D view of III-V trenches ( $-77.1 \text{ nm} < z < 38.1 \text{ nm}$ )

RMS values under parallel and perpendicular orientation to the GaAs trenches are given in Table III-13. Slightly less roughness is observed under parallel orientation compared to a perpendicular orientation.

**Table III-13** RMS values under cesium bombardment aligned in parallel and perpendicular orientation with respect to the trenches

	Initial state	Bombardment in parallel direction	Bombardment in perpendicular direction
RMS (one trench) 153.85 x 968 nm	1.4 nm	5.7	5.8
RMS (723.98 nm x 751.3 nm)	12.2 nm	15.1 nm	16.0 nm

The Si concentration in trenches was calculated by following the  $^{28}\text{Si}^{75}\text{As}^-$  using the  $^{69}\text{Ga}^-$  as a reference signal. The estimated RSF value of  $1.6 \cdot 10^{18}$  at/cm<sup>3</sup> was used to calculate the Si concentration. Figure III-31 shows the comparison of  $^{28}\text{Si}^{75}\text{As}^-$  signals measured in parallel and perpendicular orientations. It can be seen that in parallel orientation the SiAs<sup>-</sup> signal is less defined compared to a perpendicular orientation to the trenches due to higher contribution from Si substrate as a result of the geometry of sputtering (see Figure III-26). Additionally, SiO<sub>2</sub> walls which may be partially present as well whereas in the perpendicular orientation the analysis beam does not “see” the silicon substrate and sidewall contribution is reduced. The sputter rate for both orientations is similar and given in Table III-14.

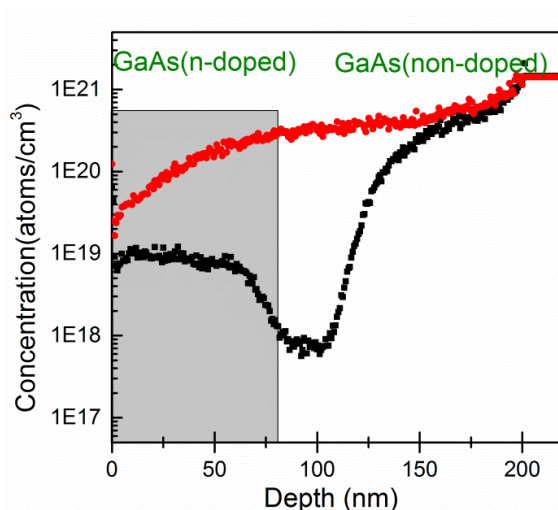


Figure III-31 Si-doping profiling in GaAs(n-doped)/GaAs/Si trenches under Cs<sup>+</sup> bombardment aligned to parallel (in red color) and in a perpendicular orientation to the trenches (in black color).

Figure III-32 shows the comparison of Si-doping in GaAs in 2D and 3D architectures. A slightly higher value of silicon dopants in planar compared to patterned sample can be seen from Figure III-32 and possibly due to the partially present of SiO<sub>2</sub> walls.

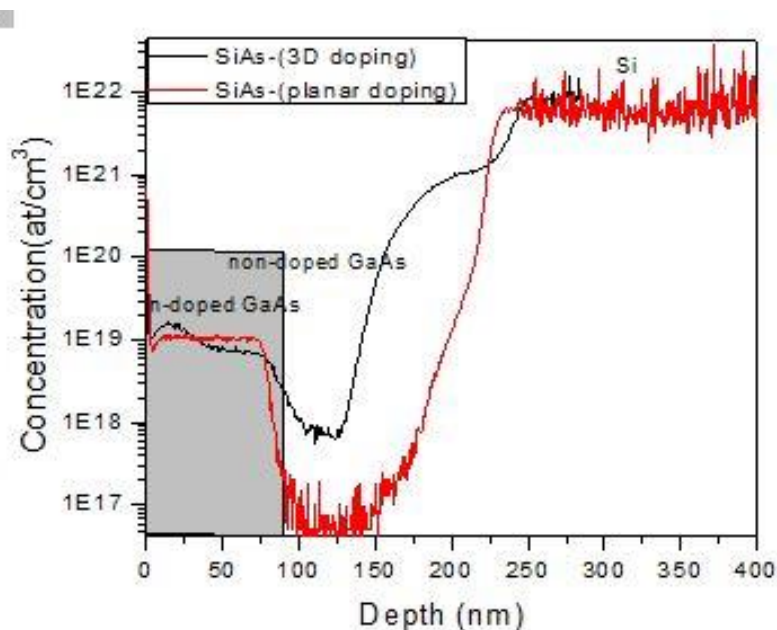


Figure III-32 Si-doping profiling in GaAs in 2D and 3D architectures

**Table III-14** Sputter rate of GaAs trenches under  $\text{Cs}^+$  bombardment with 1 keV primary energy and using the  $\text{Bi}^+$  analysis ion beam

	planar GaAs	III-V trenches cesium ion beam in perpendicular direction wtf trenches	III-V trenches cesium ion beam in perpendicular direction wtf trenches
<b>Sputter rate, nm/s</b>	0.6	0.7	0.7

The carrier concentration  $n$  were performed by Hall effect measurements at room temperature. The concentration of  $n=4 \cdot 10^{18} \text{ cm}^{-3}$  ( $\rho=1 \cdot 10^{-4} \Omega \cdot \text{cm}$ ) was estimated for samples in 2D and 3D architectures (see Table III-15). A higher dopants concentration compared to carrier measurements for both samples is observed. We assume that the silicon dopants are not completely activated due to possibly Si clustering and presence of defects participating in compensation. Additionally, the high dopants concentration (more than  $3 \cdot 10^{18} \text{ cm}^{-3}$ ) leads to a decrease in the carrier concentration and thus, to lower mobility of electrons. [X. Tang et al., 1989].

**Table III-15** Si concentration in GaAs measured using SIMS and ToF-SIMS techniques

	Carrier concentration (Hall effect measurements)	Si-concentration (SIMS)	Si-concentration (ToF-SIMS)
n-doping GaAs planar	$4 \cdot 10^{18}$	$8.9 \cdot 10^{18} (\pm 0.4 \cdot 10^{18})$	$9 \cdot 10^{18} (\pm 1 \cdot 10^{18})$
n-doping GaAs in 3D	$4 \cdot 10^{18}$	-	$11 \cdot 10^{18} (\pm 1 \cdot 10^{18})$

**Conclusions:** this chapter reported on the chemical compositional analysis for InGaAs channel materials and doping profiling for future generations of transistors. The development of reference samples using ion implantation for doping and impurities measurements is described as well as the development of compositional analysis for InGaAs and AlGaAs layers using different techniques (RBS, PIXE, PIGE etc.). The decrease of sputter rate with increasing indium fraction  $x$  in  $\text{In}_x\text{Ga}_{1-x}\text{As}$  was observed for high and medium impact energy (500 eV-5000 eV) oxygen ion beam bombardment, whereas at 250 eV impact energy the sputter rate variation with composition is minor. The linear dependence of sputter yield on impact energy is observed. Indeed, the extremely low impact energies (less than 500 eV) lead to very low sputter yields. A linear In/Ga ion intensity ratio as a function of composition  $x/(1-x)$  is observed for high and low primary energy oxygen sputtering. The calibration curve for indium as a function of intensities of In/Ga ion intensity ratio in the impact energy range 250-5000 eV is determined and was used to quantify the indium composition in InGaAs layers.

It was observed that reducing the thickness of InGaAs QWs down to 10 nm leads to a change of indium signal from rectangular to Gaussian shape. These results were compared with quantitative analysis using PL and Auger was performed. Reliable quantitative values were observed for InGaAs QW thicker than 10 nm for SIMS and Auger in good agreement with PL measurements. However, for films thinner than 10 nm, SIMS and Auger measured lower indium atomic concentration values compared to that extracted from PL measurements due to limitations of depth resolution (less than 3-4 nm), which is of the same order of magnitude as the layer thickness.

Furthermore, quantification for InGaAs using the  $\text{MCs}^+$  mode was described under medium and low ion beam cesium sputtering. The calibration curve for indium and gallium is given and it was demonstrated that RSF values for the primary energy of 250 eV are similar to those at 1 keV.

Finally, quantitative analysis for Si-doping in GaAs on planar and patterned Si wafers was developed using ToF-SIMS and SIMS. It was found that using SiAs, SiGa ions the Si dopants in GaAs/Si to be distinguished. Moreover, orientating the III-V trenches in a perpendicular orientation to the cesium ion beam is preferable for Si dopant measurements in GaAs on patterned Si wafers. This is because the contribution from the substrate is minimized in this geometry, whereas when the III-V trenches are oriented parallel to the ion beam the silicon contribution is much higher and comes mainly from the silicon substrate.

#### REFERENCES:

- [C. A. Andersen, et al. 1972] Ion Microprobe Mass Analyzer, *Science*, **175** (4024), pp. 853-860.
- [A. Benninghoven, et al. 1987] Secondary Ion Mass Spectrometry: Basic Concepts, Instrumental Aspects, Applications and Trends, Wiley.
- [V. Bondarenko, 2004] Positron annihilation study of equilibrium point defects in GaAs, Phd thesis, Mathematisch-Naturwissenschaftlich-Technischen Fakultät.
- [W. C. H. Choy, et al. 1998] The effect of growth interruption on the properties of InGaAs/InAlAs quantum well structures, *Applied Physics Letters*, **72** (3), pp. 338-340.
- [A. R. Denton, et al. 1991] Vegard's law, *Physical Review A*, **43** (6), pp. 3161-3164.
- [Y. Gao 1988] A new secondary ion mass spectrometry technique for III-V semiconductor compounds using the molecular ions CsM<sup>+</sup>, *Journal of Applied Physics*, **64** (7), pp. 3760-3762.
- [C. J. Gu, et al. 2006] SIMS quantification of matrix and impurity species in Al<sub>x</sub>Ga<sub>1-x</sub>N, *Applied Surface Science*, **252** (19), pp. 7228-7231.
- [Y. Homma, et al. 1991] Analyses of III-V compound semiconductors using secondary ion mass spectrometry, **40** (3), pp. 373-384.
- [Y. Homma, et al. 1992] Stability of Relative Sensitivity Factors in Secondary Ion Mass Spectrometry, *Journal of the Mass Spectrometry Society of Japan*, **40** (4), pp. 217-223.
- [M. J. P. Hopstaken, et al. 2010] Sputtering behavior and evolution of depth resolution upon low energy ion irradiation of GaAs, *Journal of Vacuum Science & Technology B: Microelectronics and Nanometer Structures*, **28** (6), pp. 1287.
- [C. Huyghebaert, et al. 2004] Energy and angular dependence of the sputter yield and ionization yield of Ge bombarded by O<sub>2</sub><sup>+</sup>, *Applied Surface Science*, **231-232**, pp. 693-697.
- [Y. Kudriavtsev, et al. 2013] Sputtering of the target surface by Cs<sup>+</sup> ions: Steady-state concentration of implanted cesium and emission of CsM<sup>+</sup> cluster ions, *Technical Physics*, **58** (5), pp. 735-743.
- [D. R. Lide, 2005] Handbook of Chemistry and Physics, CRC.
- [J. W. M. M. Nastasi, 2006] Ion Implantation and Synthesis of Materials (Springer -Verlag Berlin Heidelberg: Springer.
- [R.G. Wilson, et al. 1989] Secondary ion mass spectrometry A Practical Handbook for Depth Profiling and Bulk Impurity Analysis (USA: Wiley).
- [F. A. Stevie, et al. 2008] Quantification in dynamic SIMS: Current status and future needs, *Applied Surface Science*, **255** (4), pp. 1364-1367.
- [T.Wirtz, et al. 2001] Useful yields of MCs<sup>+</sup> and MCs<sub>2</sub><sup>+</sup> clusters: a comparative study between the Cameca IMS 4f and the Cation Mass Spectrometer, *International Journal of Mass Spectrometry*, **209** (1), pp. 57-67.
- [X. Tang, et al. 1989] Si-doping of MOCVD GaAs: Closer analysis of the incorporation process, *Journal of Crystal Growth*, **98** (4), pp. 827-837.
- [P. Van Der Heide, 2014] Secondary Ion Mass Spectrometry: John Wiley & Sons, Inc.) pp 44-143.
- [R. G. Wilson, 1995] SIMS quantification in Si, GaAs, and diamond *International Journal of Mass Spectrometry and Ion Processes*, **143** (0), pp. 43-49.

[R. G. Wilson, et al. 1989] Secondary ion mass spectrometry: a practical handbook for depth profiling and bulk impurity analysis, Wiley.

[H. Yamamoto, et al. 2013] RFS ratio of silicon in III-V compound semi-conductor measured with different offset voltage, *Surface and Interface Analysis*, **45** (1), pp. 417-429.

[J. F. Ziegler], [www.srim.org](http://www.srim.org), SRIM

## CHAPTER IV

### IV. Development of experimental protocols for chemical composition profiling of 3D architecture structures

This chapter is focused on the experimental protocols developed for chemical compositional analysis of InGaAs QWs in 3D architectures. In the first section, the development of the SIMS protocols to achieve high depth resolution profiles is discussed in detail. The impact of primary beam energy, incidence angle and orientation of the ion beam with respect to the trenches on the depth resolution is addressed. In the next two sections, the 3D reconstruction and depth profiling of single III-V trenches using ToF-SIMS and APT are discussed. Finally, the SIMS studies were compared with Auger and PL measurements on III-V trench using the averaging method.

#### IV.1 Recall of basic parameters of the investigated sample

The sample consists of InGaAs QWs of 8 to 10 nm in thickness with AlAs barrier layers of several nanometres in thickness grown selectively on non-planar Si substrates (100). III-V semiconductor compounds were grown using the selective aspect ratio trapping method (see Chapter II.1.3). 180-200 nm deep SiO<sub>2</sub> trenches aligned along the [110] direction with widths ranging from 100 nm to 300 nm were patterned on 300 mm Si (100). Figure IV-1 shows a cross-section STEM image of the III-V trenches, which contain the GaAs/AlAs/InGaAs/AlAs/GaAs/Si substrate stack. The growth conditions of III-V heterostructures are described in detail in Chapter II.1.4.3. At the bottom of the trench, many dislocations exist due to the high lattice mismatch between GaAs and Si. Some threading dislocations may propagate towards the surface but most of them are blocked in the SiO<sub>2</sub> walls leading to low defect density in the upper region. The good quality of the InGaAs (in thickness 8-10 nm) was confirmed by room temperature  $\mu$ PL measurements on the GaAs and on the InGaAs QW structures (discussed in Chapter IV.3.1).

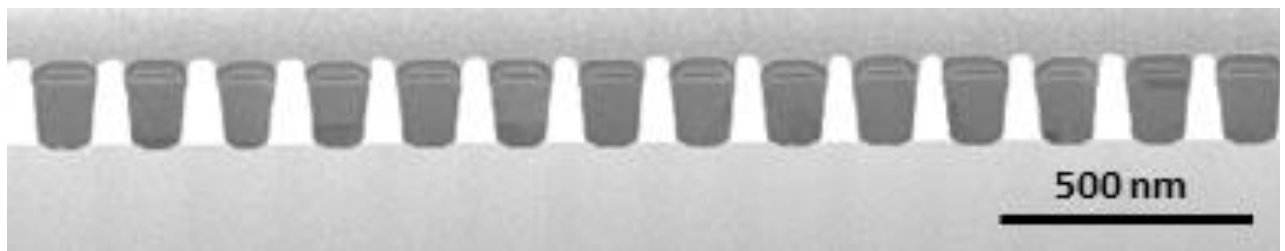


Figure IV-1 A cross-section STEM image of III-V heterostructures selectively grown in cavities on 300 mm Si wafers using the aspect ratio trapping method.

#### IV.2 An average approach using low energy magnetic SIMS

The abruptness of the InGaAs/AlAs QWs interfaces was investigated using Cameca SIMS-Ultra instrument (described in Chapter II.2.1.4). However, the lateral resolution of this instrument

(less than 1  $\mu\text{m}$ ) is not sufficient to resolve the individual trenches. Therefore, a profiling method that averages over several trenches was used to investigate the heteroepitaxial interfaces in each cavity. This method is based on the assumption that the structures are repetitive and thus, the signal from many adjacent trenches approaches the signal that would be obtained from one single trench.

An oxygen primary ion beam was used to achieve sufficiently high ion yield for III-group elements (In, Ga, Al). The sputtered area was limited by raster of  $200\text{ }\mu\text{m} \times 200\text{ }\mu\text{m}$  and a small field aperture of  $400\text{ }\mu\text{m}$  in diameter. The analyzed area was thus  $33\text{ }\mu\text{m}$  in diameter. Figure IV-1 shows a basic diagram for SIMS analysis of III-V trenches (around 100 to 120 trenches visible in the analyzed area). This method was applied in the previous chapter to study the Si doping in GaAs trenches under cesium bombardment. In the next sections, the experimental conditions used for accurate SIMS profiling of repetitive structures are discussed in detail.

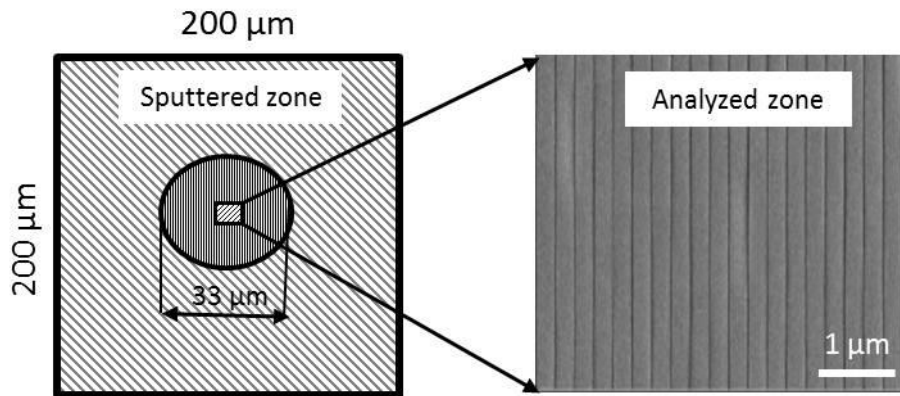


Figure IV-2 The basic principal of SIMS analysis of a repetitive III-V trench structures using an average approach.

### IV.2.1 SIMS conditions optimization in terms of sample topography and depth resolution under oxygen ion beam bombardment

#### IV.2.1.1 Effect of primary energy

The optimization of SIMS conditions is crucial if accurate studies of the quality of interfaces, segregation, diffusion and quantification in thin layers/structures are to be carried out. Furthermore, the analysis conditions should be adjusted accordingly to maximize the signal of interest and minimize artifacts. Whereas the true in-depth distribution of elements in the material (internal profile) can be modified as a result of the physical mechanisms involved during ion beam sputtering. As was mentioned in Chapter II.2, the energy deposited by primary ions leads to ion beam mixing processes, such as recoil mixing (interaction of primary ions with sample atoms), cascade mixing and radiation-enhanced diffusion [R.G. Wilson et al., 1989].

Basically, the depth resolution depends on the primary ion beam (type, energy, incident angle) and the substrate [Heide, 2014]. The collision cascade is responsible for the losses in depth resolution [Heide, 2014]. The depth resolution can be improved by decreasing the primary beam energy. The improved depth resolution by decreasing primary ion beam energy was reported for certain materials, e.g. Si with delta-doped layers [M. Juhel et al., 2006, B. Gautier et al., 1996] and SiGe [W. Vandervorst, 2008]. The depth resolution is often defined by decay length  $\Delta x$  per decade or by exponential decay length and both terms are used in this chapter. The exponential decay length  $\lambda$  can be calculated by the following equation:

$$\lambda = -\frac{(x_2 - x_1)}{\ln(I_{x2}) - \ln(I_{x1})} \quad (\text{Equation IV-1})$$

Where  $(x_2, x_1)$  and  $(I_{x2}, I_{x1})$  are respectively the depths and secondary ion intensities.

Figure IV-3 shows the SIMS depth profile of indium performed on a sample containing InGaAs QWs on non-planar Si substrates of 8-9 nm in thickness surrounded by AlAs barrier layers grown in cavities. The average profiling method that includes contributions from around one hundred III-V trenches under different oxygen primary ion beam impact energies was studied and shown in Figure II-3. A superposition of the different profiles and reduce the artifacts from depth calibration the mono-calibration (see Chapter II) (until AlAs/GaAs interface) was used. The thickness of III-V materials was estimated from cross-section STEM measurements. The experimental conditions can be found in Chapter II.1.4.3.

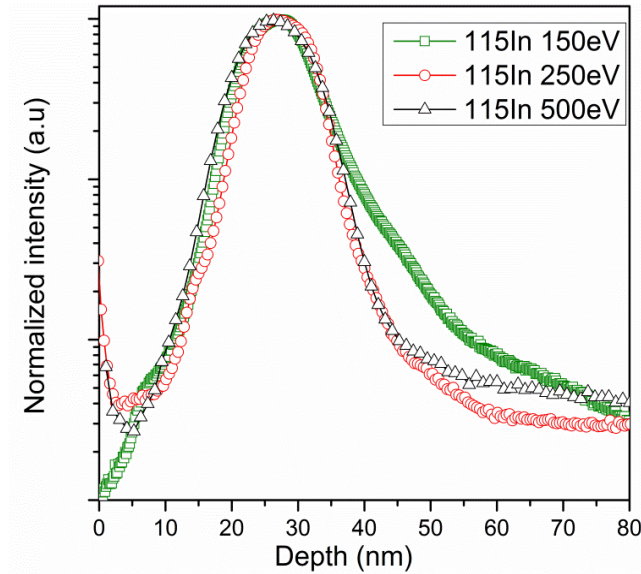


Figure IV-3 SIMS depth profiles of InGaAs QWs of 8-9 nm in thickness under low energy oxygen sputtering: a) 500 eV (black color), b) 250 eV (red color), c) 150 eV (green color).

## Chapter IV. Development of experimental protocols for chemical composition profiling of 3D architecture structures

The effects of primary energy on depth resolution of III-group elements were studied also on III-V sample grown on planar Si substrate. The reference sample containing the stack of GaAs/AlAs/InGaAs/AlAs/GaAs layers was studied with similar analysis conditions as those used for non-planar InGaAs layers. The III-V trenches were analyzed with the oxygen beam incident parallel to the trenches. The thickness of the InGaAs layer is 2 nm in thickness and the STEM image can be found in Appendix IV.A. The depth resolution calculations under low oxygen ion beam bombardment (less than 500 eV) for planar and non-planar InGaAs materials are given in Table IV-1.

**Table IV-1** Depth resolution of indium profile in InGaAs QWs on planar and non-planar Si substrates under the different energy of oxygen sputtering.

Primary energy, Ev	500 eV (41°)	250 eV (41°)	150 eV (52°)
Decay length upslope par decade	non-planar: 5.3 nm/dec. planar: 3.6 nm/dec.	non-planar: 5.1 nm/dec. -	non-planar: 5.8 nm/dec. planar: 3.3 nm/dec.
Decay length upslope, $\lambda_{\text{upslope}}$	non-planar: 3 nm planar: 2 nm	non-planar: 2.5 nm -	non-planar: 2.9 nm planar: 1.6 nm
Decay length downslope par decade	non-planar: 5.4 nm/dec. planar: 6 nm/dec.	non-planar: 5 nm/dec. -	non-planar: 12 nm/dec. planar: 5.6 nm/dec.
Decay length downslope, $\lambda_{\text{downslope}}$	non-planar: 2.8 nm planar: 3 nm	non-planar: 2.8 nm -	non-planar: 5.3 nm planar: 4 nm

The decay length upslope  $\lambda_{\text{upslope}}$  of indium profile (i.e MOCVD growth direction) in non-planar InGaAs is slightly higher than for planar InGaAs QW while the downslope decay is similar for both materials. The depth resolution of 5-6 nm/decade obtained for the indium profile in planar and non-planar InGaAs QW under 500 eV energy (41°) oxygen sputtering is similar to the reported results under the similar analysis conditions [M. J. P. Hopstaken et al., 2010].

The effect of the primary energy on the depth resolution in III-V materials is different to observations for boron doped layers in Si (see Appendix IV.B) and reported [M. Juhel et al., 2006]. The best depth resolution in Si material of 0.8 nm/decade is obtained at the lowest primary energy ( $E_p=150$  eV) compared to InGaAs, where depth resolution degradation is observed. It can be related to the roughness formation on the material and is discussed in the next section.

### IV.2.1.2 Effect of orientation of the ion beam with respect to the trenches

A sample containing III-V trenches of 300 nm in width on non-planar Si substrates samples were analyzed using both parallel and perpendicular orientations of the oxygen ion beam with respect

## Chapter IV. Development of experimental protocols for chemical composition profiling of 3D architecture structures

to the trenches. The primary impact energy of 500 eV with an incident angle of  $42^\circ$  was used during the experiments. SIMS depth profiles of relevant elements (Al, Ga, In and Si) are presented in Figure IV-4 a), b) for each orientation. In the SIMS depth profile shown in Figure IV-4 a), b) the  $^{69}\text{Ga}^+$  profile is well defined at the AlAs/InGaAs and InGaAs/AlAs interfaces. The downslope of the  $^{69}\text{Ga}^+$  signal at the first GaAs/AlAs interface is twice as steep as that at the InGaAs/AlAs interface. It can be explained by the high abruptness and quality of heteroepitaxial layers using aspect ratio (AR) method during epitaxy in comparison to direct epitaxy on planar Si wafers where the defect concentration is higher (Figure II-5) (see Chapter II).

The upslope of indium profiles in parallel and perpendicular directions is similar (3.5 nm/decade). However, a better depth resolution of downslope of indium in a parallel orientation (6 nm/decade) compared to the perpendicular direction (7.7 nm/decade) is observed. When the  $\text{O}_2^+$  ion beam is incident perpendicular to the trenches the sputtering behavior may be modified due to shadowing (see Figure IV-5), whilst the sputtering behavior of the ion beam aligned parallel to the trenches should minimize shadowing effects.

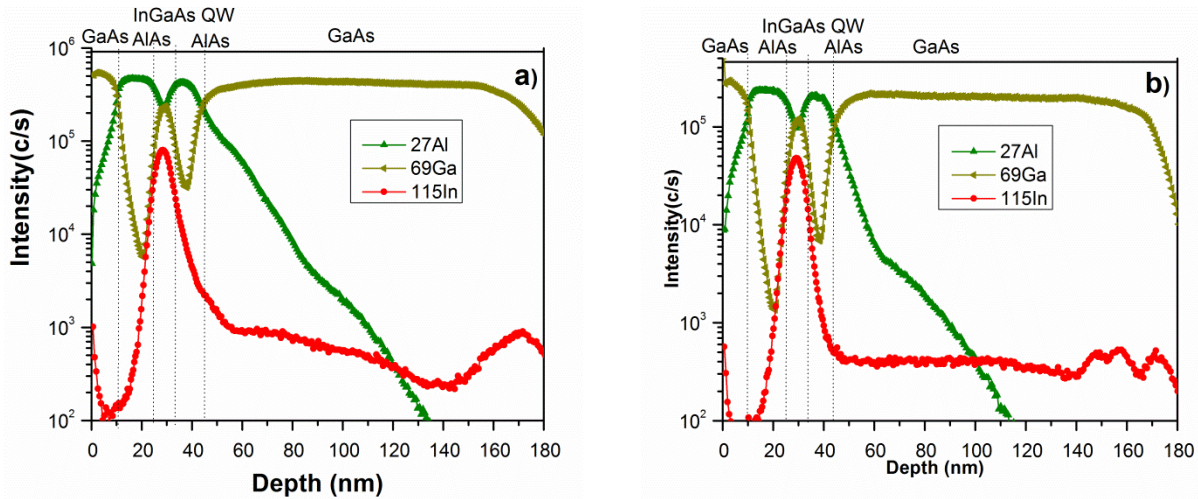


Figure IV-4 SIMS depth profiles of III-V heteroepitaxial interfaces under a) perpendicular and b) parallel direction with respect to the trenches using 500 eV ( $42^\circ$ ) oxygen sputtering.

The better depth resolution for the parallel orientation can be seen also by the presence of two peaks of indium at the substrate interface due to the step (see Figure IV-7) on the substrate surface that is not distinguished in the perpendicular orientation (Figure IV-4 a, b). These peaks can be explained by contamination of indium at the GaAs/Si interface (see Figure IV-4).

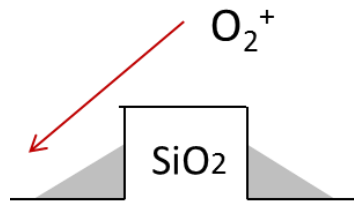


Figure IV-5 Illustration of the shadowing effect when the ion beam is in perpendicular orientation to the III-V trenches using magnetic SIMS

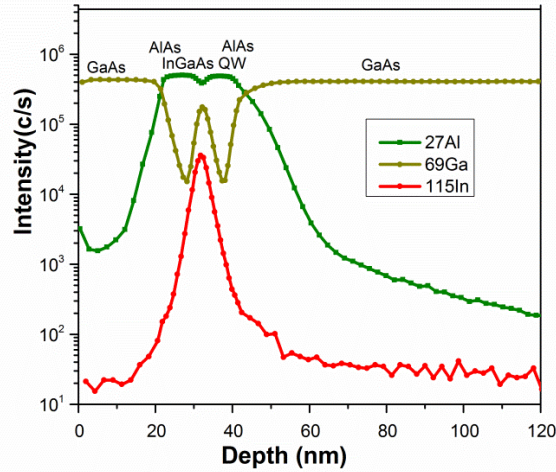


Figure IV-6 SIMS depth profiles of InGaAs/AlAs QW of 2 nm in thickness on planar Si substrate under 500 eV oxygen sputtering.

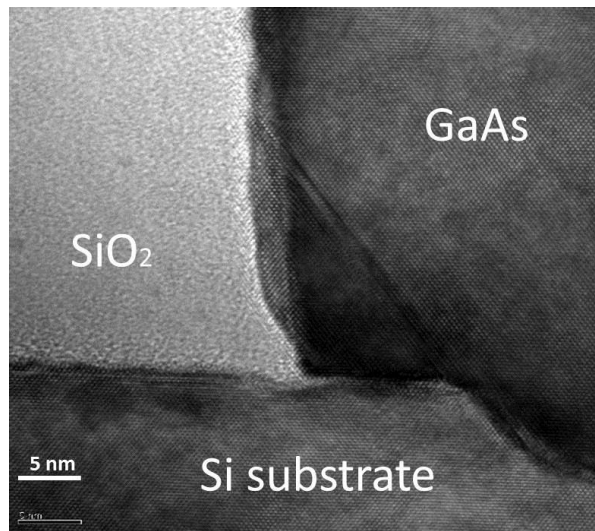


Figure IV-7 A cross-section STEM image of GaAs/Si interfaces grown in cavities on 300 mm Si wafers.

Worse depth resolution with respect to the orientation of the ion beam to the trenches inside SiO<sub>2</sub> can be also explained by the formation of topography under oxygen sputtering. In order to gain more insight about the effect of oblique O<sub>2</sub><sup>+</sup> ion beam irradiation on the surface morphology, AFM measurements were performed after different O<sub>2</sub><sup>+</sup> sputtering times for the two configurations of the incident beam: parallel and perpendicular. Figure IV-8 shows an AFM image of the initial topography of the III-V trenches. The formation of roughness at the InGaAs/AlAs interface at an approximate depth of 40 nm under O<sub>2</sub><sup>+</sup> sputtering for parallel and perpendicular ion beam orientations with respect to the trenches is shown in the AFM images in Figure IV-9 and Figure IV-10, respectively.

The formation of periodic surface ripples which develop perpendicular to the incident beam is a result of oxygen beam irradiation of III-V materials. Note that the precise mechanism of ripple formation is still unknown. The wavelength of these periodic ripples are of the order of 24 nm

## Chapter IV. Development of experimental protocols for chemical composition profiling of 3D architecture structures

for both ion beam orientations but the surface roughness for the perpendicular orientation (RMS=2.9 nm) is much higher than that for parallel one (RMS=1.7 nm). The main change in topography occurs at the junction between III-V materials and SiO<sub>2</sub> walls where the surface morphology is much more affected when the O<sub>2</sub> beam is incident perpendicular to the trenches. As can be seen in Figure IV-10, a large ripple can be seen close to the SiO<sub>2</sub> wall (see Figure IV-10) due, most certainly, to the shadowing effect in the perpendicular orientation. Similar observations were observed and confirmed by a lower impact energy of 250 eV of oxygen sputtering in the parallel and perpendicular directions and are given in Figure IV-11 and Figure IV-12. The strong impact of primary ion beam energy on the surface topography formation can be seen from Table IV-2. Higher surface topography is formed when lowering the impact energy below 500 eV. This explains the results discussed in the previous section that the lowering the beam energy below 500 eV actually deteriorates depth resolution.

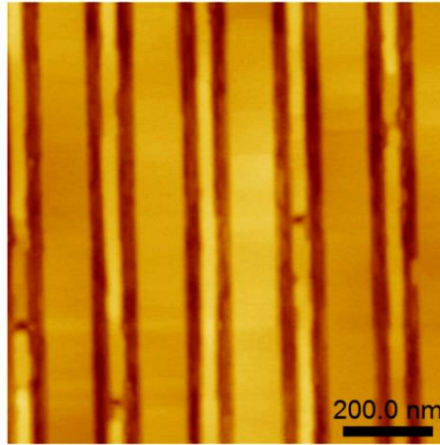


Figure IV-8 AFM image of the initial topography of III-V trenches selectively grown in SiO<sub>2</sub> cavities on Si substrates, where  $-17.8 \text{ nm} < z < 14 \text{ nm}$ .

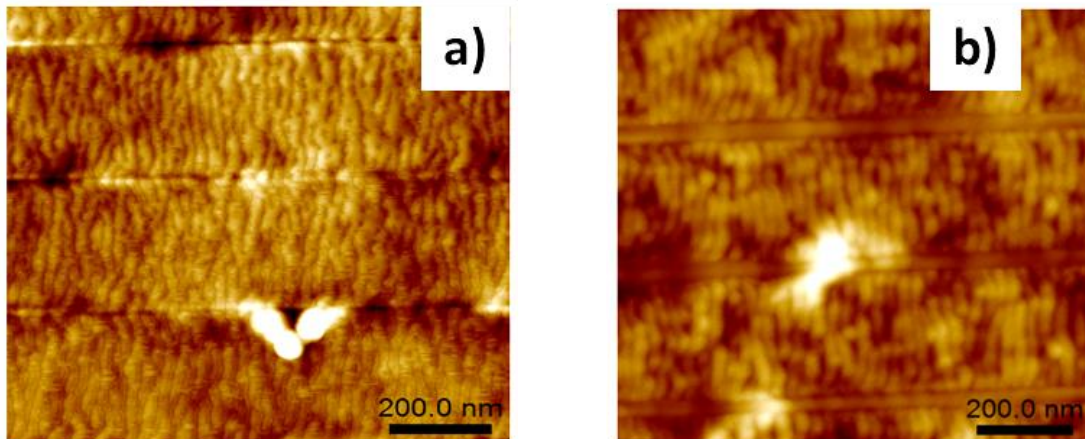


Figure IV-9 AFM image of topography formation at a) InGaAs/AlAs (33 nm) interfaces and b) et GaAs/Si interfaces under oxygen sputtering with energy 500 eV in a parallel direction to the trenches, where  $-12.3 \text{ nm} < z < 12.4 \text{ nm}$ .

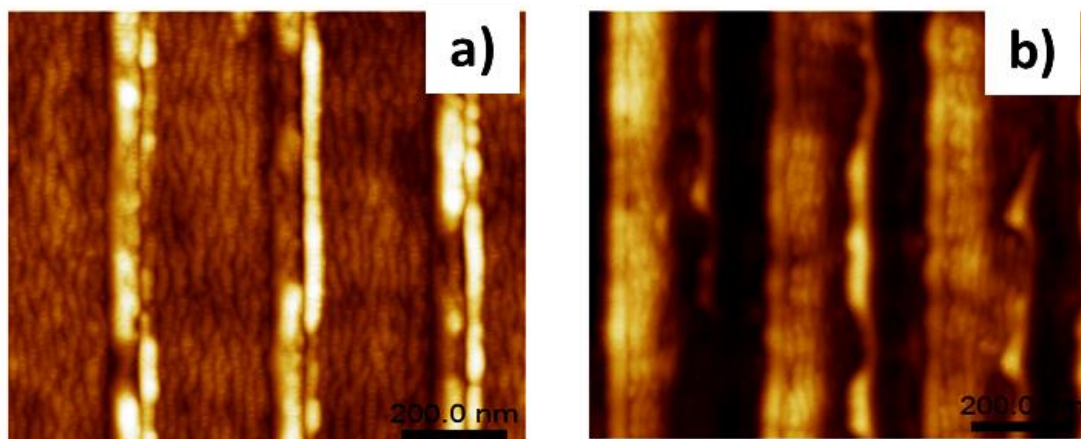


Figure IV-10 AFM image of topography formation at a) InGaAs/AlAs (33 nm), where  $-13.2 \text{ nm} < z < 10.7 \text{ nm}$  and b) GaAs/Si (180nm) interfaces under oxygen bombardment with energy 500 eV in perpendicular orientation in respect to the trenches, where  $-12 \text{ nm} < z < 15.7 \text{ nm}$ .

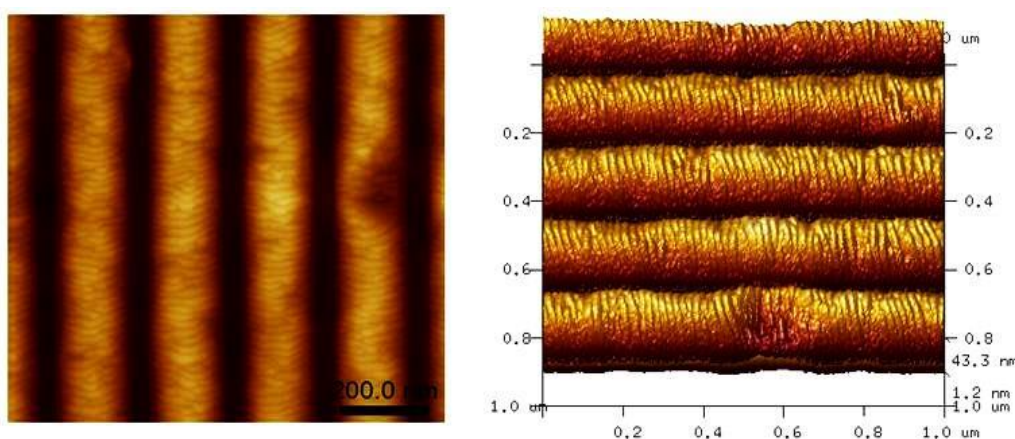


Figure IV-11 AFM images of topography formation on III-V trenches in 150-180 nm width under oxygen bombardment with energy 250 eV  $\text{O}_2^+$  in parallel direction respect to the trenches, where  $-41 \text{ nm} < z < 43.3 \text{ nm}$ .

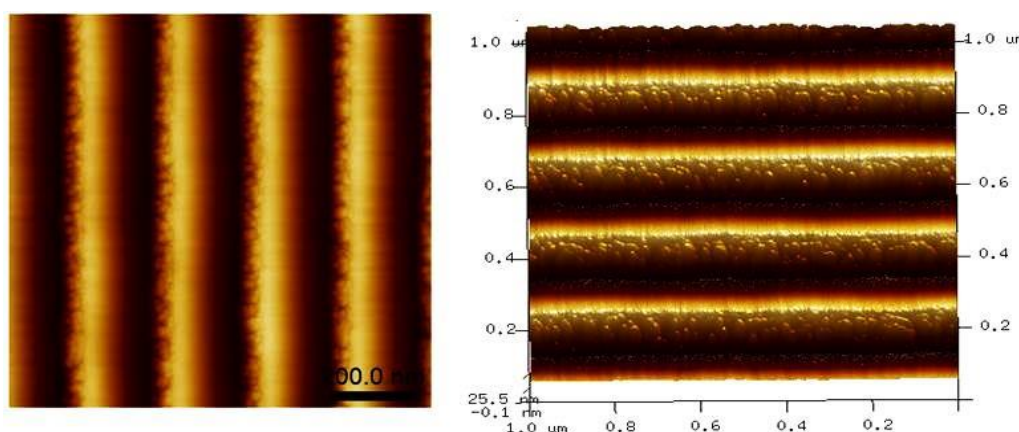


Figure IV-12 AFM images of topography formation on III-V trenches 250 nm width under 250 eV oxygen bombardment in a perpendicular orientation, where  $25.7 \text{ nm} < z < 25.5 \text{ nm}$ .

**Table IV-2** Roughness measurements on single trench under parallel and perpendicular orientation oxygen bombardment with respect to the III-V trenches

Energy of sputtering	Initial topography (nm)	Roughness in parallel orientation (nm)	Roughness in a perpendicular orientation (nm)
500 eV	0.5	0.9	1.2
250 eV	0.5	4.3	5.4

### IV.2.1.3 Effect of incidence angle

The incident angle of the primary ion beam is an important parameter to achieve an accurate depth profiling as well as energy and orientation of ion beam. Depth resolution evolution of indium in InGaAs QWs on planar Si substrates under different angles  $\theta$  and primary energies  $500\text{eV} < E < 1\text{ keV}$  of oxygen sputtering was reported [M. J. P. Hopstaken et al., 2010]. The best depth resolution for III-V materials was demonstrated for impact angles ( $45^\circ$ - $60^\circ$ ) using the quadrupole SIMS instrument Atomika 45000. However, in Cameca SC-Ultra instrument the variation of incident angle ( $>3$ - $5^\circ$ ) is limited by the variation of sample voltage and, therefore, requires different beam alignments for each angle.

The extreme low primary energy of 250 eV oxygen ion beam sputtering with an incident angle of  $50^\circ$  was used to study III-V trenches. In order to perform the experiments with a single beam alignment, a metallic stand was used to tilt the sample at  $12^\circ$  to increase the impact angle. Figure IV-13 shows the comparison of chemical profiles of non-planar InGaAs/AlAs QWs with ( $62^\circ$ ) and without sample tilting ( $50^\circ$ ). Note the monocalibration was applied to study the depth resolution.

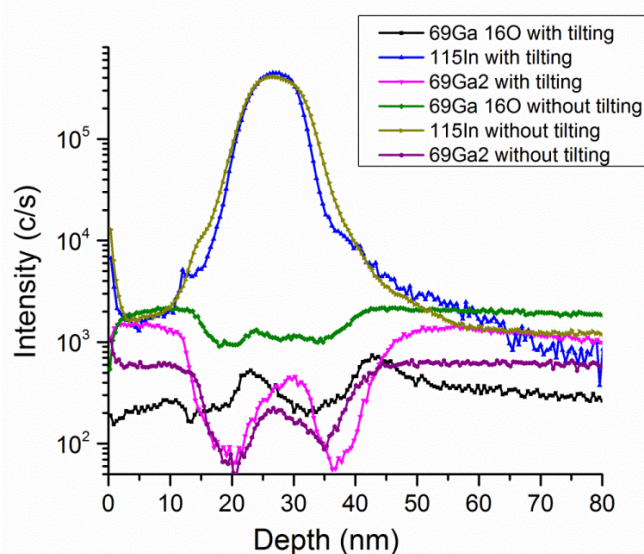


Figure IV-13 SIMS depth profiles of InGaAs/AlAs QWs on non-planar Si using 250 eV oxygen sputtering with ( $62^\circ$ ) and without sample tilting ( $50^\circ$ ).

## Chapter IV. Development of experimental protocols for chemical composition profiling of 3D architecture structures

Figure IV-14 shows the superposition of the indium profiles obtained with and without sample tilting. The improvement of depth resolution at the InGaAs/AlAs (downslope) interface using the simple tilting of more than 1 nm/decade is observed. The AFM images of topography formation under sample tilting and after oxygen sputtering at 40-50 nm in depth are shown in Figure IV-15. It can be seen that ripples form. Contrary, to topography formation on non-tilted sample (see Figure IV-11) the improvement of depth resolution can be explained by the longer time of ripples formation on the surface. However, the experiments performed on the boron delta-doping layers in Si materials(reference sample) have shown the different effect on depth resolution profiling using sample tilting. For Si, significant degradation in depth resolution is observed contrary to InGaAs using sample tilting. It was previously[Juhel et al, 2016] shown that a primary  $O_2^+$  beam at the  $45^\circ$  incidence angle to offer the best depth resolution, minimizing the ripple formation during sputtering of Si. (see Appendix IV.C). The sputter rate measurements for Si and InGaAs are given in Table IV-3. For III-V materials, the increase in sputter rate by more than twice using sample tilting was also observed. We assume that the difference in sputter rate is related to oxygen incorporation and the increased ripple amplitude on the III-V surface as observed by AFM. Note that sputter rate was estimated by using monocalibration in depth.

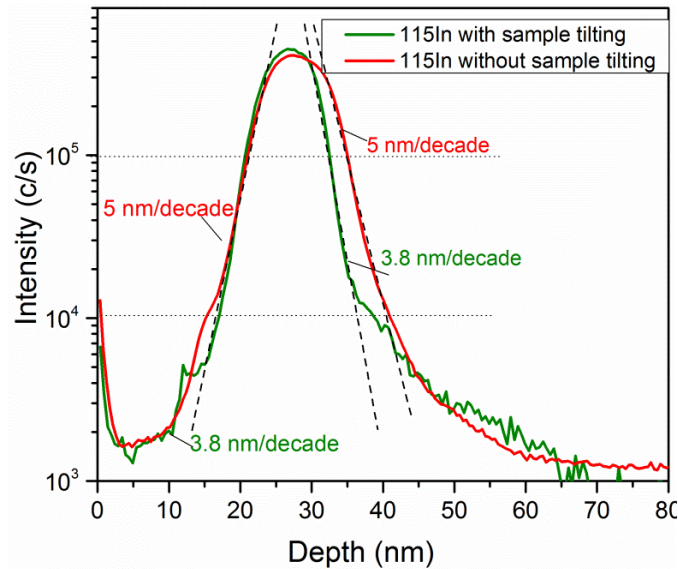


Figure IV-14 SIMS depth profiles of InGaAs/AlAs QWs on non-planar Si using 250 eV oxygen sputtering with (incident angle of  $50^\circ$ ) and without sample tilting (incident angle of  $62^\circ$ ) with parallel direction to the trenches

**Table IV-3** Sputter rate measurements for III-V materials using sample tilting under 250 eV

SR <sub>III-V</sub> 250 eV with sample tilting	SR <sub>III-V</sub> 250 eV without sample tilting
0.04 nm/s	0.02 nm/s

The disadvantage of using sample tilting is that practically it is difficult to optimize due the variation of z-height across the tilted direction in Cameca SIMS-Ultra instrument.

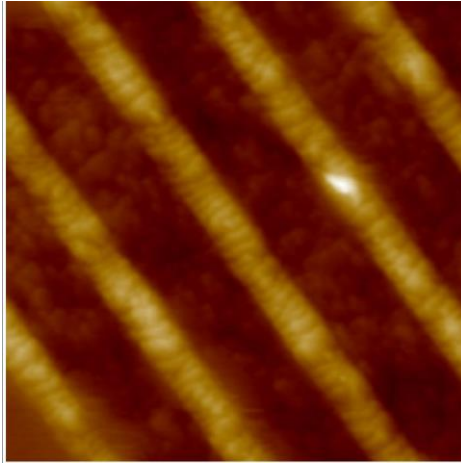


Figure IV-15 AFM image of topography formation on III-V trenches under 250 eV oxygen sputtering in parallel direction and using sample tilting, where  $-27.3 < z < 28.8$  nm and zone dimensions of 810.5 nm

#### IV.2.1.4 Effect of sample rotation

The different macro topography formation on the surface under ion beam bombardment was observed, such as ripples, cones, pyramids, and terraces etc. The formation of ripples and changes of ion yield under oxygen sputtering has been observed for GaAs, GaSb and InAs materials [Y. Nakagawa et al., 1992]. However, these effects weren't observed for GaP material under oxygen ion beam bombardment with the energy of 10.5 keV and the incidence angle of  $37^\circ$  [Y. Nakagawa et al., 1992, A. Karen et al., 1993]. The theoretical explanation based on the Sigmund model of height modulations on the surface of amorphous solids was proposed by Bradley and Harper [R. M. Bradley et al., 1988]. This model assumes that the surface self-diffusion is thermal dependent. In this model, the wavelength of ripples has expressed a function of the activation energy of the surface self-diffusion  $\Delta E$  and temperature and can be found in reference [P. Sigmund, 1973]. Unfortunately, the theoretical model wasn't confirmed by experimental observations for  $\text{Al}_{0.2}\text{Ga}_{0.8}\text{As}$  material [K. Elst et al., 1997]. The absence of temperature dependence on the ripple wavelength and the absence of diffusion mechanism were reported [K. Elst et al., 1997]. Thus, the mechanism of ripple formation remains unclear.

The rotation of the sample or Zalar rotation (term used in Auger technique) is an effective method to improve the depth resolution profiling by smoothing the surface during ion beam sputtering [R. M. Bradley et al., 1996]. Sample rotation is not mechanically available in the magnetic SIMS Cameca SC-Ultra instrument and thus, for these experiments the ToF-SIMS V instrument was used. The description of the ToF-SIMS technique can be found in Chapter II.2.1.1. The impact angle of  $45^\circ$  for both dual beams (analysis and sputtering) is close to the impact angle (of  $41^\circ$ ) used in the experiments performed on the SC-Ultra described above. Figure II-15 shows the ToF-SIMS comparison of InGaAs QWs grown on patterned Si wafers under oxygen irradiation with and without sample rotation. The III-V trenches were aligned parallel to the oxygen beam during the experiments without sample rotation. Higher depth

## Chapter IV. Development of experimental protocols for chemical composition profiling of 3D architecture structures

resolution (6 nm/decade) using sample rotation compared to results obtained without sample rotation (7.5 nm/decade) is observed. The artifact of sputtering and tailing effect on the indium profile using sample rotation can be seen in Figure IV-16, the appearance of a bump at 550 s sputter time. To better understand the improvement with and without sample rotation (in parallel orientation) and artifact of sputtering at approximately 40 nm in depth, AFM measurements were performed (Figure IV-17 a, b, c). Figure IV-16 c shows that using sample rotation leads to a smooth and flat surface on III-V materials compared to without rotation (parallel orientation) where the surface of the III-V materials roughens. (Table IV-4). However, the bumps observed at the III-V/SiO<sub>2</sub> interface are similar to those using the perpendicular orientation to the trenches (see Figure IV-4). It seems that using sample rotation, although it reduces roughness on the III-V materials, it brings the sample into the non-preferable orientation of the ion beam for most of the depth profile, which leads to a shadowing effect during oxygen sputtering. Note that, in this case, the shadowing effect can be seen on both sides of the trench.

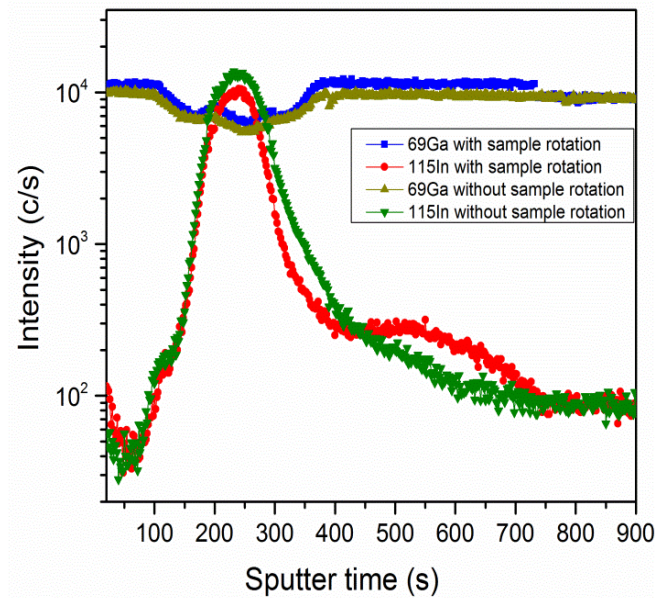


Figure IV-16 ToF-SIMS profile of InGaAs QWs arrays grown on patterned Si substrates under oxygen irradiation (dose= $4.8 \cdot 10^{14}$  ions) at 500 eV energy and analysis beam  $\text{Bi}_5^{++}$  and energy of 60 keV (dose= $6.8 \cdot 10^8$  ions) with and without sample rotation

Table IV-4 Topography formation on III-V materials on patterned Si wafers under oxygen bombardment using ToF-SIMS.

	Initial topography	Under $\text{O}_2^+$ 500 eV sputtering and $\text{Bi}_5^{++}$ in parallel orientation to the trenches	Under $\text{O}_2^+$ 500 eV sputtering and $\text{Bi}_5^{++}$ and under sample rotation
RMS, one trench, nm	0.6	0.9	0.5

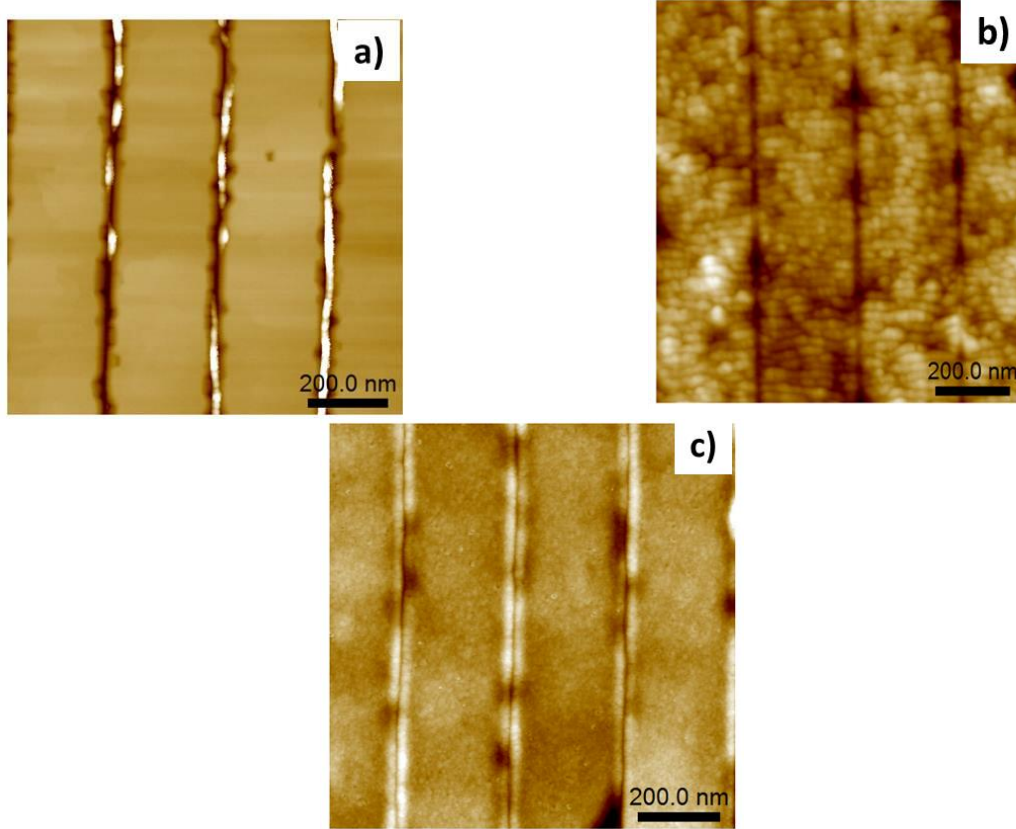


Figure IV-17 AFM image of III-V trenches, where a) initial topography, where  $-28.7 \text{ nm} < z < 11.4 \text{ nm}$  b) in parallel orientation to the trenches and under oxygen sputtering of 500 eV and  $\text{Bi}_5^{++}$  and energy of 60 keV, where  $-9 \text{ nm} < z < 5.5 \text{ nm}$ , c) under sample rotation and oxygen sputtering of 500 eV and  $\text{Bi}_5^{++}$ , where  $-8.7 \text{ nm} < z < 3.8 \text{ nm}$ .

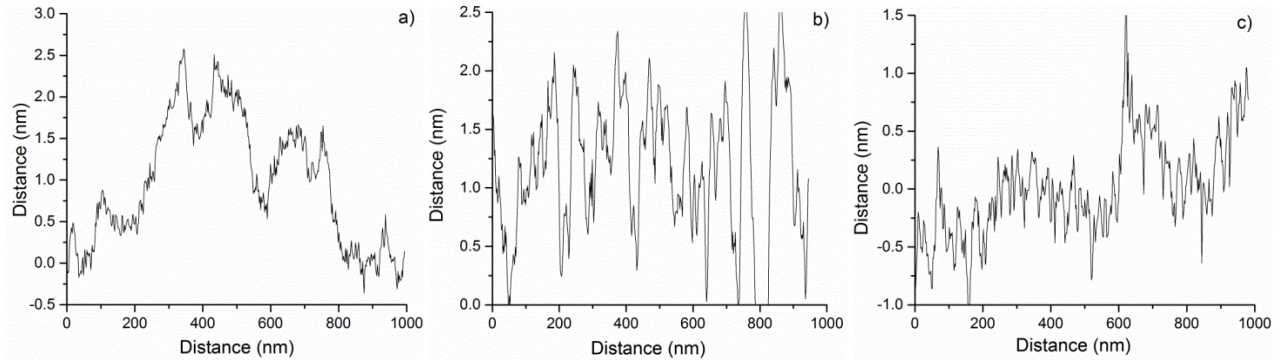


Figure IV-18 Profiles along the III-V trenches presented in Figure IV-16, where a) initial topography b) under oxygen sputtering of 500 eV and  $\text{Bi}_5^{++}$ , c) under sample rotation.

The impact of the bismuth source on the depth resolution under sample rotation was studied also using planar reference sample containing InGaAs QW of 2 nm in thickness described above (see Appendix IV.A). Figure IV-19 shows the ToF-SIMS profile of the InGaAs/AlAs QW with and without sample rotation under 250 eV  $\text{O}_2^+$  ion beam bombardment and with 60 keV  $\text{Bi}_3^{++}$  primary ion beam. However, the significant improvement of the surface topography under oxygen and bismuth irradiation using sample rotation wasn't observed. This is probably related to the high initial topography of the III-V surface due to lattice mismatch of III-V materials and

## Chapter IV. Development of experimental protocols for chemical composition profiling of 3D architecture structures

Si (see Chapter II.1.4.1). The presence of defects like APBs on the surface can be seen from AFM measurements (see Figure IV-20). Moreover, the topography observations in the center of the crater are demonstrated that bismuth incorporation leads to the formation of higher roughness on the surface (see Figure IV-21 and Figure IV-22). The preservation of the initial surface topography is observed as well for experiments performed under oxygen sputtering. Furthermore, Figure IV-23 shows the presence APBs even under sample rotation. Roughness measurements using AFM measurements are summarized in Table IV-5.

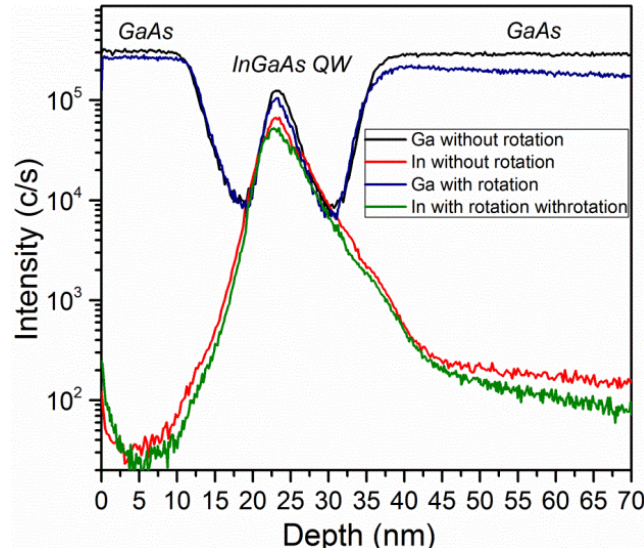


Figure IV-19 ToF-SIMS profile of a sample containing InGaAs/AlAs QW of 2 nm with and without sample rotation under  $O_2^+$  ion beam bombardment with energy of 250 eV (dose= $1.05 \cdot 10^{15}$  ions) and with  $Bi_3^{++}$  primary ion beam and energy of 30 keV (Dose:  $5,61 \cdot 10^8$  ions).

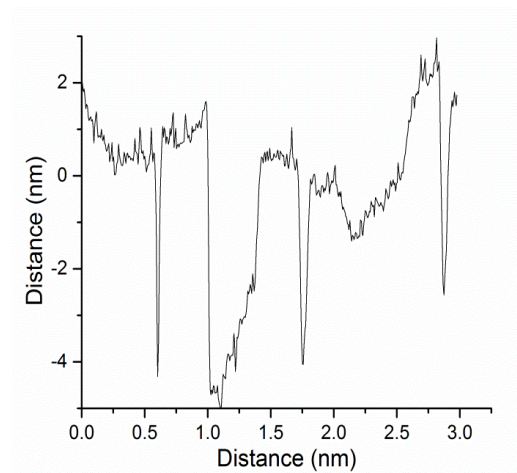


Figure IV-20 Initial topography of III-V heterostructures grown on planar Si wafers, -, nm, scanning zone  $3.3 \mu m \times 3.3 \mu m$ , where  $14.8 nm < z < 7.8 nm$ .

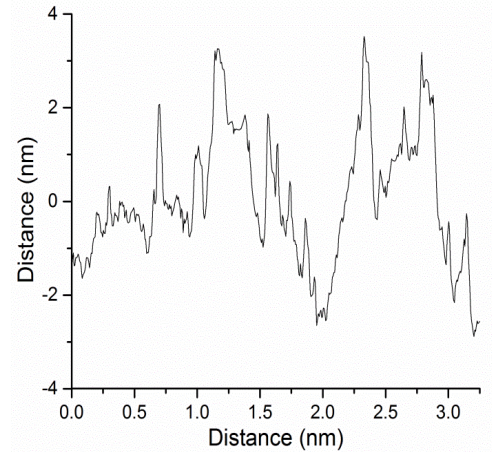
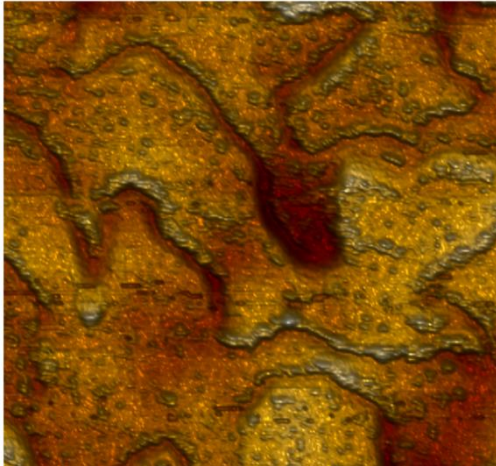


Figure IV-21 AFM image of topography formation on III-V materials without sample rotation under  $O_2^+$  sputtering (250 eV) with scanning zone  $3.3 \mu m \times 3.3 \mu m$ , where  $-10.2 \text{ nm} < z < 7.5 \text{ nm}$ .

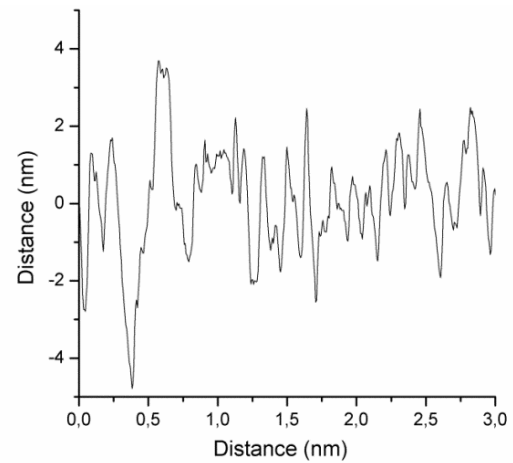
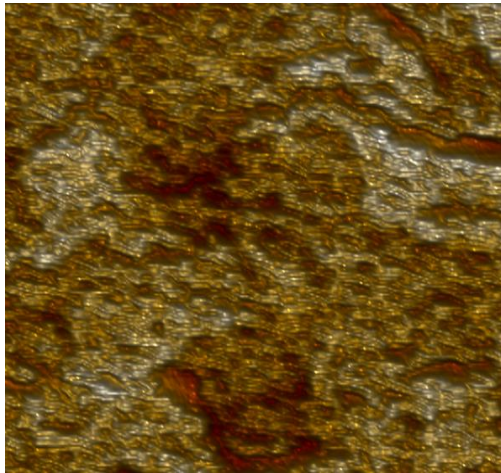


Figure IV-22 AFM image of topography formation on III-V materials without sample rotation under  $O_2^+$  sputtering (250 eV) and  $Bi_3^{++}$  with scanning zone  $3.3 \mu m \times 3.3 \mu m$ , where  $-12.1 \text{ nm} < z < 6.4 \text{ nm}$ .

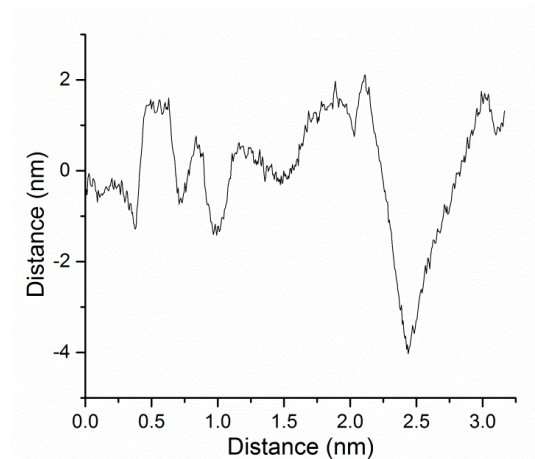
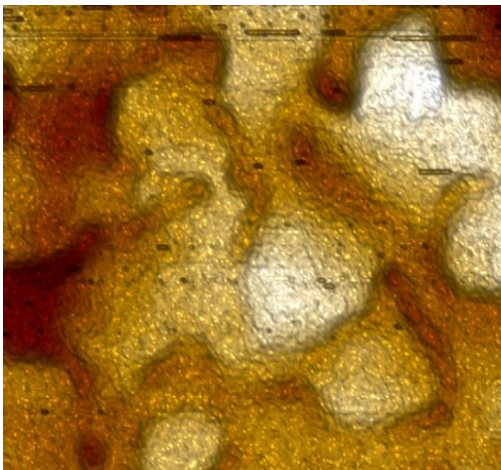


Figure IV-23 AFM image of topography formation on III-V materials under sample rotation with scanning zone  $3.3 \mu m \times 3.3 \mu m$ , where  $8.5 \text{ nm} < z < 5 \text{ nm}$ .

## Chapter IV. Development of experimental protocols for chemical composition profiling of 3D architecture structures

**Table IV-5** Topography formation on III-V materials on planar Si under oxygen bombardment with and without sample rotation using ToF-SIMS

	Initial topography	Under 250 eV $O_2^+$ sputtering and $Bi_3^{++}$	Under 250 eV $O_2^+$ sputtering and without $Bi_3^{++}$	Under sample rotation
RMS (9.32 $\mu m$ x 9.19 $\mu m$ )	1	2	1.5	1.4
RMS (292.97 nm x 315.5 nm)	0.3	0.8	0.4	0.2

The topography formation of bulk GaAs material was studied also under low energy cesium bombardment (250 eV) and using a 60 keV  $Bi_3^{++}$  analysis beam by ToF-SIMS. During these experiments, the formation of “bumps” “in labyrinth structure” of GaAs surface under cesium irradiation is observed. Figure IV-24 shows the initial topography of GaAs material. From Figure IV-27 can be seen that that small “bumps” formation are retained using cesium irradiation. In contrast, to oxygen irradiation of III-V materials, the “bumps” are promoted under cesium irradiation using sample rotation (Figure IV-27). The use of bismuth leads to higher topography formation (Figure IV-26). However, the roughness is significantly higher under cesium irradiation with sample rotation than without, thus will impact on the depth resolution (Table IV-6). It can be explained by the higher reactivity of cesium primary ions on III-V materials than oxygen. This mechanism of formation of “bumps” under cesium irradiation requires further investigations. Thus, due to the high roughness formation, the experiments using cesium sputtering at low impact energy are not suitable for high depth profiling of III-V materials.

**Table IV-6** Roughness measurements of GaAs material under cesium (250 eV) and bismuth irradiation using ToF-SIMS

	Initial topography	Under $Cs^+$ sputtering and $Bi_3^{++}$	Under $Cs^+$ sputtering and without $Bi_3^{++}$	Under sample rotation
RMS, nm	1.4	3.7	3.4	20.3

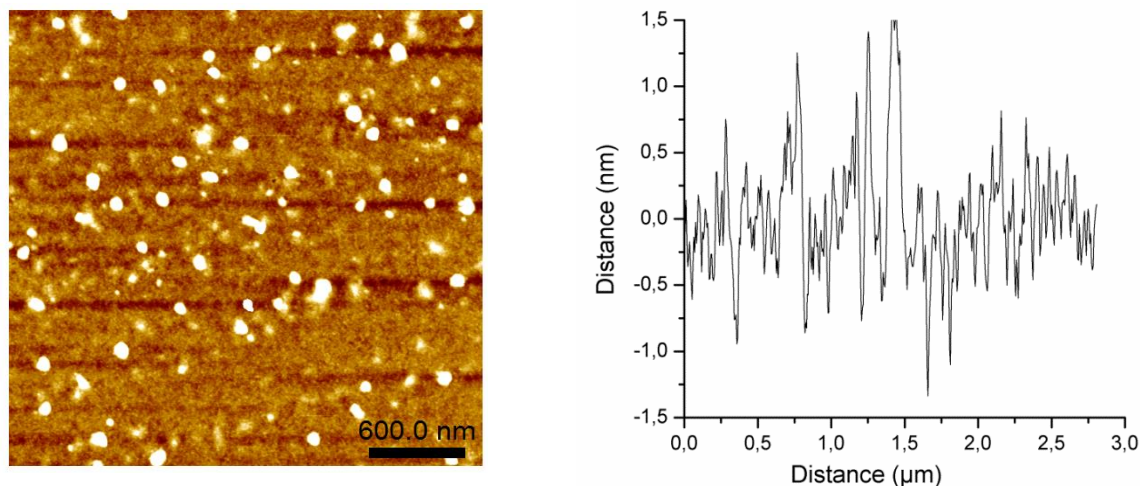


Figure IV-24 Initial topography of GaAs material, where  $4.7 \text{ nm} < z < 3.5 \text{ nm}$ .

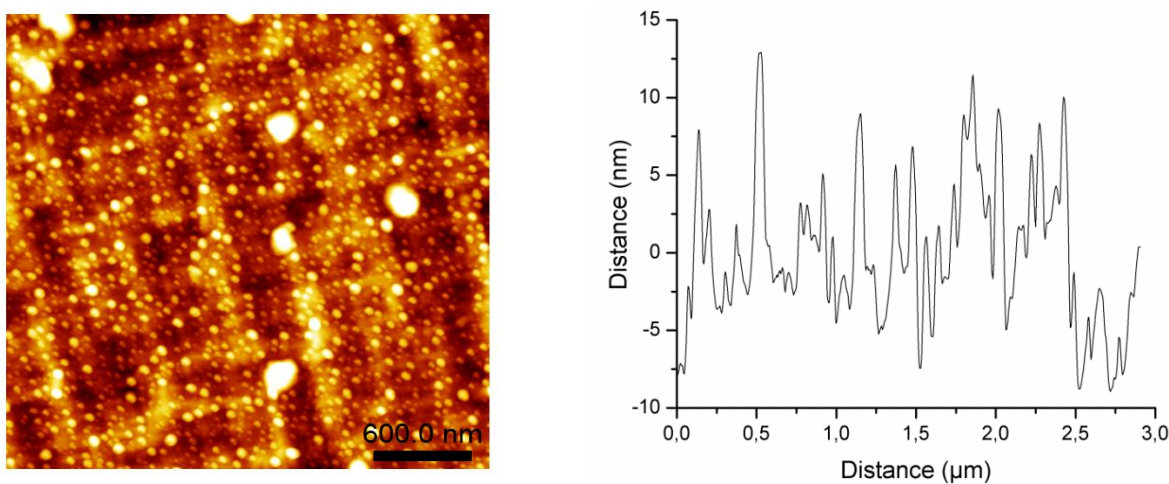


Figure IV-25 AFM image of GaAs topography under  $\text{Cs}^+$  sputtering and  $\text{B}_3^{++}$  analysis ion beams without sample rotation, where  $-27.5 \text{ nm} < z < 24.1 \text{ nm}$ .

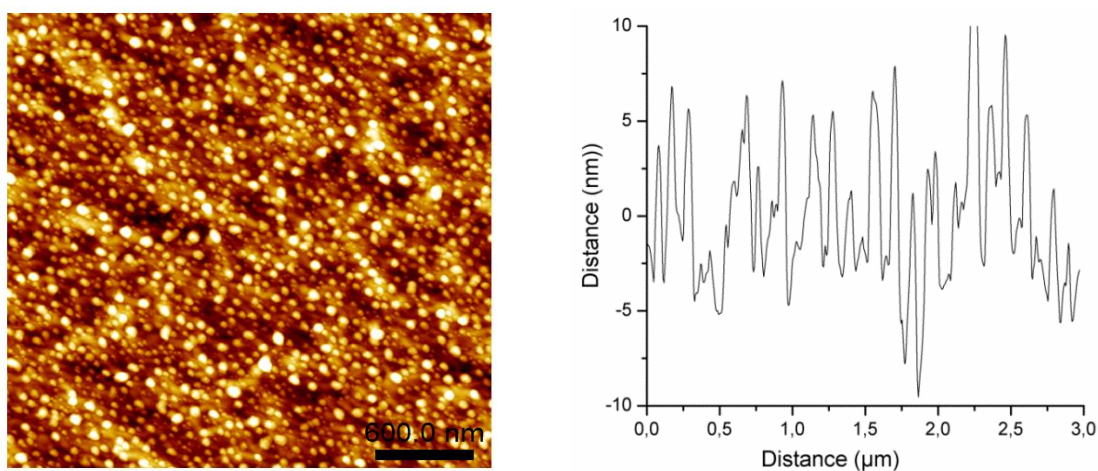


Figure IV-26 AFM image of GaAs topography under sample rotation under  $\text{Cs}^+$  sputtering without  $\text{Bi}_3$ , where  $-13.1 < z < 11.6$ .

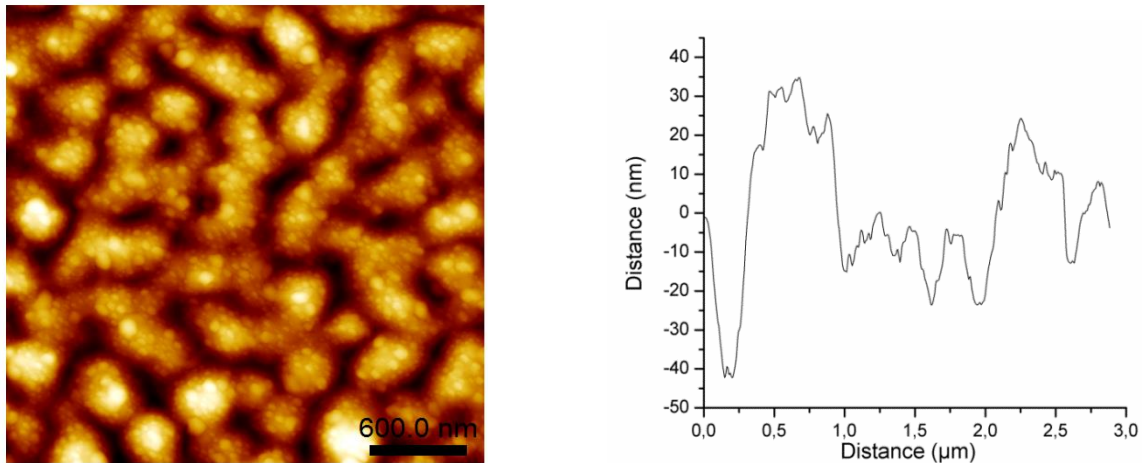


Figure IV-27 AFM image of GaAs topography under sample rotation at the center of the crater, where  $-73.5 \text{ nm} < z < 73.5 \text{ nm}$ .

### IV.3 3D reconstruction of a single III-V trench using ToF-SIMS and atom probe tomography

The use of techniques with higher lateral and depth resolution than SIMS allows the pertinence of magnetic SIMS profiles that are averaged over several trenches to be confirmed. To achieve this, we have used ToF-SIMS and 3D atom probe tomography. These techniques are powerful analytical tools for nanoscale characterization of advanced materials and allow localized information of species in a 3D volume to be obtained. Additionally, ToF-SIMS and APT can be well correlated although the basic principle of extraction of atoms from the sample is different while the time-of-flight spectroscopy is used for collection of atoms in both techniques. In APT, a laser pulse is used to create of atoms in the form of ions, albeit in ToF-SIMS and SIMS the atoms are sputtered from the surface of the material using an ion beam.

Dual beam TOF-SIMS was used to analyze patterned III-V heterostructures with a lateral resolution sufficient to resolve the individual trenches and obtain a 3D reconstruction of several InGaAs QWs. The III-V patterned structures have been observed by TOF-SIMS with 500 eV  $\text{O}_2^+$  sputtering source and 60 keV  $\text{Bi}_3^{++}$  analysis with a small area of analysis of  $5 \mu\text{m} \times 5 \mu\text{m}$  corresponding to a pixel size of 19.5 nm/pixel. The III-V trenches in 180-200 nm in width were orientated in parallel orientation to the incidence direction of the  $\text{O}_2^+$  ion beam.

A high lateral resolution of the  $\text{Bi}_3^{++}$  analysis beam (estimated at  $<100 \text{ nm}$  in this case) allows the individual  $\text{SiO}_2$  trenches to be resolved with sufficient lateral resolution. The obtained  $\text{Si}^+$  secondary ion image corresponding to the periodicity of the  $\text{SiO}_2$  trenches is presented in Figure IV-28.

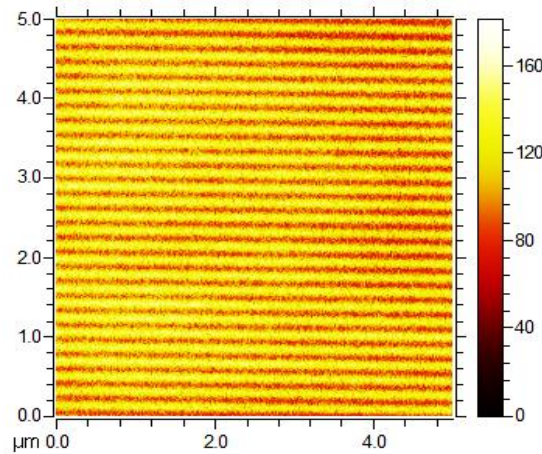


Figure IV-28 The ToF-SIMS Si secondary ion image coming from arrays of III-V heterostructures and SiO<sub>2</sub> barrier layers using a scanning resolution of 256 x 256 pixels. Where the Si secondary ion image is more intense (lighter color) this corresponds to the SiO<sub>2</sub> barrier layers.

The 3D reconstruction of III-V heterostructures with the field of view of 5  $\mu\text{m} \times 5 \mu\text{m}$  is presented in Figure IV-29 a, b. Each of the layers composing this 3D stacking can be spatially distinguished and identified. There is a good correspondence between 3D images and the cross-sectional STEM image shown in Figure IV-36 b.

The Si contribution from the SiO<sub>2</sub> walls has been excluded from the reconstruction using a region of interest (ROI). It allows the quantification of one individual patterned III-V heterostructures trench in between SiO<sub>2</sub> wall to be obtained. Figure IV-29 c shows the 3D volume of an individual III-V trench of 3074 nm x 41 nm x 179 nm in volume that was calibrated in depth using the STEM image. Indium quantification was performed using a reference sample consisting of an In<sub>53</sub>Ga<sub>47</sub>As layer grown on an InP substrate (Sample IGA#11). The corresponding SIMS depth profiles for III-V elements are presented in Figure IV-29 d. All the indium depth profiles are noisier after ROI reconstruction, because they come from a smaller volume, and they are similar to SIMS profiles obtained by magnetic SIMS (Figure IV-4). To ensure that the signal came only from the trenches the mass spectra were checked after reconstruction and the ROI adjusted to minimize Si containing ions. The calculated ratio of  $^{115}\text{In}^+ / ^{69}\text{Ga}$  is the same for one or all trenches and allows the indium concentration to be quantified.

However, to achieve lateral resolution for 3D reconstruction of III-V trenches in the ToF-SIMS data a high dose of bismuth ions at high energy ( $\text{Bi}_3^{++}$  60 keV) is required. The damage that is produced is not completely removed by each sputter cycle and this leads to degradation of depth resolution during depth profiling. Whereas low lateral resolution magnetic SIMS depth profiling (Figure IV-4 a) gives better depth resolution than ToF-SIMS depth profiling.

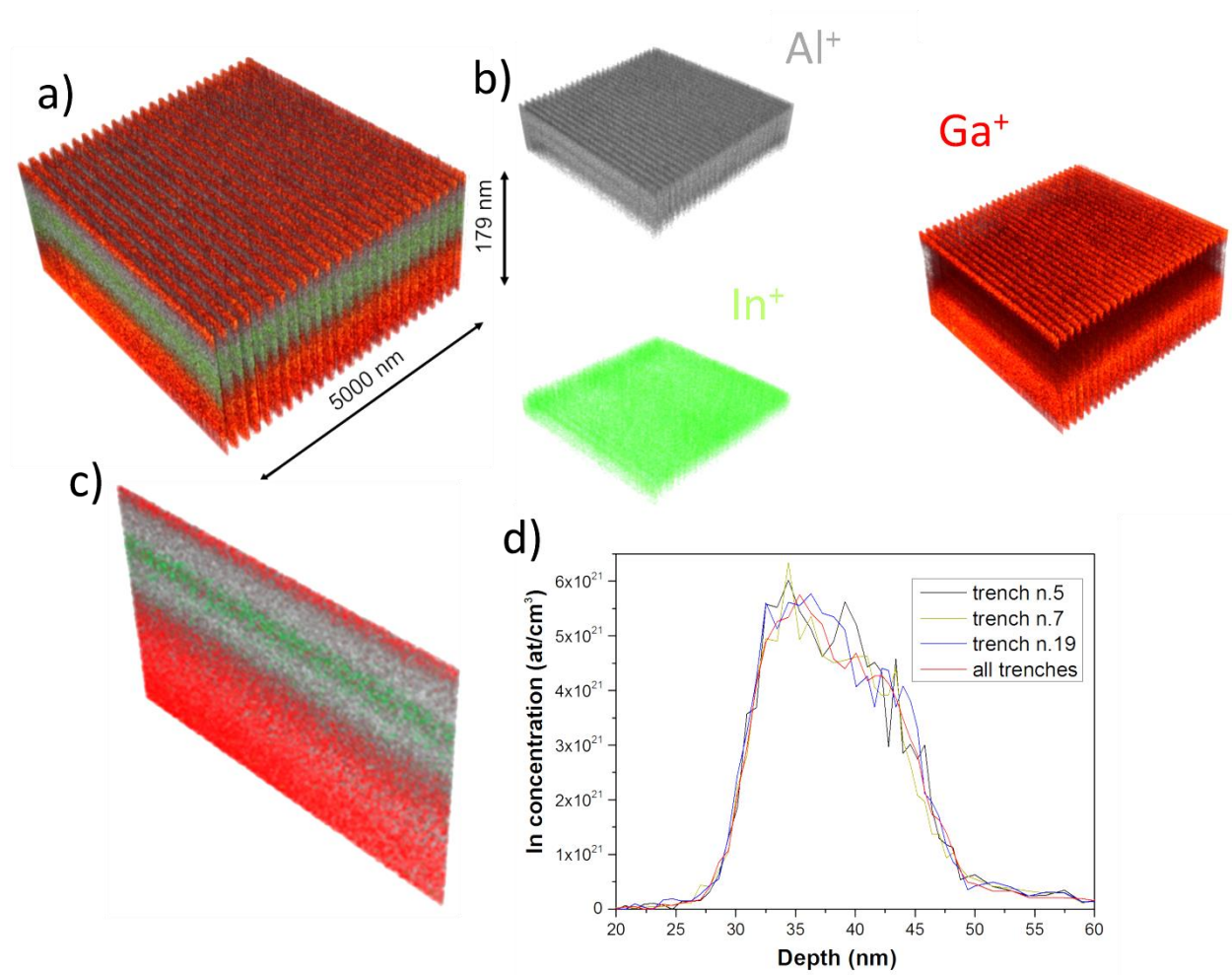


Figure IV-29 3D reconstruction of InGaAs QW with AlAs barrier layers by TOF-SIMS technique with field of view of 5  $\mu\text{m}$  x 5  $\mu\text{m}$ , b) separate reconstruction of Al, In, Ga, c) 3D volume reconstruction of an individual III-V trench of 3074 nm x 41 nm x 179 nm and d) SIMS depth profiles of trenches n°5, 7 and 19 (numbered from the top image, from left to right).

In order to achieve higher depth resolution profiling a needle-shaped APT tip containing the III-V multilayers was prepared using focused ion beam (FIB) preparation. All steps of sample preparation in detail are described in Chapter II.2.2.1. The 3D atomic distribution of the indium, aluminum, gallium and silicon atoms in  $58 \times 58 \times 173 \text{ nm}^3$  volume is presented in Figure IV-30. The volume has been obtained using a standard algorithm with a shank angle method and the depth has been calibrated using the layer thickness measured by STEM. The contamination of indium at the GaAs/Si interface can be observed, which explains the SIMS peaks (see Figure IV-4). Additionally, Si diffusion is not observed at GaAs/Si interfaces which are often observed for planar at the GaAs/Si materials [P. Murugan et al., 2002]. However, these observations require further investigations to confirm them.

The InGaAs QW of 9 nm in thickness in the APT analysis volume comes from the edge of the line where the InGaAs layer is thinner (see Figure IV-31). Figure IV-31 shows the InGaAs/AlAs

interface is extremely abrupt. However, the QW thickness is not representative of the whole line as the sample was prepared near the edge (see Figure IV-31 a, b).

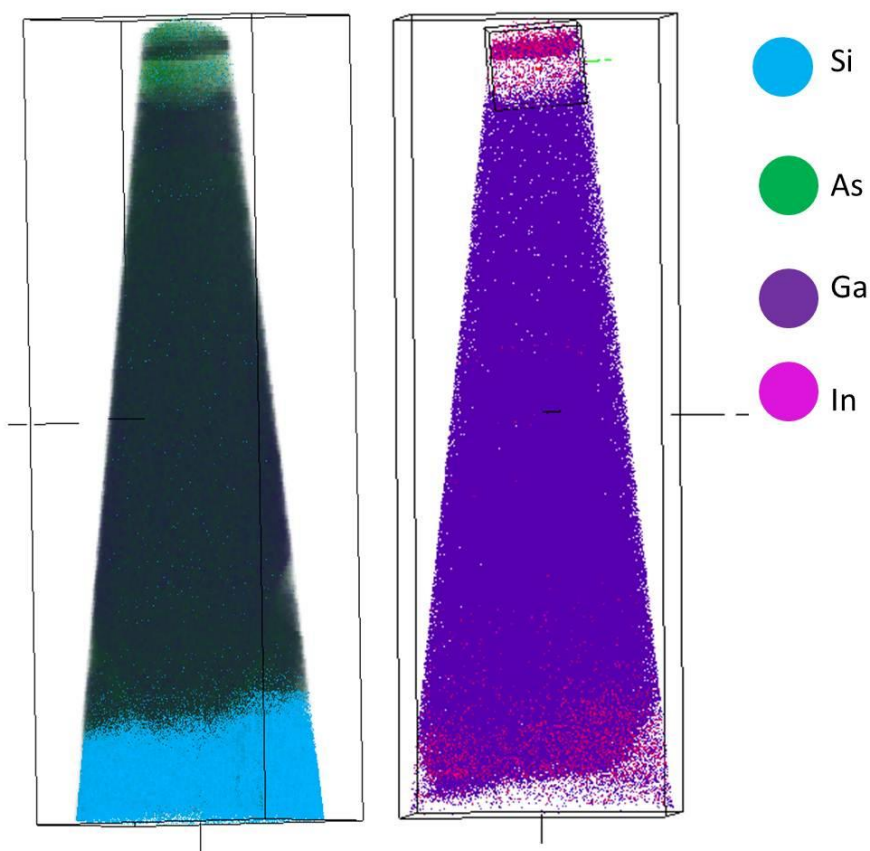


Figure IV-30 3D atomic distribution of the indium, arsenic, silicon and gallium atoms in  $58 \times 58 \times 173 \text{ nm}^3$  volume.

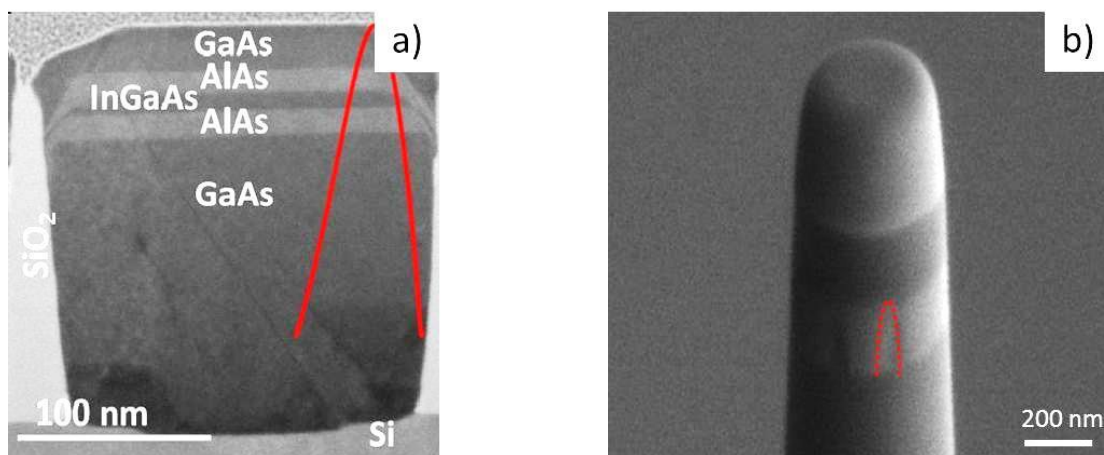


Figure IV-31 A needle-shaped tip containing InGaAs/AlAs QW in thickness of 9 nm, where a) cross section STEM image of InGaAs/QW and b) the preparation of singular III-V trench using FIB. The region of analyzed III-V heterostructures is marked in red color.

Figure IV-32 shows the 3D reconstruction of the InGaAs layer with an AlAs barrier layer in nanoscale volume where the abrupt InGaAs/AlAs interfaces can be seen. The corresponding

depth profile for InGaAs/AlAs interfaces is given in Figure IV-33. The slight variation of indium composition can be explained by the artifacts during reconstruction, either preferential evaporation of III-V element and it requires further investigation. The downslope at interface AlAs/InGaAs layers following a gallium signal is 0.5 nm/decade nm for APT profiling single trench.

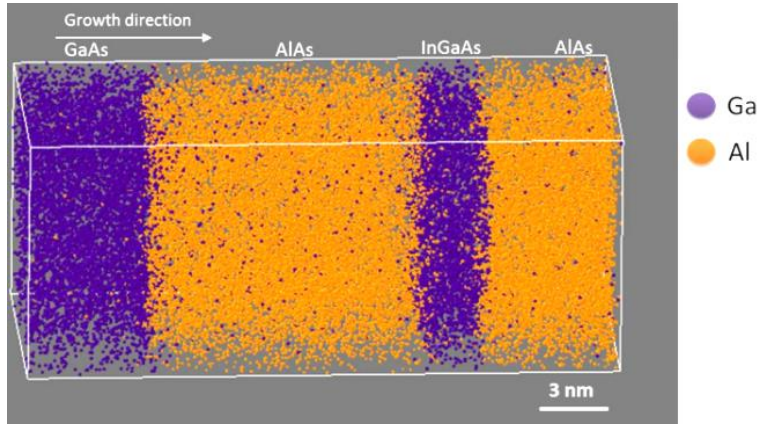


Figure IV-32 3D reconstruction of the InGaAs QW with an AlAs barrier layer.

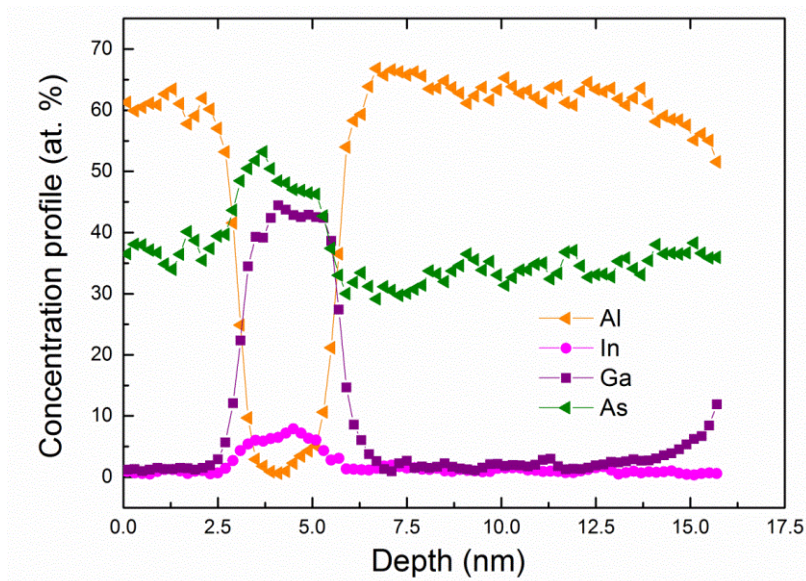


Figure IV-33 3D APT reconstruction of the InGaAs QW with an AlAs barrier layer of the FIB-prepared sample shown in Figure IV-31.

The Si diffusion in GaAs layers grown in SiO<sub>2</sub> cavities was also studied using APT and is shown Figure IV-34. The observation of arsenic clustering among the screw dislocations, which propagates from the Si substrate to the edges (see Figure IV-34 front and top view) due to lattice-mismatched materials, was observed. From the Figure IV-34 can be seen that the gallium atoms are replaced by arsenic atoms in the direction of dislocations. To confirm APT results additional experiments are required.

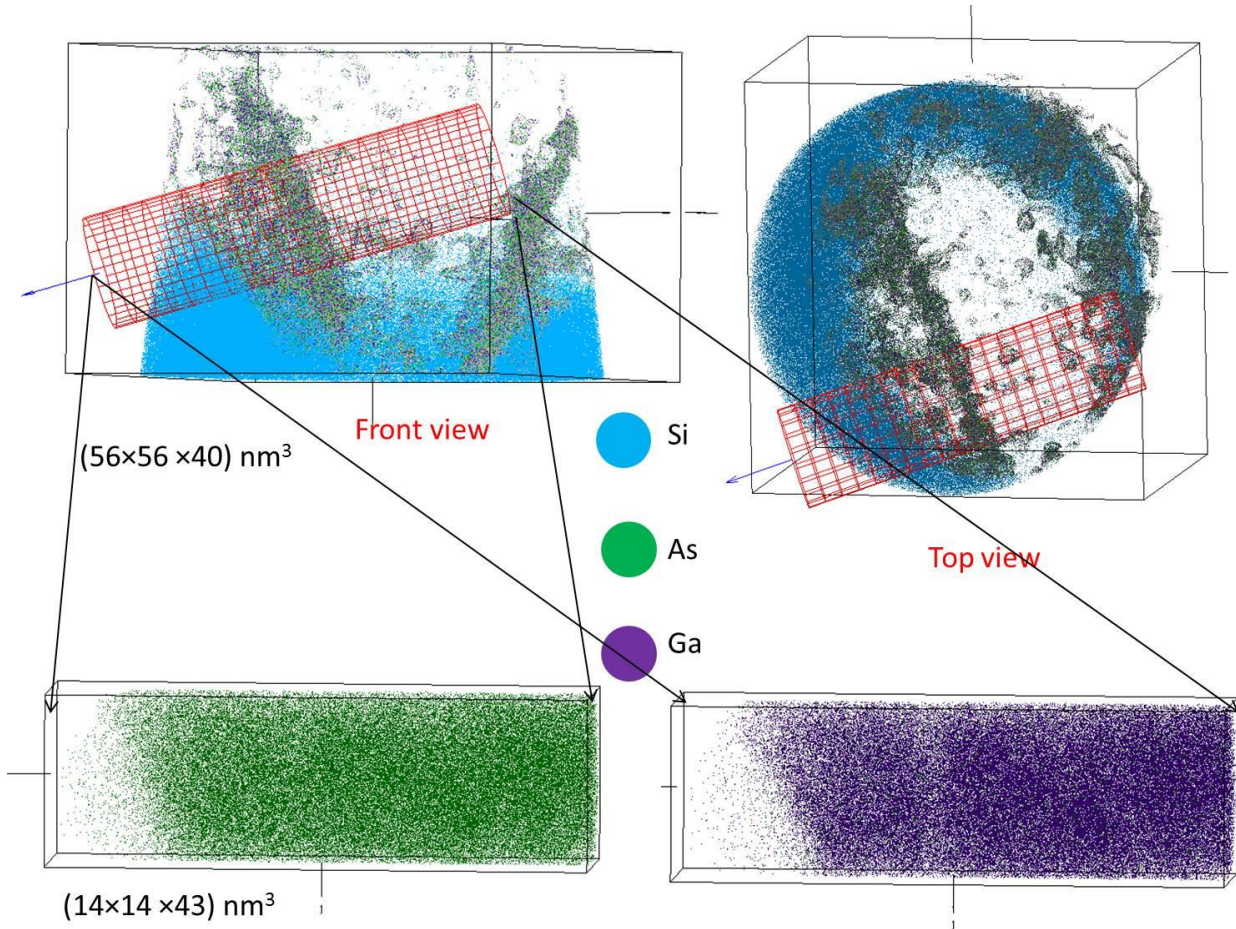


Figure IV-34 3D APT reconstructed volume of non-planar GaAs/AlAs/InGaAs QW/AlAs/GaAs/Si wafers grown by MOCVD.

In the next section, the quantitative analysis for non-planar InGaAs QWs is in detail studied.

#### IV.4 Quantitative analysis of InGaAs quantum well by Auger and SIMS techniques

SIMS results performed on non-planar InGaAs QWs (described in Chapter II.1.4.3) were compared with Auger measurements using both points (singular) and averaged analyzes. The theoretical background of Auger technique and experimental details can be found in Chapter II.2.3. As for SIMS, the Auger profiles are averaged over ~100-120 trenches using an average approach. The combination of the Auger technique with scanning electron microscopy with a lateral resolution of less than 20-30 nm also allowed individual trenches to be analyzed. The trenches were aligned in parallel to the sputter beam direction for both magnetic SIMS and Auger measurements. The profiles of the Auger electrons of Al and Ga for one trench demonstrate the same shape as the profile averaged over many trenches, but slightly sharper interfaces (Figure IV-35 a). The superposition of Auger and SIMS averaged profiles by normalization to the maximum intensity shows good correspondence (Figure IV-35 b).

Therefore, the analysis performed on a uniform and repetitive structures may give more reliable results using both techniques.

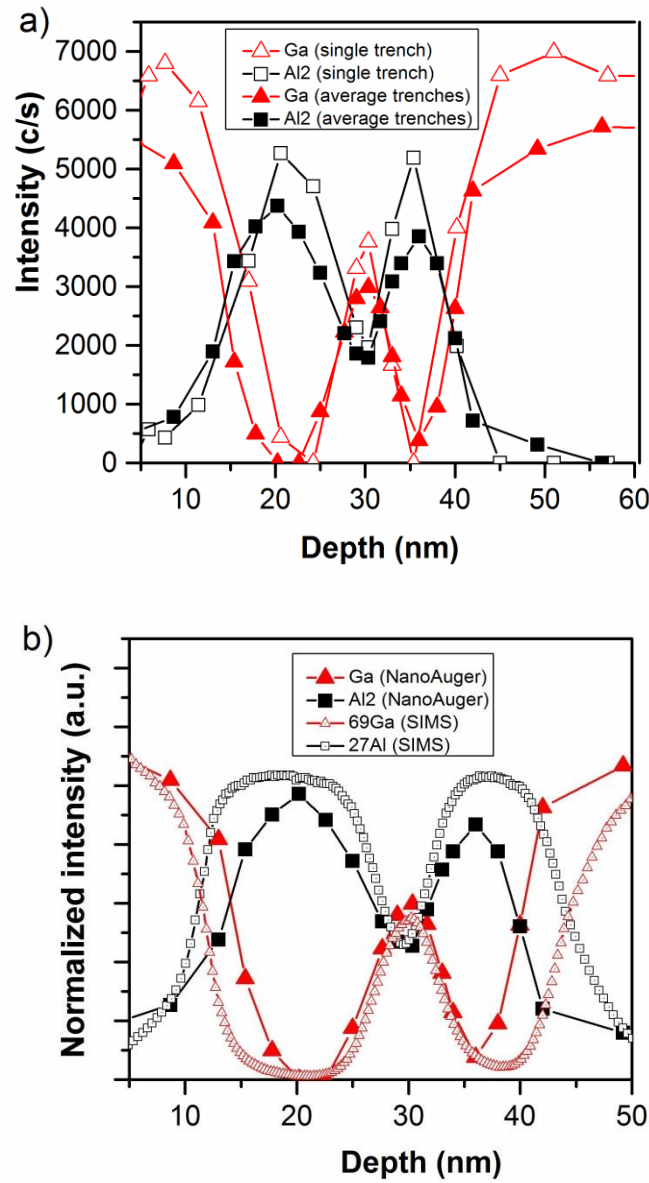


Figure IV-35 a) High depth resolution profiles of InGaAs QW with AlAs barrier layers of an individual trench and many trenches using Auger analysis b) comparison of Auger and SIMS depth profiles of average III-V trenches

The cross-section STEM images of a series of samples of non-planar  $\text{In}_{0.1 < x < 0.4}\text{Ga}_{1-x}\text{As}$  QWs with various composition of indium are presented in Figure IV-36. The slight variation in thickness of InGaAs QWs can be observed. Figure IV-37 shows that shape of the  $^{69}\text{Ga}^+$ ,  $^{115}\text{In}$  and  $^{27}\text{Al}$  profiles are well defined at the AlAs/InGaAs and InGaAs/AlAs interfaces. The multi-calibration was used to calibrate x-scale. Following those signals, the good correspondence between SIMS averaging depth profiling (Figure IV-37) and STEM images (Figure IV-36) can

## Chapter IV. Development of experimental protocols for chemical composition profiling of 3D architecture structures

be seen. The slight non-uniformity in thickness of InGaAs layers near the SiO<sub>2</sub> barriers is observed for #P10, #P07 and #P09 samples which may impact on SIMS depth profiling.

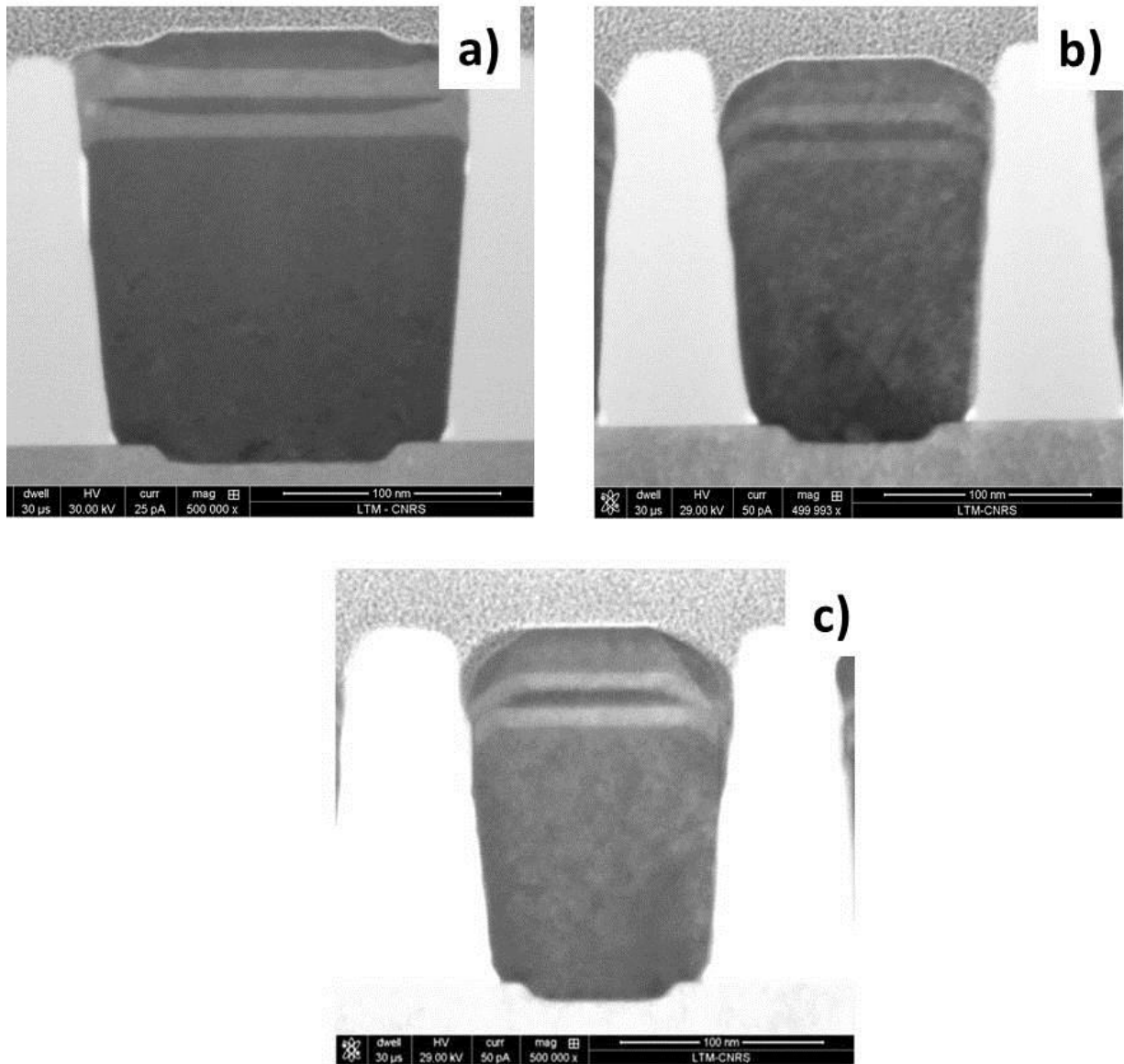


Figure IV-36 The cross-sectional view of a single trench with width of 150 nm containing InGaAs QW/AlAs in thickness of a) 8-10 nm (Sample #P10), b) 8-10 nm (Sample #P07), c) 7-9 nm (Sample #P09) selectively grown by MOCVD on 300 mm Si wafers

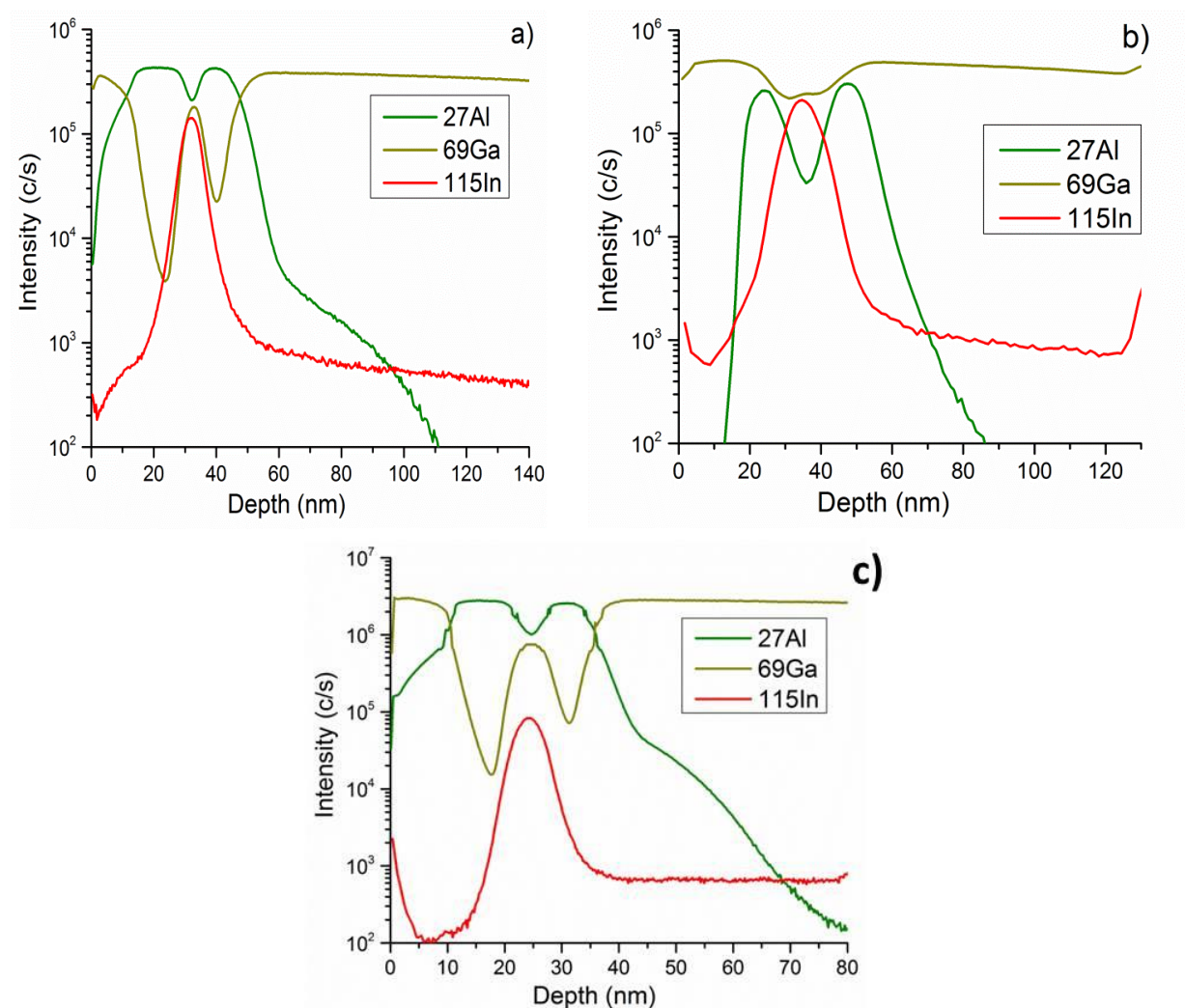


Figure IV-37 SIMS profiles of InGaAs QWs with thickness presented in Figure IV-36 a) 8-10 nm (#P10), b) 8-10 nm (#P07), c) 7-9 nm (#P09) under 500 eV energy and in the parallel direction of oxygen beam with respect to the trenches.

The indium composition in  $\text{In}_x\text{Ga}_{1-x}\text{As}$  QWs samples was studied using PL and compared with SIMS and Auger techniques. The estimated indium composition is given in Table IV-7.

**Table IV-7** Quantification of  $\text{In}_x\text{Ga}_{1-x}\text{As}$  using an average approach by SIMS, PL, and Auger

Name of Sample	#P10	#P07	#P09
Thickness of layer	8-10	8-10	7-9
Targeted In content	13	30	40
[x] %, (SIMS)	8	12	32
[x] %, (Auger)	8	18	18
[x] %, (PL)	11	33	40

## Chapter IV. Development of experimental protocols for chemical composition profiling of 3D architecture structures

To calculate the indium composition in InGaAs QWs the RSF values previously described were used for SIMS and Auger quantifications (see Chapter III.3.1 and Chapter III.3.3). The lower composition of indium for Sample #P07 and #P09 using SIMS and Auger techniques can be explained by the non-uniformity in InGaAs layer thickness at the edges of the trench. However, the good correspondence for quantitative analysis for Sample #P10 is obtained. Quantitative accuracy of non-planar III-V semiconductors using SIMS and Auger techniques depend on the shape and geometry of the structure and also the depth resolution of instruments. Indium composition estimated by SIMS and Auger is reduced to the aluminum contribution from the AlAs edges. Moreover, indium composition is more accurate due the quantum confinement in described structures is possible only in a parallel direction to the growth. Quantum confinement in parallel to the growth is illustrated in Figure IV-38a. Thus, PL gives more reliable measurements in composition compared to SIMS and Auger.

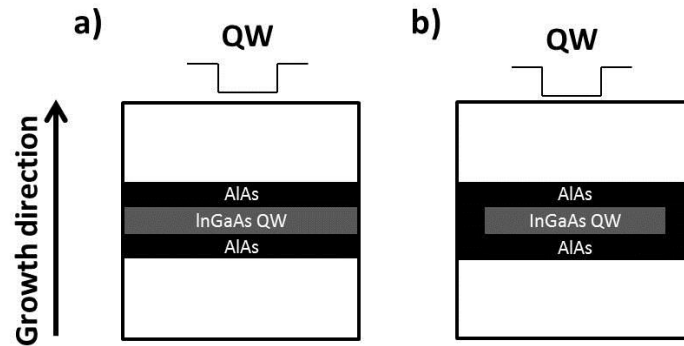


Figure IV-38 The schematic illustration of quantum confinement in III-V trenches containing the InGaAs QWs in a) ideal structure and b) actual structure.

**Conclusions:** Advanced SIMS protocols were developed in order to investigate III-V heterostructures selectively grown by MOCVD in 100-300 nm wide SiO<sub>2</sub> trenches. The effect of (i) primary energy, (ii) orientation of ion beam and (iii) incident angle with respect to the III-V trench arrays are discussed in detail. Firstly, it was shown that the effect of the primary energy on depth resolution in InGaAs materials is different to those reported for boron delta layers in silicon. The degradation of SIMS depth resolution for III-V materials was observed for low energy oxygen sputtering. These observations were confirmed using planar reference samples. The degradation of depth resolution was also confirmed by AFM measurements. For using extreme low ion beam sputtering (less than 500 eV), the higher roughness formation was observed due to the formation of ripples on the surface. Secondly, it was demonstrated that aligning the ion beam parallel to the trenches minimizes ion-beam induced surface roughness and gives better depth resolution. When the O<sub>2</sub><sup>+</sup> ion beam is incident perpendicular to the trenches the sputtering behavior may be modified due to shadowing effects, whilst the sputtering behavior of the ion beam aligned parallel orientaton to the trenches should minimize shadowing effects. Finally, the depth resolution also depends on the incident angle of the ion beam. Increasing the incident angle from 50° to 62° leads to improvement of the depth resolution by more than 1nm/decade and thus, these results are promising for high depth resolution profiling

## Chapter IV. Development of experimental protocols for chemical composition profiling of 3D architecture structures

---

of thinner III-V trenches. Additionally, it was shown that sample rotation during the ion beam sputtering smooths the surface. However, this leads to artifacts such as the tailing effect of the indium signal due to sputtering in non-preferable orientation on patterned samples. Moreover, it was demonstrated that the analysis using cesium bombardment (250 eV) may be not suitable for high depth profiling of III-V trench arrays. High roughness formation on bulk GaAs (reference sample) was observed under cesium bombardment whilst no significant improvement in depth resolution was obtained at a primary energy of 250 eV.

Additionally, it was shown that the obtained SIMS depth profiles are fully consistent with reconstructed profiles obtained from individual trenches using dual-beam TOF-SIMS and Auger. This shows that averaged measurements in uniform, repetitive structures can be used for reliable chemical characterization of III-V heterostructures. The ability to make averaged depth profiles and 3D TOF-SIMS reconstructions of patterned heterostructures of a few hundred nanometers in width will be useful for chemical identification of more complex 3D architecture devices.

Furthermore, for accurate quantitative analysis III-V trenches using SIMS and Auger the lateral uniformity in thickness of layers should be considered. The composition given by these techniques is an average one over the entire trench and may not necessarily agree with more localized concentration measurements (APT or PL) if the layer thickness is not uniform. The correlation with cross-sectional STEM image is important to interpret SIMS and Auger profiles.

**REFERENCES:**

- [R. M. Bradley, et al. 1996] Theory of improved resolution in depth profiling with sample rotation, *Applied Physics Letters*, **68** (26), pp. 3722-3724.
- [R. M. Bradley, et al. 1988] Theory of ripple topography induced by ion bombardment, *Journal of Vacuum Science & Technology A*, **6** (4), pp. 2390-2395.
- [K. Elst, et al. 1997] The study of ripple formation and degradation of depth resolution in GaAs and Al<sub>x</sub>Ga<sub>1-x</sub>As structures, *International Journal of Mass Spectrometry and Ion Processes*, **171** (1-3), pp. 191-202.
- [B. Gautier, et al. 1996] Deconvolution of SIMS depth profiles of boron in silicon, *Surface and Interface Analysis*, **24**(11), pp.733-745
- [C. Gerardi, 1997] SIMS analyses of III-V semiconductor quantum-well and superlattice heterostructures, *Surface and Interface Analysis*, **25** (6), pp. 397-403.
- [M. J. P. Hopstaken, et al. 2010] Sputtering behavior and evolution of depth resolution upon low energy ion irradiation of GaAs, *Journal of Vacuum Science & Technology B: Microelectronics and Nanometer Structures*, **28** (6), pp. 1287.
- [M. Juhel, et al. 2006] SIMS depth profiling of boron ultra-shallow junctions using oblique O<sub>2</sub><sup>+</sup> beams down to 150 eV, *Applied Surface Science*, **252** (19), pp. 7211-7213.
- [A. Karen, et al. 1993] Dependence of rippled topography of the sputtered surfaces on the energy and the incident angle of the O<sub>2</sub><sup>+</sup> beam in Secondary ion mass spectrometry SIMS VIII, Secondary ion mass spectrometry SIMS VIII.
- [K. Muraki, et al. 1992] Surface segregation of In atoms during molecular beam epitaxy and its influence on the energy levels in InGaAs/GaAs quantum wells, *Applied Physics Letters*, **61** (5), pp. 557-559.
- [P. Murugan, et al. 2002] Si diffusion in GaAs, *Bulletin Material Science*, **25** (4), pp. 335-340
- [Y. Nakagawa, et al. 1992] Scanning tunneling microscopy study of the ripple formation on sputtered surfaces, New York, John Wiley.
- [R.G. Wilson, et al. 1989] Secondary ion mass spectrometry A Practical Handbook for Depth Profiling and Bulk Impurity Analysis, Wiley.
- [P. Sigmund, 1973] A mechanism of surface micro-roughening by ion bombardment, *Journal of Materials Science*, **8** (11), pp. 1545-1553.
- [W. Vandervorst, 2008] Semiconductor profiling with sub-nm resolution: Challenges and solutions, *Applied Surface Science*, **255** (4), pp. 805-812.

## CONCLUSIONS

This thesis reports on the physico-chemical characterization of III-As heterostructures grown by MOCVD on 300 mm Si wafers. These as-grown heterostructures have a strong potential in the near future for micro- and optoelectronic applications. The optimization of growth conditions is essential to achieve high-quality III-As materials on Si wafers. The main issues for the characterization of non-planar III-As materials were addressed such as (i) *How to study depth profiling in thin layers (less than 10 nm) in 3D architecture*, (ii) *How to study the composition in thin layers in 3D architecture* (iii) *How to measure the doping concentration in non-planar materials*. For this, the Cameca SC Ultra instrument designed for high depth resolution profiling of semiconductors was used. Additionally, complementary techniques were performed such as ToF-SIMS, Auger, and PL to confirm the SIMS results. The main results, obtained in the framework of this thesis, are summarized below.

- Advanced SIMS protocols for InGaAs QWs grown by MOCVD on 300 mm Si wafers were developed. SIMS experiments were carried out using oxygen sputtering at 250 eV to 5000 eV energy range to achieve a high ion yield of III-group elements. For this, specially grown and designed series of planar InGaAs layers were used for SIMS analysis. The reference samples were studied for accurate compositional analysis using non-destructive techniques, e.g. RBS, PIXE, and PIGE. Moreover, ion implanted reference samples were fabricated to study doping and contamination in III-V materials. A series of  $\text{In}_x\text{Ga}_{1-x}\text{As}$  reference samples were used to create the calibration curve for indium and gallium elements. Additionally, the ion and sputter yield as a function of  $x$  fraction and ion beam energy were studied. Quantitative analysis using  $\text{MCs}^+$  was also demonstrated under cesium ion beam sputtering with energy lower than 1 keV. However, analysis conditions using oxygen sputtering are preferable and mainly used to investigate planar and non-planar InGaAs QWs.
- InGaAs QWs with different thicknesses (6, 10 and 19 nm) grown by MOCVD on Si were investigated. The indium composition in  $\text{In}_x\text{Ga}_{1-x}\text{As}$  QWs was estimated from the position of the  $\mu\text{PL}$  peak. SIMS conditions using oxygen sputtering at an energy of 500 eV were chosen to study thin InGaAs layers. The calibration curve using reference samples was used to quantify the indium and gallium elements in  $\text{In}_x\text{Ga}_{1-x}\text{As}$  QWs. SIMS results show that accurate quantitative profiling of thin layers in thickness less than 5-10 nm is challenging and leads to inaccuracy in quantification. Indeed, the accurate quantitative analysis is limited by SIMS depth resolution. Further, the underestimated composition of indium in InGaAs QWs of 5-10 nm compared to  $\mu\text{PL}$  was also observed using Auger technique, which is also limited by the depth resolution. These results were then used in developing quantitative chemical analysis protocols for non-planar structures.
- SIMS protocols were carefully optimized to study more complex structures such as III-As trenches selectively grown using the ART method on patterned 300 mm Si wafers. A good quality of non-planar InGaAs/AlAs QWs of 10 nm in thickness was observed by  $\mu\text{PL}$

signals at room temperature. Despite an insufficient lateral resolution (better than  $1\mu\text{m}$ ), the possibility to perform an accurate chemical profiling of InGaAs QWs in trenches surrounded by  $\text{SiO}_2$  walls was demonstrated. For this purpose, SIMS depth profiling for III-V trenches of 100-200 nm in width the averaging profiling method was developed. This established method is based on the following assumptions: (i) the structures are repetitive, and (ii) the signal from many adjacent trenches approaches the signal that would be obtained from one single trench. SIMS chemical depth profiling using this method has shown abrupt III-V interfaces and confirmed the PL observations. The chemical profiles for narrow and repetitive III-V trenches demonstrate good agreement with cross-sectional STEM observations. The averaging profiling method was confirmed by Auger measurements performed on individual III-V trenches using both pointed and average analysis methods.

- For accurate quantitative SIMS depth profiling, the depth resolution on III-V trench arrays has to be optimized in order to understand SIMS signals correctly and to avoid artifacts due to the 3D-structure of the sample. SIMS experimental conditions were optimized by considering the following parameters i) the primary energy, ii) the ion beam incident angle, and iii) the oxygen ion beam orientation with respect to the III-V trenches. High SIMS depth resolution (less than 3-4 nm) can be obtained using extremely low primary ion energy (less than 500 eV). However, the results have shown that reducing the primary oxygen ion beam impact energy down to 150 eV leads to an increase of the surface roughness and thus, depth resolution degradation. It is explained by the ripple formation observed by AFM measurements under oxygen irradiation. Furthermore, the effect of ion beam orientation with respect to the trenches was studied. The results show that the depth resolution is improved using the parallel orientation of the ion beam with respect to the trenches. Contrary to the perpendicular orientation of ion beam with respect to the trenches which leads to the sputtering artifacts and depth resolution degradation. Additionally, depth resolution might be affected by the incident angle of oxygen ion beam. It was demonstrated that depth resolution improves when increasing the oxygen ion beam incident angle. Moreover, the impact of sample rotation under oxygen ion beam sputtering of III-V trenches was also studied. Less roughness on the III-V surface under oxygen irradiation using sample rotation was observed by AFM. However, no significant depth resolution improvement and the tailing effect were observed. This can be explained by a shadowing effect at III-V/ $\text{SiO}_2$  interfaces due to the sample being perpendicular to the ion beam for part of the time during sample rotation. This was observed using AFM and is consistent with previous observations for perpendicular orientation of the ion beam with respect to the trenches. Although in the case of sample rotation the shadowing effect is seen on both sides of the  $\text{SiO}_2$  walls.
- The quantitative analysis for a series of non-planar thin (9 nm in thickness) InGaAs QWs was performed using both SIMS and Auger techniques. It was observed that SIMS and Auger quantification strongly depends on the slight variation in thickness of the layers as well as their geometrical shape. There is a discrepancy in indium composition found using SIMS and Auger compared to that extracted from  $\mu\text{PL}$  measurements. This difference comes from the AlAs edges, which contribute to SIMS and Auger signals reducing the

apparent indium composition of the InGaAs QWs. For PL, it doesn't contribute because quantum confinement is parallel to the growth direction and therefore, the extracted indium composition is higher.

- Quantitative analysis and 3D chemical distribution of atoms in InGaAs QWs grown on patterned Si were obtained using ToF-SIMS and APT. The measurements are found consistent and show good uniformity in composition. Abrupt InGaAs/AlAs interfaces were demonstrated using APT with a high depth resolution of less than 1 nm/decade while both SIMS and ToF-SIMS are more adapted for chemical profiling of repetitive uniform structures. Nevertheless, APT gives the information from a tiny volume of one trench and which may be not representative of the whole array of trenches and when trench width became narrow (less than 40 nm) the presence of SiO<sub>2</sub> sidewalls will make distortions in the APT volume.
- SIMS and ToF-SIMS protocols for Si-dopant concentration measurements in 2D and 3D architectures were developed using an average method. Samples containing GaAs (n-doped) /GaAs stack selectively grown on patterned Si substrates were studied. However, the presence of SiO<sub>2</sub> barrier walls makes the Si doping measurements challenging. One solution to overcome this issue was to remove SiO<sub>2</sub> barriers using an HF etch. It was found that using SiAs, SiGa ions the Si dopants in GaAs/Si to be distinguished. Additionally, it was demonstrated that the ion beam orientation to the trenches has an impact on the dopants limitations because in perpendicular orientation the substrate is less visible than in parallel orientation and this contributes less to the overall Si signal.

In conclusion, SIMS protocols for InGaAs channel materials and doping profiling in repetitive narrow structures with high depth resolution were developed. The ability to make averaged depth profiles and 3D chemical profiling of confined III-V heterostructures a few hundred nanometres in width will be useful for chemical identification of more complex devices. All reported results may find applications in future III-V FinFET or III-V FD-SOI devices monolithically integrated on Si.

## **PERSPECTIVES:**

To follow the tendencies in a semiconductor technology such as scaling and development of complex multi-material structures the improvement of SIMS and ToF-SIMS instrumental is required. It is necessary to improve the lateral and depth resolution by the implementation of new ion beam sources. Additionally, to better understand the influence of material geometry and shape on the chemical profiling of fin or trench arrays the numerical simulations or in-situ correlation with AFM measurements could be developed.

The III-V growth in fin arrays of less than 40 nm in width for FinFET technology may lead to new characterization challenges. Such thin structures remain to be tested using SIMS and correlated with STEM images. Another perspective for the SIMS analysis of fin structures is the use of more advanced sample preparation (etching the SiO<sub>2</sub> walls, filling with another material, planarization of the surface).

The studies of Si diffusion from the substrates in FinFET devices have to be investigated. The Si diffusion in GaAs layers on non-planar Si substrates was studied using APT and SIMS in this work. However, due to difficulties of interpretation all results were not included in this work because it is hard to achieve a low enough detection limitation due to the presence of SiO<sub>2</sub> sidewalls. The improvement of FIB preparation for APT by removing the SiO<sub>2</sub> and replacing with amorphous silicon could be investigated to minimize the reconstruction artifacts due to the presence of SiO<sub>2</sub> sidewalls.

## Annex II.A

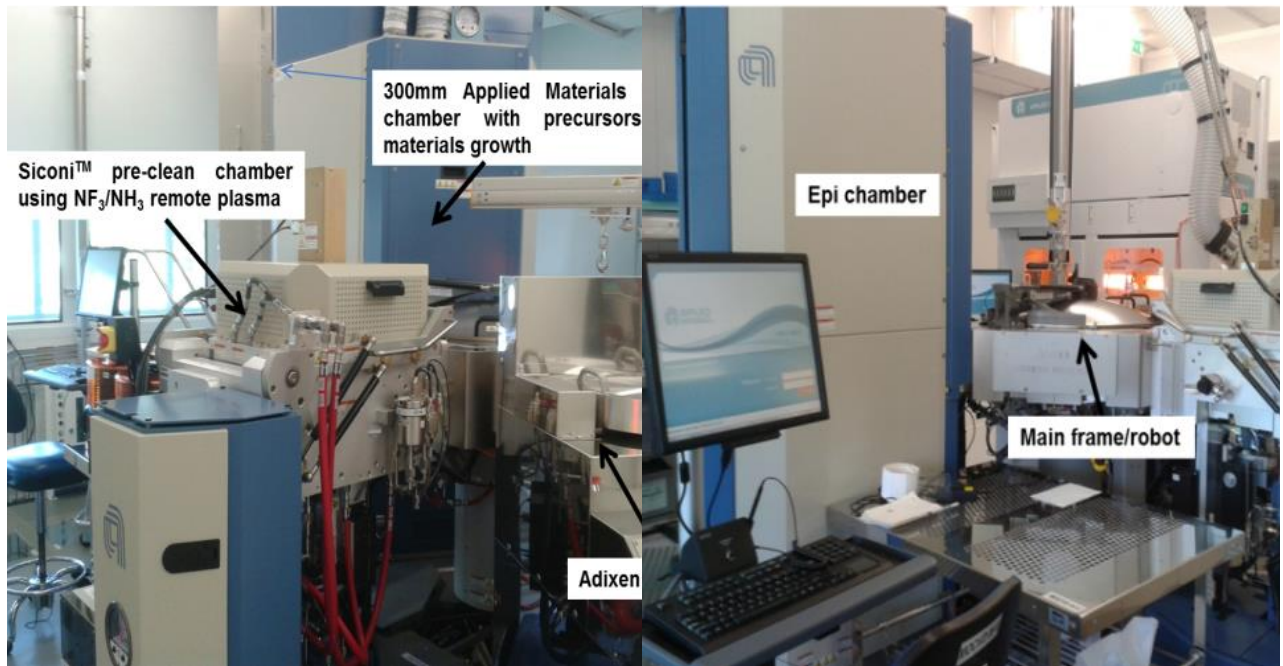


Figure II.A. Illustration of MOCVD AMAT tool platform installed in 2013 at CEA/LETI-CNRS/LTM, Grenoble, France.

## Annex II.A

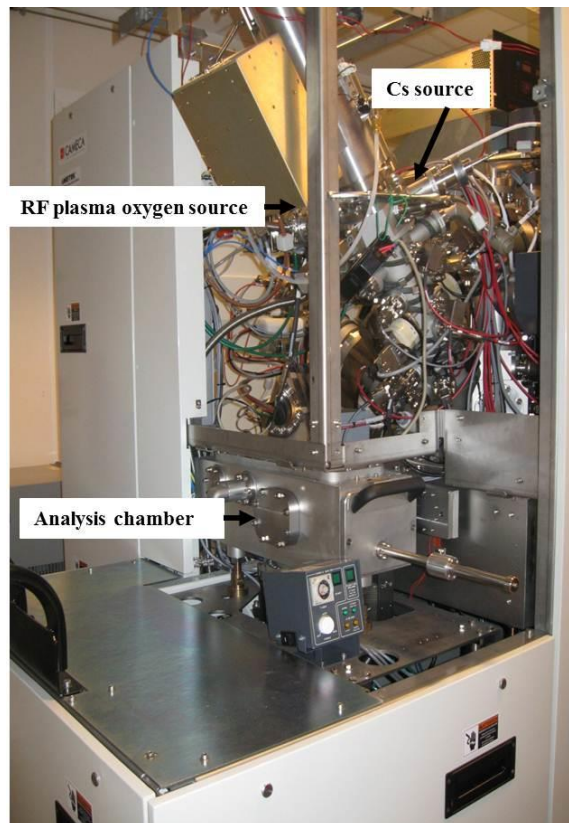


Figure.II.B Cameca SIMS SC-Ultra instrument installed on Nanocharacterization platform at CEA/LETI

## Annex II.C

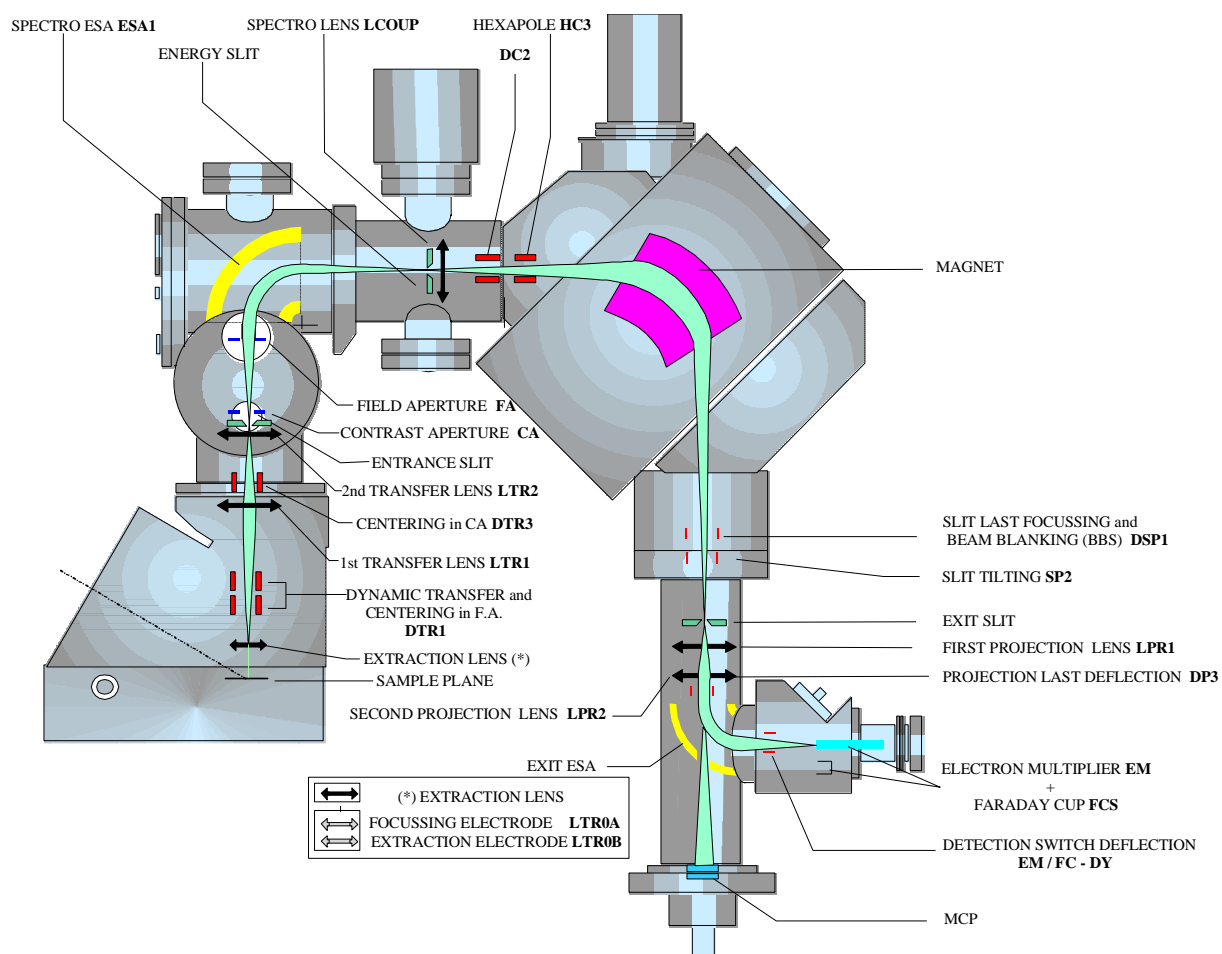


Figure II. C.Schematic structure of SC-Ultra secondary optics. Figure is taken from reference [CAMECA, 2014]

## Annex III.A

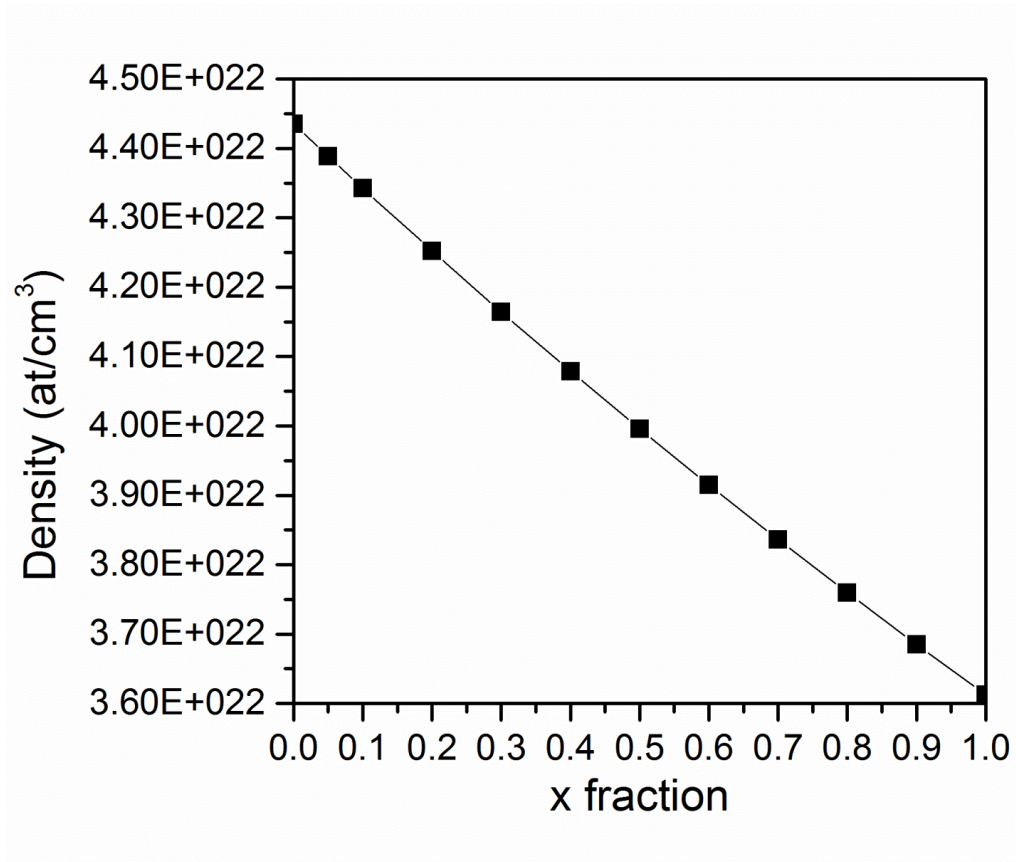


Figure III.A Density of  $\text{In}_x\text{Ga}_{1-x}\text{As}$  materials as a function of  $x$

## **Annex III.B**

### **Calculation of Indium composition using photoluminescence measurements**

The excitation was provided by a continuous wave He-Ne laser beam (632.8 nm) focused by a microscope objective to a spot size of about 5  $\mu\text{m}$ . The PL emission was collected by the same microscope objective and sent to a monochromator equipped with a nitrogen cooled InGaAs photodiode array detector. The calculation is performed using the simulator “Nextnano”.

## Annex IV.A

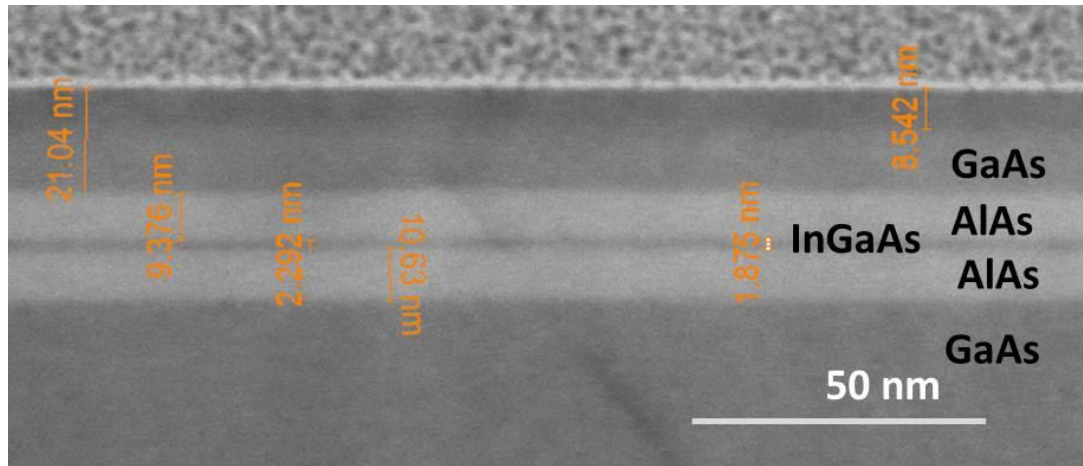


Figure IV.A. STEM-cross section image of InGaAs/AlAs QW of 2 nm grown on planar Si 300 mm wafers by MOCVD

## Annex IV.B

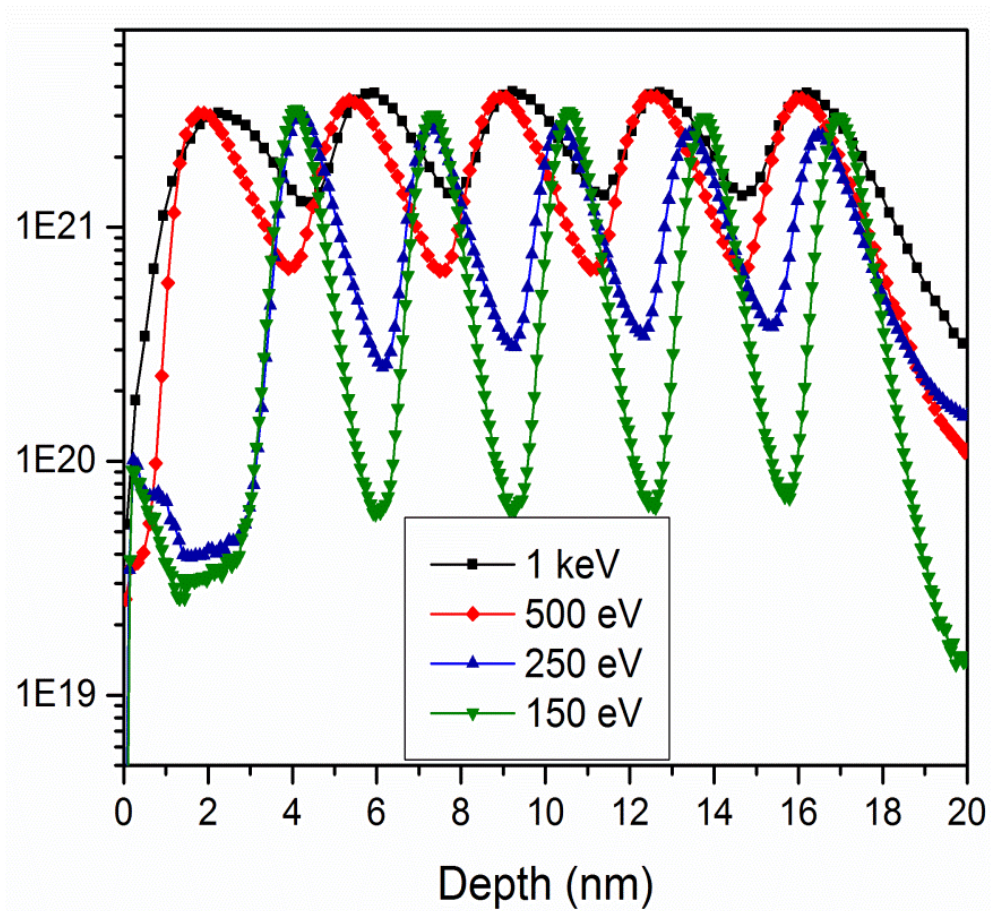
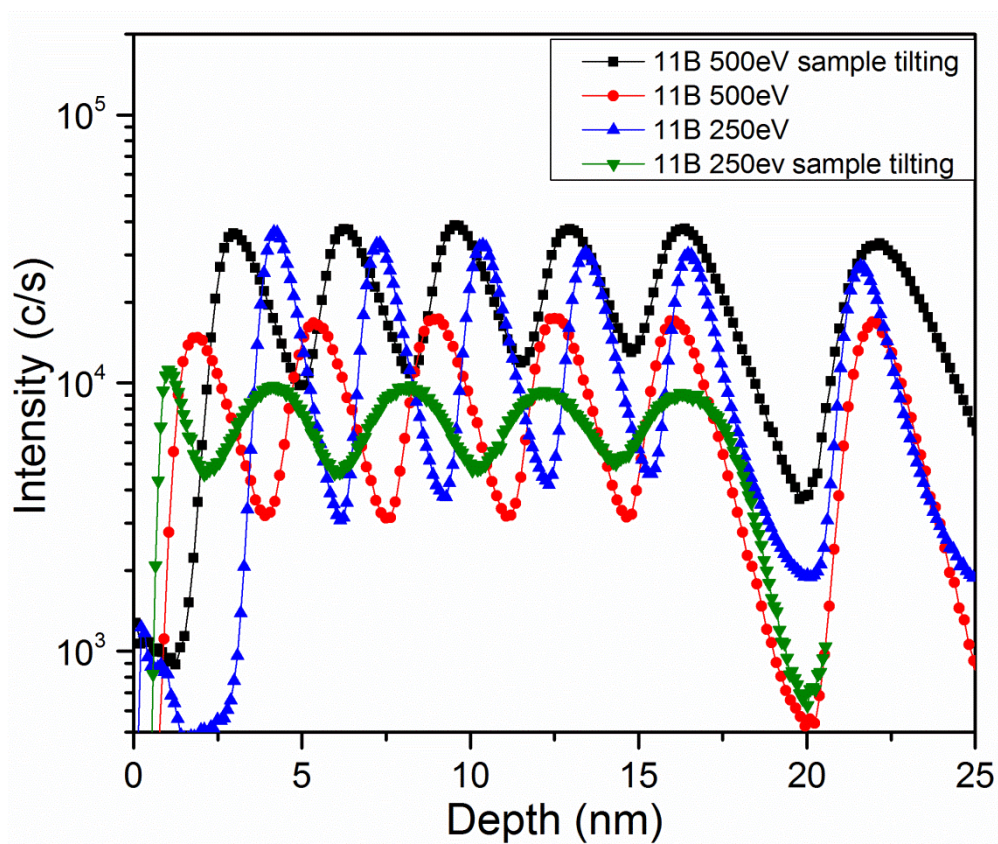


Figure IV.B. Comparison of depth profiling of boron-doped Si under 1 keV ( $39^\circ$ ) with oxygen flooding, 500 eV ( $42^\circ$ ), 250 eV ( $49^\circ$ ) and 150 eV ( $53^\circ$ ) oxygen ion beam bombardment

## Annex IV.C



Annex IV.C Comparison of depth profiling of boron-doped Si boron delta-doping in Si profiling under 500 eV ( $42^\circ$ ) with and without sample tilting, 250 eV ( $49^\circ$ ) with and without sample tilting using oxygen ion beam bombardment

## Annex IV.D

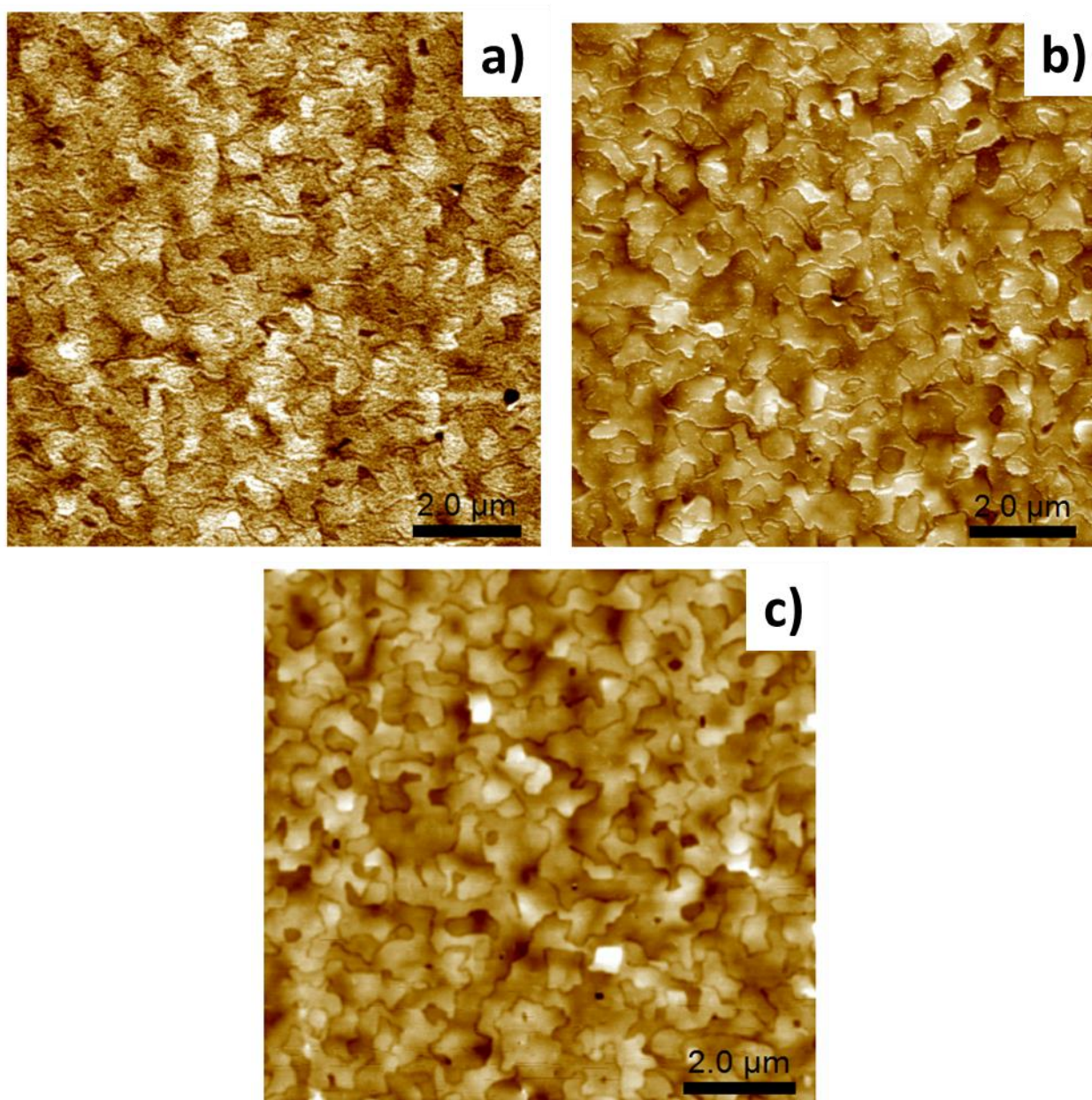


Figure IV.D. AFM observations of III-V materials under sample rotation

# List of publications and presentations

## PUBLICATIONS

- Chemical depth profiling and 3D reconstruction of III-V heterostructures selectively grown on non-planar Si substrates by MOCVD, **V. Gorbenko**, M. Veillerot, A. Grenier, G. Audoit, W. Hourani, E. Martinez, R. Cipro, M. Martin, S. David, X. Bao, F. Bassani, T. Baron, J.-P. Barnes, Phys. Status solidi RRL 9, pp. 202-205, (2015).
- Chemical characterization of III-V heterostructures in 3D architecture, **V. Gorbenko**, A. Grenier, G. Audoit, R. Cipro, M. Martin, S. David, X. Bao, F. Bassani, T. Baron, J.-P. Barnes, Microelectronics Journal, 147, pp. 219-222, (2015).
- SIMS depth profiling and topography studies of III-V trenches under oxygen ion beam sputtering, **V. Gorbenko**, F. Bassani, A. Merkulov, T. Baron, M. Martin, S. David, J.-P. Barnes, submitted to JVST Journal.
- Low defect InGaAs quantum well selectively grown by metal organic chemical vapor deposition on Si(100) 300 mm wafers for next generation non-planar devices, R. Cipro, T. Baron, M. Martin, J. Moeyaert, S. David, **V. Gorbenko**, F. Bassani, Y. Bogumilowicz, J.-P. Barnes, N. Rochat, V. Loup, C. Vizios, N. Allouti, N. Chauvin, X.Y. Bao, Z. Ye, J.B. Pin, E. Sanchez, Applied Physics Letters, 104, 262103, (2014).
- Nanoscale Auger depth profiling of III-V heterostructures, W. Hourani, **V. Gorbenko**, J.-P. Barnes, R. Cipro, F. Bassani, T. Baron, E. Martinez, submitted to Nanotechnology journal.

## CONFERENCES

- High depth resolution SIMS profiling and topography studies of III-V heterostructures in 3D architecture under low ion beam sputtering, **V. Gorbenko**, F. Bassani, T. Baron, R. Cipro, M. Martin, A. Grenier, Y. Bogumilowicz, G. Audoit, J.-P. Barnes, *oral presentation* at SIMS XX, Seattle, USA, (2015).
- Ultralow energy SIMS depth profiling of patterned III-V heterostructures, **V. Gorbenko**, F. Bassani, T. Baron, R. Cipro, M. Martin, A. Grenier, Y. Bogumilowicz, G. Audoit, X.Y. Bao, Z. Ye, J.B. Pin, E. Sanchez, J.-P. Barnes, *oral presentation* at Europe MRS, Lille, France, (2014).
- Going beyond the lateral resolution of SIMS depth profiling, **V. Gorbenko**, J.-P. Barnes, M. Veillerot, F. Bassani, R. Cipro, T. Baron, *oral presentation* at SIMS meeting, Nancy, France, (2014).
- SIMS high-resolution depth profiling for 2D and 3D architecture devices for microelectronic applications, **V. Gorbenko**, M. Veillerot, A. Grenier, G. Audoit, W. Hourani, E. Martinez, R. Cipro, M. Martin, S. David, X. Bao, F. Bassani, T. Baron, J.-P. Barnes, *oral presentation* at SIMS Europe, Munster, Germany, (2014).

- Chemical characterization of III-V heterostructures in 3D architecture, **V. Gorbenko**, A.Grenie, G. Audoit, R. Cipro, M. Martin, S. David, X. Bao, F. Bassani, T. Baron, J.-P. Barnes, *oral presentation* at INFOS conference, Udine, Italy, (2015).
- In, Al, Ga, As compounds grown by MOCVD for MOSFET channel on blanket and patterned 300 mm Si (100) substrates exhibiting room temperature photoluminescence, T. Baron, R. Cipro, M. Martin, F. Bassani, **V. Gorbenko**, J.-P. Barnes, Y. Bogumilovicz, P. Gergaud, N. Rochas, V. Loup, C. Vizioz, K. Yckache, N. Chauvin, X.Y. Bao, Z.Ye, D. Carlson, JB Pin, E. Sanchez, *oral presentation* at MRS spring, San-Francisco, USA, (2014).
- Auger depth profiling of patterned III-V heterostructures at the nanoscale, E. Martinez, W. Hourani, **V. Gorbenko**, J.-P. Barnes, R. Cipro, F. Bassani, T. Baron, *oral presentation* at ECASIA, Granada, Spain, (2015).

## DISTINCTIONS

*Awarded Young Scientific Award at E-MRS Spring Meeting, Lille, France, 2014*





## RÉSUMÉ

La miniaturisation continue des circuits intégrés nécessite l'intégration de matériaux avancés pour améliorer les performances du transistor. L'intégration de composés semi-conducteurs III-V sur silicium devrait conduire au développement de nouveaux dispositifs micro- et optoélectroniques performants. Les matériaux III-V ont des propriétés physiques intéressantes, comme un haut transport de porteurs, direct et à large bande. Le composé InGaAs de haute mobilité électronique est un candidat prometteur pour le transistor métal-oxyde-semiconducteur à effet de champ à canal n au-delà du nœud technologique 10 nm. En outre, les semi-conducteurs III-V sont aussi des matériaux appropriés pour la fabrication de composants optiques (lasers, diodes) et de dispositifs analogiques ultra-haute fréquence et leur intégration sur silicium ajoutera de nouvelles fonctionnalités pour le réseau de communications optiques. Cependant, l'intégration d'III-V sur silicium a des défis liés à la croissance, un décalage thermique et treillis de semi-conducteurs, ce qui affecte l'opération du dispositif.

L'intégration de matériaux III-V dans les architectures 3D, par exemple comme le transistor à effet de champ de type fin (FinFET), triple grille (Tri-Gate), grille Omega (Omega-Gate), est une solution pour obtenir un meilleur contrôle électrostatique du canal et une meilleure immunité contre les effets de canaux courts. L'intégration de ces matériaux dans les architectures 3D nécessite le développement de méthodes de caractérisation de pointe pour fournir des informations sur leur composition physico-chimique avec une résolution à l'échelle nanométrique. Dans ce travail, la caractérisation physico-chimique des matériaux III-As crus par dépôt chimique en phase vapeur organométallique (MOCVD) sur des plaquettes de Si 300 mm est adressée. Les principales questions pour la caractérisation des matériaux III-As crus sur substrats de Si plans et structurés sont abordées, tels que (i) *Comment quantifier la composition chimique de couches minces non planes*, (ii) *Comment améliorer la résolution en profondeur pour étudier les interfaces en couches minces dans architectures 2D et 3D* (iii) *Comment mesurer le dopage dans les couches dans architectures 3D*.

Les techniques de spectrométrie de masse d'ions secondaires sont utilisées et développées dans le but d'étudier la raideur des interfaces, la composition chimique et le dopage de couches III-V minces dans des architectures 2D et 3D avec une bonne résolution en profondeur. L'analyse

quantitative précise sur un puits quantique InGaAs (PQ) pour des architectures 2D et 3D a été réalisée en utilisant les techniques SIMS magnétique et Auger. Pour obtenir le profil chimique des structures III-V étroites et répétitives, une méthode de moyenne des profils a été développée pour ces deux techniques. Egalement, la reconstruction 3D et le profil en profondeur de tranchées individuelles (moins de cent nanomètres de largeur) contenant un PQ d'InGaAs mince obtenu par croissance sélective dans des cavités de dioxyde de silicium en utilisant la méthode de piégeage des défauts par rapport d'aspect ont été obtenus avec succès en utilisant le SIMS à temps de vol ainsi que la sonde atomique tomographique. Enfin, les résultats ont été corrélés avec des mesures de photoluminescence.

Cette thèse est organisée selon les quatre chapitres suivants.

**Le chapitre I** introduit la technologie d'intégration III-V sur des plaquettes de silicium. La première section décrit les propriétés physiques des matériaux III-V qui les rend appropriés pour les applications opto- et micro-électronique. En particulier, l'application principale des matériaux III-V sur Si est leur utilisation comme matériaux canal dans la technologie des nMOSFET. Cette section aborde les challenges technologiques pour les structures III-V FinFET et FDSOI. Les approches les plus prometteuses et récemment utilisées pour intégrer les matériaux III-V sur des plaquettes de silicium tels que le collage moléculaire, la sur-épitaxie latérale et le piégeage par rapport d'aspect sont décrites. La deuxième partie se concentre sur les questions de caractérisation de matériaux dans les architectures 3D. Elle résume les travaux récemment obtenus concernant les profils 3D de dopage ainsi que les profils de composition chimique des couches minces d'InGaAs.

**Le chapitre II** décrit les techniques de croissance et de caractérisation ainsi que les échantillons étudiés dans cette thèse. La première section de ce chapitre se concentre sur le processus de croissance épitaxiale d'hétérostructures III-V sur plaquettes de Si 300 mm en utilisant la MOCVD. Les défis et les méthodes pour obtenir des couches III-V de haute qualité sur des plaquettes de silicium sont adressées. La description de puits quantiques InGaAs (PQ) et des échantillons GaAs dopées crues par MOCVD étudiée par spectrométrie magnétique de masse d'ions secondaires (SIMS) et SIMS à temps de vol (ToF-SIMS) est donnée. La première section comprend également la description de l'échantillon de référence utilisé pour l'analyse quantitative. La deuxième partie se concentre sur les techniques de faisceaux d'ions utilisées

dans ce travail. Elle commence par une description des principes de base que sont le SIMS magnétique et le ToF-SIMS suivi par les détails de l'instrument Cameca SC-Ultra utilisé pour ce travail. Cet instrument est conçu pour étudier les matériaux semi-conducteurs avancés, avec une bonne résolution en profondeur. Ensuite, les principes de base de la sonde atomique tomographique (APT), Auger et spectrométrie de rétrodiffusion Rutherford (RBS) sont expliqués. En outre, à la fin de chaque sous-section, les détails expérimentaux pour chaque technique sont donnés.

**Le chapitre III** se concentre sur l'analyse de la composition des PQs  $\text{In}_x\text{Ga}_{1-x}\text{As}$  et les profils de dopage 3D obtenus par SIMS pour les générations futures de transistors. Il commence avec une revue théorique sur l'analyse quantitative par SIMS. Le développement de protocoles SIMS par pulvérisation d'ions oxygène et césium à faible énergie d'impact est décrit. L'analyse quantitative utilisant une série d'échantillons références d' $\text{In}_x\text{Ga}_{1-x}\text{As}$  spécialement conçus dans cette thèse est expliquée. En outre, le rendement d'ions en fonction d'indium fraction  $x$  et de l'énergie primaire du faisceau d'ions est déterminé expérimentalement. L'analyse quantitative utilisant les ions  $\text{MCs}^+$  a également été démontrée pour surmonter les effets de matrice. En outre, le développement de protocoles SIMS et ToF-SIMS des profils de dopage Si en architectures 2D et 3D est décrit.

**Le chapitre IV** aborde l'étude de réseaux de tranchées III-V répétitives crues sélectivement par MOCVD sur des plaquettes de Si structurées. La première section introduit l'approche moyenne pour le profil de composition chimique en profondeur de réseaux répétitifs de tranchées III-V. Cette section décrit également l'optimisation et le développement des conditions SIMS utilisées pour établir le profil des réseaux de tranchées III-V. Les paramètres SIMS tels que (1) l'impact de l'énergie primaire, (2) l'angle d'incidence et (3) l'orientation du faisceau d'ions par rapport aux tranchées sont étudiés en détail afin d'améliorer la résolution en profondeur. L'étude de la formation de la topographie sous irradiation d'oxygène sur les matériaux III-V à l'aide d'observations en microscopie à force atomique et la corrélation avec les profils SIMS sont également incluses. La deuxième partie décrit le profil 3D de composition chimique de PQs InGaAs minces crus sur des plaquettes de Si structurées en utilisant les techniques ToF-SIMS et APT. Cette section représente les études complémentaires effectuées sur différents tableaux III-V tranchés à l'aide de la méthode d'analyse pointue et la moyenne par

la technique Auger. Enfin, l'analyse chimique quantitative des réseaux répétitifs de PQs d'InGaAs étudiés par Auger, SIMS, photoluminescence est décrite.

Les conclusions et perspectives reprennent les principaux résultats obtenus dans cette thèse et énoncent les perspectives pour ce travail en termes de caractérisation des semi-conducteurs III-V pour la technologie CMOS avancée.

### **Les conclusions**

- Des protocoles SIMS avancés pour PQ InGaAs élaboré par MOCVD sur 300 mm tranches de Si ont été développés. Les expériences SIMS ont été réalisées à l'aide de pulvérisation à l'oxygène avec des gammes d'énergie à 250 eV à 5000 eV pour atteindre un rendement élevé d'ions d'éléments du groupe III-. Pour cela, spécialement développé et conçu des plans couches série InGaAs ont été utilisés pour l'analyse SIMS. Les échantillons de référence ont été étudiés pour l'analyse de la composition précise en utilisant des techniques non destructives, par exemple la RBS, sonde nucléaire PIXE( Particle-Induced X-ray emission), et PIGE(Particle-induced Gamma-ray emission). En outre, des échantillons de référence d'ions implantés ont été fabriqués pour étudier le dopage et la contamination dans les matériaux III-V. Une série d'échantillons de référence  $\text{In}_x\text{Ga}_{1-x}\text{As}$  ont été utilisés pour créer la courbe d'étalonnage pour les éléments indium et le gallium. le rendement d'ions et pulvérisation cathodique en fonction de la fraction  $x$  et de l'énergie du faisceau d'ions ont été étudiés. L'analyse quantitative utilisant  $\text{MCs}^+$  a également été démontrée dans le césium faisceau d'ions de pulvérisation d'énergie inférieure à 1 keV. Cependant, les conditions d'analyse à l'aide de pulvérisation d'oxygène sont préférables et principalement utilisé pour étudier les InGaAs PQ plans et non plans .
- Dans GaAs PQ avec des épaisseurs différentes (6, 10 et 19 nm) déposés par MOCVD sur Si a été étudiée. La composition de l'indium dans  $\text{In}_x\text{Ga}_{1-x}\text{As}$  PQ a été estimée par des mesures micro photoluminescence ( $\mu\text{PL}$ ). Les conditions SIMS de pulvérisation cathodique utilisant de l'oxygène à une énergie de 500 eV ont été choisis pour l'étude des couches minces InGaAs. La courbe d'étalonnage en utilisant des échantillons de référence a été utilisée pour quantifier les éléments indium et le gallium dans  $\text{In}_x\text{Ga}_{1-x}\text{As}$  PQ. Les résultats SIMS montrent que le profilage quantitatif précis de couches minces

d'épaisseur inférieure à 5-10 nm est difficile et conduit à des inexactitudes dans la quantification. En effet, l'analyse quantitative précise est limitée par la résolution de profondeur. En outre, la composition de l'indium sous-estimée en InGaAs de 5 à 10 nm PQ par rapport à la  $\mu$ PL a également été observée en utilisant la technique Auger, qui est également limitée par la résolution en profondeur. Ces résultats ont ensuite été utilisés dans l'élaboration de protocoles d'analyse quantitative chimique pour les structures non-planaires.

- Des protocoles SIMS ont été soigneusement optimisés pour étudier les tranchées de structures III-V croissance sélective en utilisant l'état de l'art sur Si. Une bonne qualité de InGaAs/AlAs PQ de 10 nm d'épaisseur a été observée par des signaux  $\mu$ PL à température ambiante. En dépit d'une résolution latérale suffisante (supérieure à 1  $\mu$ m), la possibilité d'effectuer un profilage chimique précis de InGaAs PQ dans des tranchées entourées par des parois SiO<sub>2</sub> a été démontrée. A cet effet, la profondeur des tranchées SIMS pour le profilage III-V de 100-200 nm largeur dans le procédé de profilage de la moyenne a été évaluée. Cette méthode est basée sur les hypothèses suivantes: (i) les structures répétitives, et (ii) le signal provenant de nombreuses tranchées adjacentes proches du signal qui serait obtenu à partir d'une seule tranchée. Le profilage chimique SIMS en profondeur en utilisant cette méthode a montré des interfaces abruptes III-V et a confirmé les observations PL. Les profils chimiques pour des tranchées étroites et répétitives III-V démontrent un bon accord avec les observations STEM. La méthode de la moyenne de profilage a été confirmée par des mesures effectuées par Auger sur des tranchées individuelles III-V à l'aide de deux méthodes d'analyse pointues et moyennes.
  
- L'analyse quantitative pour une série de InGaAs PQ non plan minces (9 nm d'épaisseur) a été effectuée en utilisant les deux techniques SIMS et Auger. Il a été observé que la quantification par SIMS et Auger dépend fortement de la légère variation de l'épaisseur des couches ainsi que leur forme géométrique. Il y a une différence dans la composition d'indium trouvée avec le SIMS et Auger rapport à celle extraite à partir des mesures  $\mu$ PL. Cette différence vient des bords qui contribuent à des signaux en SIMS et Auger réduisant ainsi la composition d'indium apparente du InGaAs PQ. Pour PL, il ne contribue pas parce que le confinement quantique est parallèle à la direction de croissance et, par conséquent, la composition de l'indium est extraite ultérieurement.

- L'analyse quantitative et de distribution des atomes dans le 3D volume des hétérostructures III-V ont été étudiés par TOF-SIMS et APT. Les mesures sont trouvés cohérente et montrent une bonne uniformité dans la composition. Interfaces brusque InGaAs/AlAs ont été démontrées en utilisant APT avec une résolution de moins de 1 nm/decade grande profondeur tandis que les deux SIMS et TOF-SIMS sont plus adaptés pour le profilage chimique des structures uniformes répétitives. Néanmoins, l'APT donne des informations à partir d'un petit volume d'une tranchée qui peut ne pas être représentatif de toute la gamme des tranchées. En effet, quand la largeur de tranchée devient étroite (moins de 40 nm) la présence de parois latérales SiO<sub>2</sub> fait des distorsions dans le volume APT.
- Des protocoles SIMS et TOF-SIMS pour les mesures de concentration en dopants Si dans des architectures 2D et 3D ont été développés en utilisant une méthode de la moyenne. Les échantillons contenant GaAs (dopé n)/GaAs/Si stack croissance sélective sur des substrats de silicium à motifs ont été étudiés. Cependant, la présence de parois de barrière de SiO<sub>2</sub> rend les mesures de Si de dopage difficile. Une solution pour surmonter ce problème était d'éliminer les obstacles SiO<sub>2</sub> utilisant une gravure HF. Il a été constaté que le Si dopage dans les structures non-planes est possible en utilisant de SiAs-, SiGa-ions. En outre, il a été démontré que l'orientation du faisceau d'ions par rapport à la tranchée a un impact sur les limitations de dopants, car en orientation perpendiculaire le substrat est moins visible que dans une orientation parallèle, ce qui contribue moins au signal global du Si.

Les protocoles SIMS pour les matériaux de canal InGaAs par profilage dans les structures répétitives étroites avec haute résolution en profondeur ont été développés. La capacité de faire des profils en profondeur et effectuer les mesures de dopage des centaines de tranchées III-V seront utiles pour l'identification chimique des dispositifs plus complexes. Tous les résultats présentés peuvent trouver des applications dans les futurs dispositifs monolithiques intégrés sur silicium III-V FinFET ou SOI FD-III-V

